Probing Mn-Mn and Mn-Si Bonding in Silicon Cages



Vaibhav Khanna

St Hugh's College

University of Oxford

A thesis submitted for the degree of

Master of Science by Research

April 2022

Acknowledgements

I would like to thank Prof. John McGrady for his guidance and support over the past two years.

I would also like to thank Pieterjan Claes, Ewald Janssens and Peter Lievens from KU Leuven, Belgium and André Fielicke from Fritz-Haber-Institut der Max-Planck-Gesellschaft, Germany for conducting the Infrared Multiple Photon Dissociation (IR-MPD) spectroscopic measurements.

Finally, I would like to thank my parents and my sister Brinda for supporting me financially and emotionally during my time at Oxford.

Abstract

This thesis explores the geometry and electronic structure of some manganese doped silicon clusters. Experimental characterisation of these clusters is severely limited. Theoretical investigations with density functional theory (DFT) yield conflicting results due to differences in the choice of functional. Hence, a combination of both theory and experiment has been employed: our experimental collaborators have measured the IR-MPD spectra of these clusters while we have used DFT calculations to explore the potential energy surfaces. For a given cluster, the vibrational spectra for low-lying isomers have been computed and compared with the measured spectrum to identify the experimentally observed isomers. The information content of the spectra has been expanded by assigning vibrational modes to various peaks and by identifying vibrational signatures. Given that there is no consensus about the choice of functional, the results have been computed with a range of functionals. The influence of functional choice on the conclusions has been studied which reveals how certain functionals stabilise structures with low vertex connectivity while others tend to favour deltahedral frameworks. Multiconfigurational self-consistent field theory (MC-SCF) has been used to get an alternative perspective on bonding in these clusters. By making use of generalised and restricted active spaces (GAS and RAS), important contributions to static correlation in these clusters have been probed. An attempt has been made to account for dynamic correlation by applying perturbation theory corrections to energies obtained by the RASSCF method. However, sufficient static correlation has not been captured in the RASSCF wavefunction to allow for a reliable perturbative treatment of the remaining, missing, correlation.

Declaration

All Infrared Multiple Photon Dissociation (IR-MPD) spectroscopic measurements were carried out by Pieterjan Claes, Ewald Janssens and Peter Lievens from KU Leuven, Belgium and André Fielicke from Fritz-Haber-Institut der Max-Planck-Gesellschaft, Germany. The experimental data were also submitted in the PhD thesis of Pieterjan Claes (KU Leuven). The experimentally measured spectra for the clusters Mn_2Si_{10}, Mn_2Si_{11}, Mn_2Si_{12}, Mn_2Si_{13}, $[Mn_2Si_{13}]^+$, $[Mn_2Si_{14}]^+$ and $[Mn_2Si_{15}]^+$ have been included in this thesis and the experimental technique has also been described for context, but these experiments were not performed by the author - they are provided for comparison to theory, which is the author's contribution. Specifically, the author has assigned the IR-MPD spectra of these clusters to different isomers using density functional theory (DFT) calculations. The author has also identified and assigned vibrational modes to peaks in the spectra.

Vaibhav Khanna

Contents

1 Introduction **1**

1.1 Early studies 1

1.2 Computational studies 4

1.3 Experimental studies 5

1.3.1 Photoelectron spectroscopy 5

1.3.2 X-ray absorption and XMCD spectroscopy 8

1.3.3 Infrared Multiple Photon Dissociation (IR-MPD) spectroscopy . . 9

1.4 Doubly doped silicon clusters 11

1.5 Beyond DFT 13

1.6 Synopsis 15

2 Theoretical Background **17**

2.1 Electronic Structure Theory 17

2.1.1 Introduction 17

2.1.2 Hartree-Fock theory 19

2.1.3 Density functional theory 22

2.1.3.1 Exchange-correlation functionals 24

2.1.4 Post-Hartree-Fock methods 26

2.1.4.1 CASSCF 28

2.1.4.2 RASSCF 29

2.1.4.3 GASSCF 30
2.1.5 Basis functions 31
2.1.5.1 Slater-type orbitals 31
2.1.5.2 Gaussian-type orbitals 32
2.1.5.3 Size, quality, and notation 33
2.1.5.4 Core electrons 34
2.2 Molecular Symmetry 34
2.3 Vibrational Frequencies 38

3 Evolution of Vibrational Spectra in the Manganese-Silicon Clusters Mn_2Si_n, n = 10, 12, 13, and cationic $[Mn_2Si_{13}]^+$ 40

3.1 Introduction 40
3.2 Methodology 42
3.2.1 Experimental Techniques 42
3.2.2 Computational Techniques 43
3.3 Results and Discussion 44
3.3.1 IR-MPD spectroscopy of Mn_2Si_{10}, Mn_2Si_{12}, Mn_2Si_{13} and $[Mn_2Si_{13}]^+$ 44
3.3.2 Density Functional Theory 46
3.3.2.1 Ground-state structure and vibrational spectrum of Mn_2Si_{12} 46
3.3.2.2 Ground-state structure and vibrational spectrum of $[Mn_2Si_{13}]^+$ 52
3.3.2.3 Symmetry analysis and comparison of Mn_2Si_{12} and $[Mn_2Si_{13}]^+$ 53
3.3.2.4 Vibrational spectrum of Mn_2Si_{13} 58
3.3.2.5 Vibrational spectrum of Mn_2Si_{10} 59
3.4 Summary and Conclusions 62

4 Divergence from the unequivocal assignment of IR-MPD spectra 64

4.1 Introduction 64
4.2 Methodology 65

4.2.1 Experimental Techniques 65
4.2.2 Computational Techniques 65
4.3 Results and Discussion 66
4.3.1 Density Functional Theory 66
4.3.1.1 Ground-state structure and vibrational spectrum of $[Mn_2Si_{14}]^+$ 66
4.3.1.2 Ground-state structure and vibrational spectrum of $[Mn_2Si_{15}]^+$ 67
4.3.1.3 Ground-state structure and vibrational spectrum of Mn_2Si_{11} 70
4.3.2 Effect of the Xe tag 73
4.3.3 Choice of initial structures: Algorithms vs Chemical intuition . . . 74
4.3.3.1 $[Mn_2Si_{15}]^+$ 77
4.4 Summary and Conclusions 80

5 Beyond DFT: the use of wavefunction-based methods 83
5.1 Introduction 83
5.2 Methodology 84
5.2.1 Computational Techniques 84
5.3 Results and Discussion 84
5.3.1 GASSCF Calculations of Mn_2Si_{12} 84
5.3.2 GASSCF Calculations of $[Mn_2Si_{13}]^+$ 86
5.3.3 GASSCF Calculations of Mn_2Si_{10} 87
5.3.4 RASSCF/RASPT2 Calculations of $[Mn_2Si_{13}]^+$ 88
5.3.5 CASPT2 Calculations of $[Mn_2Si_{13}]^+$ 90
5.4 Conclusions 96

6 Summary 97

Bibliography 100

Chapter 1

Introduction

1.1 Early studies

Located between carbon and germanium in group 14 of the periodic table, silicon is, to say the least, an interesting element. It marks the point in group 14 where the inert pair effect begins to have an influence on the structural chemistry and, unlike carbon, primarily forms single rather than double and triple bonds. The stability of carbon-carbon multiple bonds arises from the effective overlap between 2p orbitals of adjacent carbon atoms. On the other hand, the overlap between 3p orbitals of adjacent silicon atoms is poor, as a result of which, silicon is usually incapable of forming strong π bonds. However, unsaturated compounds of silicon have been made recently and continue to draw the attention of scientists across the world. [1] Aside from its interesting chemical properties, silicon has found numerous applications from the processors of our mobile phones to the cement that holds houses together, from the breathtaking stained glass windows of Sainte-Chapelle to the ceramic cups for our morning tea. In short, silicon forms an indispensable part of modern life.

The electronic structure and properties of silicon clusters have been explored by many researchers across the world. As mentioned above, silicon is incapable of forming strong

π bonds. Consequently, cage clusters of silicon are highly reactive due to the presence of dangling bonds. Doping silicon clusters with transition metals imparts stability due to hybridisation between d orbitals of metals and 3s/3p orbitals of silicon. [2, 3] These doped clusters can be viewed as minimal models for transition metal impurities in bulk silicon, which is an issue of importance in the semiconductor industry. Such clusters offer a way of understanding the chemistry behind reactions that occur between a metal and a semiconductor. The underlying mechanisms behind cluster formation can offer insights into the reactions that occur at the interface between metals and silicon [4]. Ongoing research in the field of doped silicon clusters forms the first step towards realizing cluster assembly materials. Studying the effect of doping different transition metals in silicon clusters can indeed be considered equivalent to varying the properties of building blocks for potential cluster assembly materials. Figure 1.1 shows different 2D planar crystal structures that could be made from endohedrally doped hexagonal prismatic Si_{12} clusters [5].

Research into transition metal doped silicon clusters can be dated back to Beck's work in 1987. [4] He reported that Si_{16} clusters doped with Cr, Mo and W were the major species observed amongst similarly doped silicon clusters of different sizes. Figure 1.2 shows the mass spectra of some Cr doped silicon clusters produced by two different methods, the first of which involved laser vaporisation of a silicon target with $Cr(CO)_6$ in the carrier gas and the second involved vaporisation of a silicon substrate with thick stripes of Cr deposited on it. With both methods, the largest peaks in the spectra corresponded to $CrSi_{16}$ [6] which led to the concept of "magic clusters"; doped clusters with certain sizes were found to be more stable and abundant as compared to neighbouring clusters of different sizes.

Several magic clusters have been identified. However, our discussion will be limited to $CrSi_{12}$ which has a D_{6h} hexagonal prismatic structure with the Cr atom occupying an endohedral position. [7] Despite the high magnetic moment of the isolated Cr atom

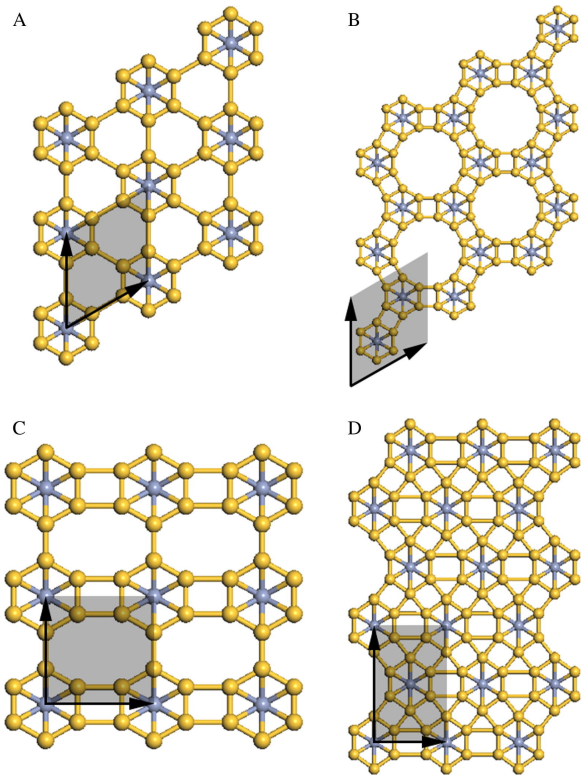


Figure 1.1: Different 2D planar crystal structures made from transition metal doped hexagonal prismatic Si_{12} clusters: hexagonal honeycomb lattice (A), hexagonal porous lattice (B), square lattice (C) and central rectangular lattice (D). Reprinted from [5], Copyright (2018), with permission from Elsevier.

(6 μ_B), the magnetic moment of Cr in $CrSi_{12}$ is completely quenched because of the hybridization between Cr 3d and 3s 3p states of Si [7]. There are several electron counting rules that have been used to rationalise the stability of such magic clusters, one of which is the 18-electron rule. The stability of $CrSi_{12}$ could be rationalised using this rule if we assume that each Si atom contributes one electron and the Cr atom contributes six [7, 8]. However, upon a closer look, it was observed that $CrSi_{12}$ does not exhibit all markers of a magic cluster. It does not have the largest HOMO-LUMO gap in the series of Cr-doped silicon clusters and is not characterized by a filled 3d electronic shell ($3d_{z^2}$ orbital is unoccupied) and so a 16 effective valence electron count has been proposed instead. [9].

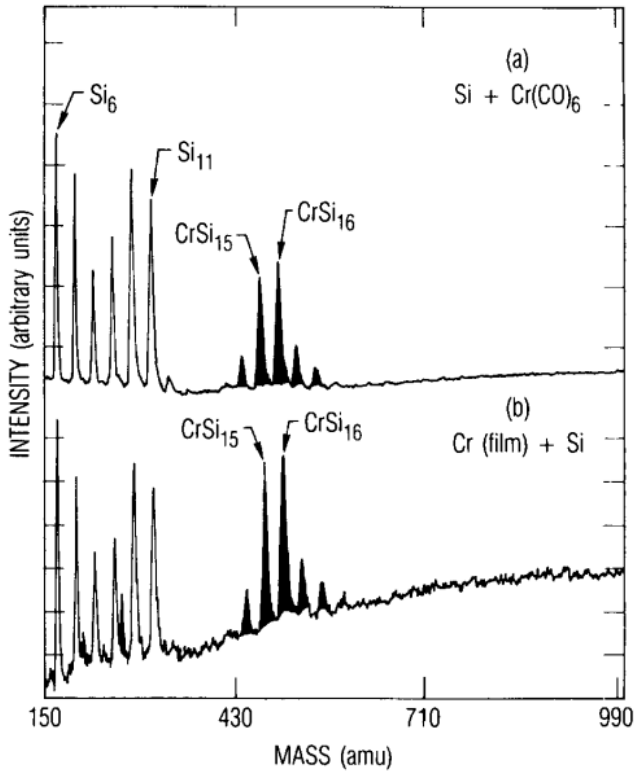


Figure 1.2: Mass spectra of Cr doped silicon clusters produced by two different methods. Reprinted from [6], with the permission of AIP Publishing.

1.2 Computational studies

Several theoretical attempts have been made to investigate the geometries and electronic structure of doped silicon clusters. Most of these studies have employed Density Functional Theory (DFT) which offers an important advantage of being computationally cost effective. However, DFT also has a major limitation: in any DFT calculation, the choice of the exchange-correlation functional is critical, and the results of these calculations often depend on the choice of functional used. For doped silicon clusters, there is no clear consensus about the best functional, and different researchers have used different criteria to choose functionals for their studies which has often led to conflicting results. The cluster $CrSi_{14}$ illustrates this problem perfectly. Abreu and co-workers [9] have used the PBE functional and reported an arachno structure (a structure with high vertex connec-

tivity) for this cluster (Figure 1.3 (a)). [9]. On the other hand, He and co-workers have employed the hybrid B3LYP functional and reported a fullerene-like structure (with low vertex connectivity) for the same cluster $CrSi_{14}$ (Figure 1.3 (b)). [10] The global minimum is therefore dependent on the choice of functional, and without definitive experimental evidence, it is not obvious which choice is better. Moreover, it is possible that there are several low-lying isomers for a cluster which are close in energy, which makes the assignment of one isomer as the global minimum even more challenging.

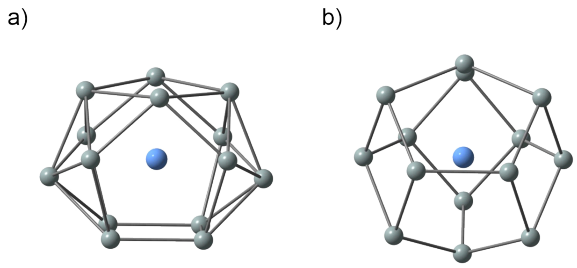


Figure 1.3: Reported structures for $CrSi_{14}$ a) arachno structure [9] and b) fullerene-like structure [10].

X-ray crystallographic data for these gas-phase clusters remains elusive, and techniques including photoelectron spectroscopy, X-ray absorption spectroscopy and infrared spectroscopy have been employed instead to provide indirect evidence about structure and bonding. Comparing the calculated spectrum of an isomer with the experimental spectrum provides a way to deduce whether or not the theoretically predicted isomer is the one that is experimentally observed. In the following sections, we will describe the use of these techniques in deducing the structures of doped silicon clusters.

1.3 Experimental studies

1.3.1 Photoelectron spectroscopy

There have been a number of studies that combine photoelectron spectroscopy and DFT calculations to explore the structures of doped silicon clusters. We will discuss the work of

Yang and co-workers, who have employed mass-selected anion photoelectron spectroscopy and density functional theory to deduce the structures of a series of cobalt doped silicon clusters, as an illustrative example. [11] The experiment was carried out by generating Co-Si clusters in a laser-vaporisation source. Each cobalt doped silicon cluster was then mass-analyzed using a time-of-flight mass spectrometer. In the photodetachment region, these clusters were crossed with a beam from a Nd:YAG laser. The detached electrons were then analyzed through a magnetic-bottle photoelectron spectrometer to probe the energies of the corresponding orbitals.

The initial structures for geometry optimisation were obtained in two ways. The first method made use of the Particle Swarm Optimization (PSO) algorithm that is based on self-improving structures using swarm intelligence, implemented through the software package CALYPSO, to identify low-lying candidate structures, while the second method involved using chemical intuition. The expression 'chemical intuition' merits further clarification because it is a broad one that captures a range of approaches, and is used widely in this thesis. These include recourse to simple electron-counting models such as Lewis Structures and Wade's rules to predict plausible starting structures. It also encompasses reference to literature precedent for clusters of similar composition, the permutation of M/Si atoms between different sites and the addition/removal of atoms from clusters with fewer/more atoms than the target. In short, 'chemical intuition' captures any approach to the generation of structures that does not involve random placement of atoms. DFT calculations were performed using PBE as the functional with the Gaussian package. Single point energies of low-lying isomers were then calculated with the coupled-cluster single and double, and perturbative triple excitation (CCSD(T)) method, with the aim of getting more accurate values of relative energies.

The generalized Koopmans' theorem was used to simulate the photoelectron spectra of the low-lying isomers. The experimentally observed isomers were identified by comparing the computed spectra of low-lying isomers with the measured photoelectron spectrum.

The comparison between computed spectra of candidate structures and measured spectrum of $[CoSi_{10}]^-$ is shown in Figure 1.4 [11]. For $[CoSi_{10}]^-$, isomer 10A was identified as the one observed in the experiment based on the match between its computed and measured spectrum. The cluster proved to have a closed shell configuration within the Jellium model, consistent with its relative stability.

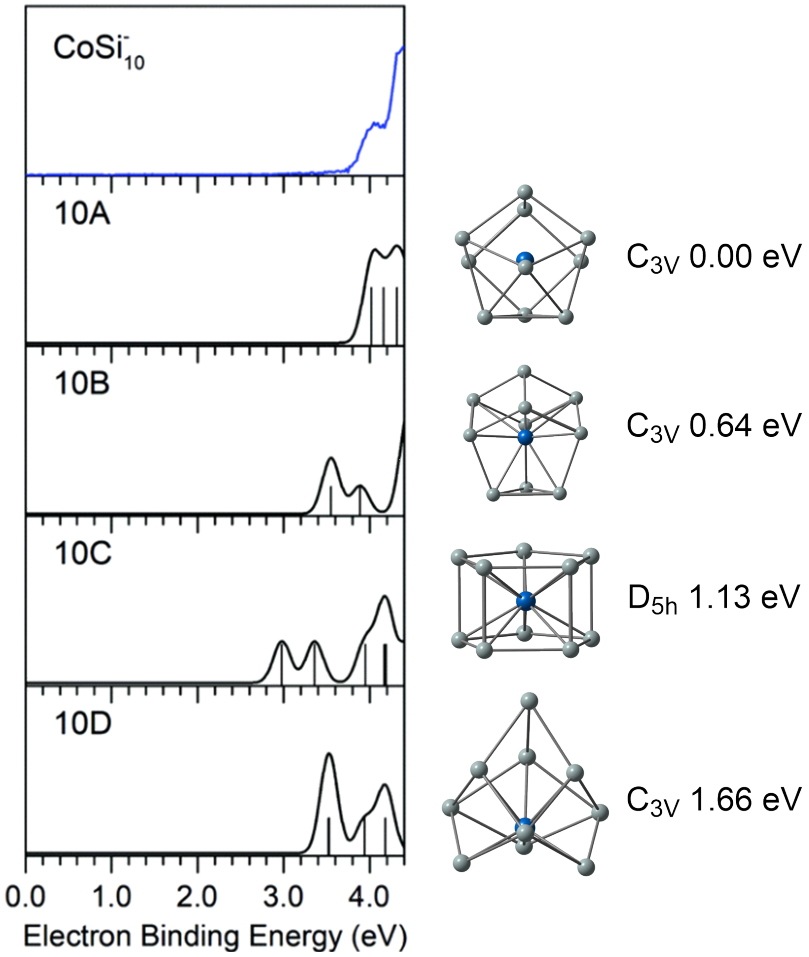


Figure 1.4: Comparison between the measured photoelectron spectrum and the simulated spectra of the low-lying isomers of $[CoSi_{10}]^-$. Republished with permission of Royal Society of Chemistry, from [11] Copyright 2019; permission conveyed through Copyright Clearance Center, Inc.

1.3.2 X-ray absorption and XMCD spectroscopy

X-ray absorption studies have also been used to explore the electronic structure of doped silicon clusters. Even though there are only a few studies of this kind, they provide valuable information about the geometry and magnetic properties of clusters. For example, Zamudio-Bayer and co-workers explored the electronic structure of some manganese doped silicon clusters using a combination of X-ray absorption spectroscopy and DFT. [12] The structural properties of these clusters were investigated by monitoring their depletion on introducing oxygen gas. The difference in the reactivity of manganese and silicon towards oxygen helped in determining the exohedral-to-endohedral transition of the dopant.

Two different optimization algorithms were used to find low-lying candidate structures: the simulated annealing approach, which heated initial structures to high temperatures of 4000 K and then cooled them slowly to 300 K to reach a local minimum, and the modified big bang approach, which randomly generated structures with compressed bond lengths and propagated them at 300 K for a short time span of 1.5 ps. The geometry optimisations were carried out with the TURBOMOLE package and used the PBE0 functional.

For the computed structures, it was observed that the Mn dopant occupied an exohedral position in $[MnSi_n]^+$, n = 7-10 and moved to an endohedral position for n = 11-14. This was supported by changes in depletion of singly doped $[MnSi_n]^+$ clusters in the presence of oxygen. The depletion, which was in the range of 89 to 94 % for n = 7-10, dropped to 0 to 15 % for n = 11-14. The structural transition from $[MnSi_{10}]^+$ to $[MnSi_{11}]^+$ also coincided with the change in the electronic properties of $[MnSi_n]^+$ as seen in the XMCD spectra (Figure 1.5), which probe local transitions at the Mn dopant. By observing the asymmetry in the XMCD spectra, it was concluded that upto n = 10, the Mn atom retained its magnetic moment and occupied an external position but from n = 11 the magnetic moment was lost which was an indication of the encapsulation of the transition metal dopant. The quenching of magnetic moment for endohedral clusters was attributed to the delocalization of 3d electrons of the transition metal due to strong

interactions with the silicon cage [12].

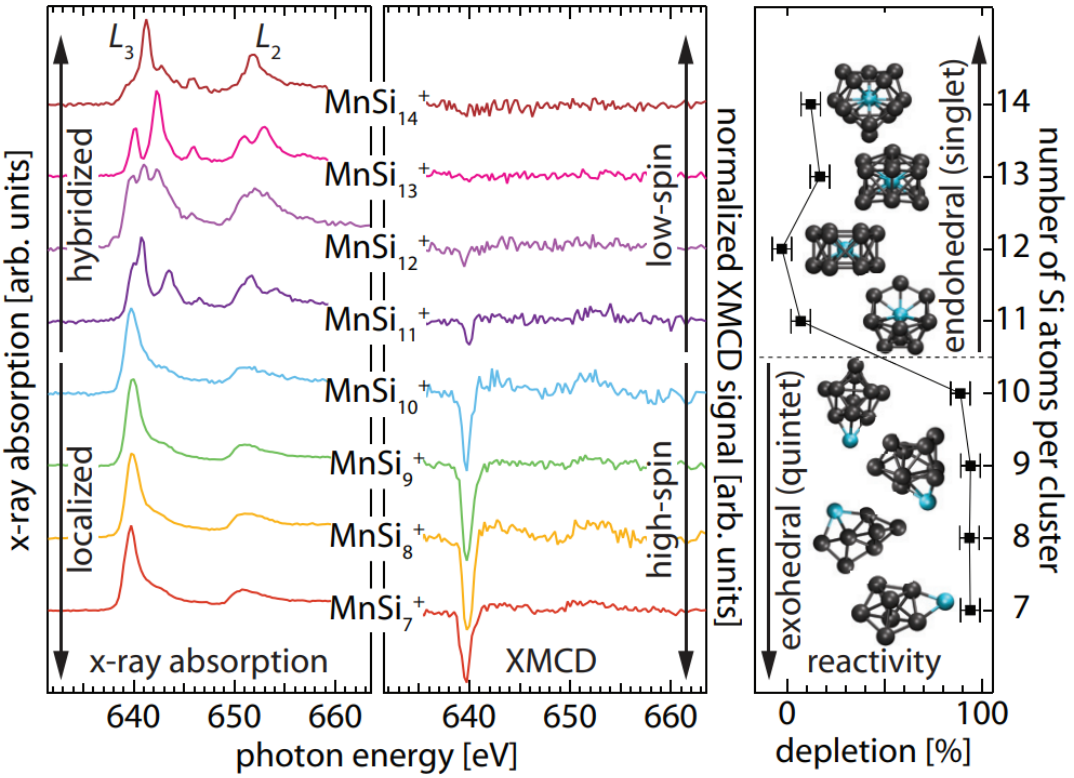


Figure 1.5: The X-ray absorption spectra of manganese (2p), XMCD spectra of $[MnSi_n]^+$ n = 7-14 clusters and the depletion of $[MnSi_n]^+$ clusters in the presence of oxygen. Reprinted (figure) with permission from [[12]] Copyright (2013) by the American Physical Society.

1.3.3 Infrared Multiple Photon Dissociation (IR-MPD) spectroscopy

Infrared Multiple Photon Dissociation (IR-MPD) spectroscopy is another experimental technique that has been used in a number of studies to deduce the structures of doped silicon clusters. This technique forms the experimental basis of this thesis, and will be described in greater detail in Chapter 3. The infrared spectrum of a cluster is measured using this technique by monitoring the loss of a rare gas atom tag from the corresponding cluster-rare gas complex. We will focus here on a study that investigated the structures of certain Cu and V doped silicon clusters [13] using a combination of IR-MPD spectroscopy and DFT calculations.

The initial structures for DFT calculations were obtained by carrying out literature surveys for structures of similar clusters and by adding dopant atoms to previously reported structures of silicon clusters. The geometry optimisation and vibrational frequency calculations were performed with the Gaussian package using BP86 as the functional. The experimentally observed isomers were identified by comparing the computed spectra of low-lying isomers with the measured IR-MPD spectrum. One example of such a comparison is depicted in Figure 1.6 which shows the low-lying isomers of $[Si_7Cu]^+$, their computed infrared spectra and the IR-MPD spectrum for $[Si_7Cu]^+$·Ar complex. [13] For $[Si_7Cu]^+$, isomer iso1 was identified as the one observed in the experiment based on the match between its computed and measured spectrum.

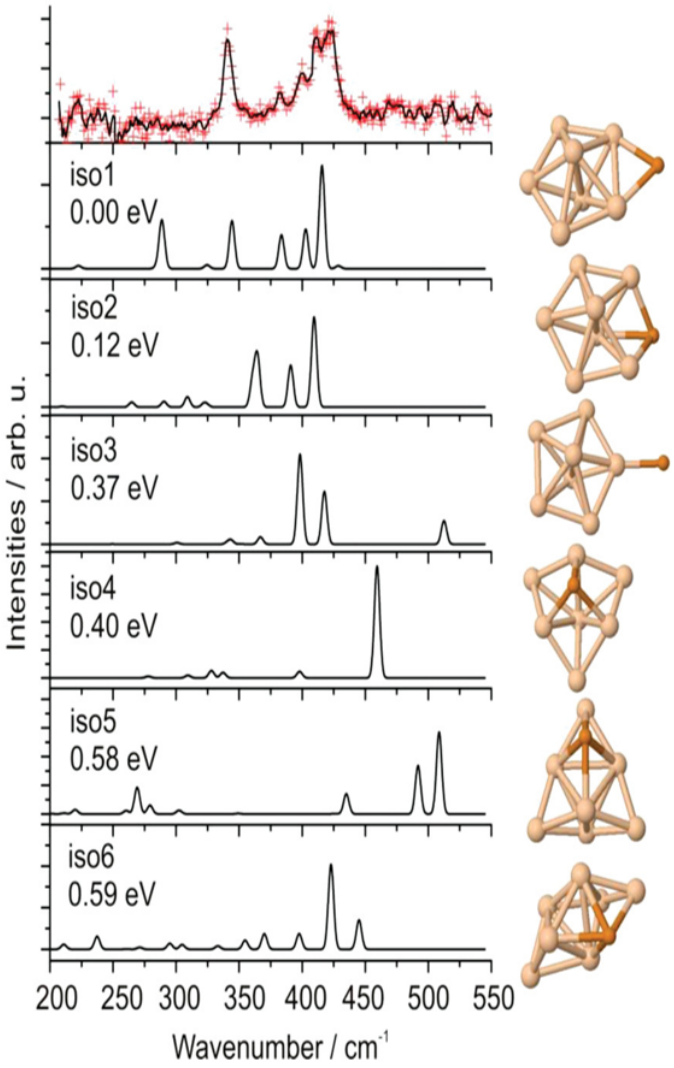


Figure 1.6: IR-MPD spectrum of $[Si_7Cu]^+ \cdot Ar$ complex (intensity in arbitrary units), optimized structures and computed IR spectra of the low-lying isomers of $[Si_7Cu]^+$. [13] (https://pubs.acs.org/doi/10.1021/ja105099u; Further permissions related to the material excerpted should be directed to the ACS.)

1.4 Doubly doped silicon clusters

In all the studies discussed so far, silicon clusters have been doped with a single transition metal atom, and in most endohedral clusters, the magnetic moment of this transition metal atom is quenched. Stable silicon building blocks that retain the magnetic moment of the transition metal are, however, required for applications in spintronics, and so the quenching of magnetic moment is a serious limitation to the use of these clusters as building blocks.

One possible solution is to use silicon clusters doped with multiple transition metal atoms. Intuitively, the first step is to consider clusters containing two metal atoms. Studies that investigate clusters in which transition metal dimers are surrounded by non-magnetic materials have only been conducted recently. As an illustrative example, Bista and co-workers investigated the electronic structure of silicon clusters doped with two iron atoms [14]. DFT calculations with PBE functional were carried out to find the global minima of a series of iron doped silicon clusters. A large number of initial structures were considered to scan the potential energy surface. The coupling between Fe atoms in these clusters was examined and the magnetic anisotropy energies were calculated using the Naval Research Laboratory Molecular Orbital Library, NRLMOL, set of codes.

Figure 1.7 (a) shows the ground state structures of Fe_2Si_n clusters (n=1-12). As evident from the figure, the Fe-Fe dimer remained intact in most cases. The magnetic moment was also found to be non-zero for a number of clusters (Figure 1.7 (b)). The authors also tried to correlate the Fe-Fe distances with the nature of coupling between them. It was observed that large Fe-Fe separations correlated with antiferromagnetic coupling between the Fe atoms which was in turn related to the local moments being derived from nonbonding 3d orbitals. On the other hand, short Fe-Fe distances correlated with ferromagnetic coupling with the magnetic moment born from antibonding orbitals between the atoms.

DFT with a single functional was employed in this study to assign ground state structures and calculate relative energies of different isomers. In light of the debate about the structure of $CrSi_{14}$, conclusions from DFT calculations strongly depend on the choice of functional used, so it could have been better if the results were also validated with some experimental measurements. However, such experimental measurements are not easily available for doubly doped silicon clusters. Studies combining photoelectron spectroscopy or IR-MPD spectroscopy with DFT calculations can be extremely valuable for such clusters. The central theme of the upcoming chapters will be based on this idea where we

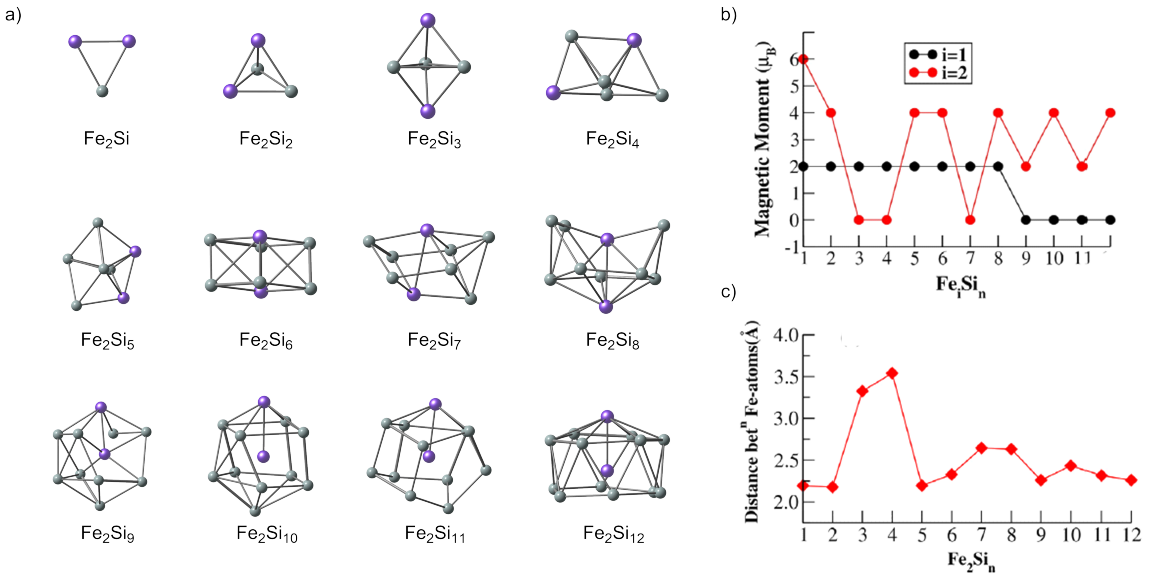


Figure 1.7: (a) Ground state structures of Fe_2Si_n clusters (n=1-12), (b) variation of total magnetic moment of Fe_2Si_n and $FeSi_n$ with cluster size and (c) variation of separation between Fe atoms in Fe_2Si_n clusters with cluster size. Reprinted from [14], Copyright (2018), with permission from Elsevier.

will use both IR-MPD spectra (measured by Ewald Janssens and co-workers) and DFT calculations to explore the geometries and electronic structure of some silicon clusters containing two Mn atoms.

1.5 Beyond DFT

Up to this point, we have only discussed studies that employ density functional theory to investigate the electronic structure of doped silicon clusters. As observed in case of $CrSi_{14}$, the results of DFT calculations depend on the choice of exchange-correlation functional used, with some functionals favouring localised σ/π bonding in structures with low vertex connectivity while others stabilising multi-centre delocalised bonding in deltahedral frameworks. The criteria of selecting a functional also differs for different researchers: some prefer to choose functionals that reproduce experimental measurements while others prefer to select functionals that give results which are consistent with higher levels of theory like CCSD(T). Consequently, a situation arises where multiple functionals

are used to address the same research problem, ultimately leading to conflicting results.

There are some systems that cannot be described by a single Slater determinant and the use of DFT for such systems is problematic. For singly doped silicon clusters, some studies have employed the multiconfigurational self-consistent field (MC-SCF) method which, being a wavefunction-based approach, offers a more robust way of dealing with static correlation. We will discuss one such study here. Arcisauskaite and co-workers investigated the geometry and electronic structure of $[MnSi_{12}]^+$ using DFT, CASPT2 and IR-MPD spectroscopy [15].

Five different states of $[MnSi_{12}]^+$ were considered which were all based on the hexagonal prismatic structure of the silicon cage with the Mn atom occupying an endohedral position. The results of DFT calculations (BLYP, B3LYP/TZP level) for open-shell states were found to be spin-contaminated, which usually is an indication of multiconfigurational character. Hence, the complete active space method with second order perturbation theory corrections (CASPT2) was employed using the MOLCAS package.

A (10,15) active space containing orbitals with Mn 3d character, Mn-Si frontier bonding and anti-bonding orbitals (similar to the Kohn-Sham orbitals) and five 4d orbitals was considered for each state (Figure 1.8). The occupation numbers of active orbitals for all states showed significant "in-out" correlation between electrons in Mn-Si bonds. For open shell singlet and triplet states, some active orbitals were also singly occupied. The 4d orbitals had occupations very close to zero, so they could be removed from the active space without changing the CASPT2 energy significantly. It was observed that the triplet states were lower in energy by 0.07–0.09 eV than the singlets irrespective of the geometry. Such an energetic difference was below the threshold where the authors could confidently make a definitive assignment of the ground state.

There are only few studies on doubly doped silicon clusters that make use of the MC-SCF method. On addition of the second metal atom, there is a possibility of "left-right" correlation between electrons on the two metal centers in addition to the "in-out"

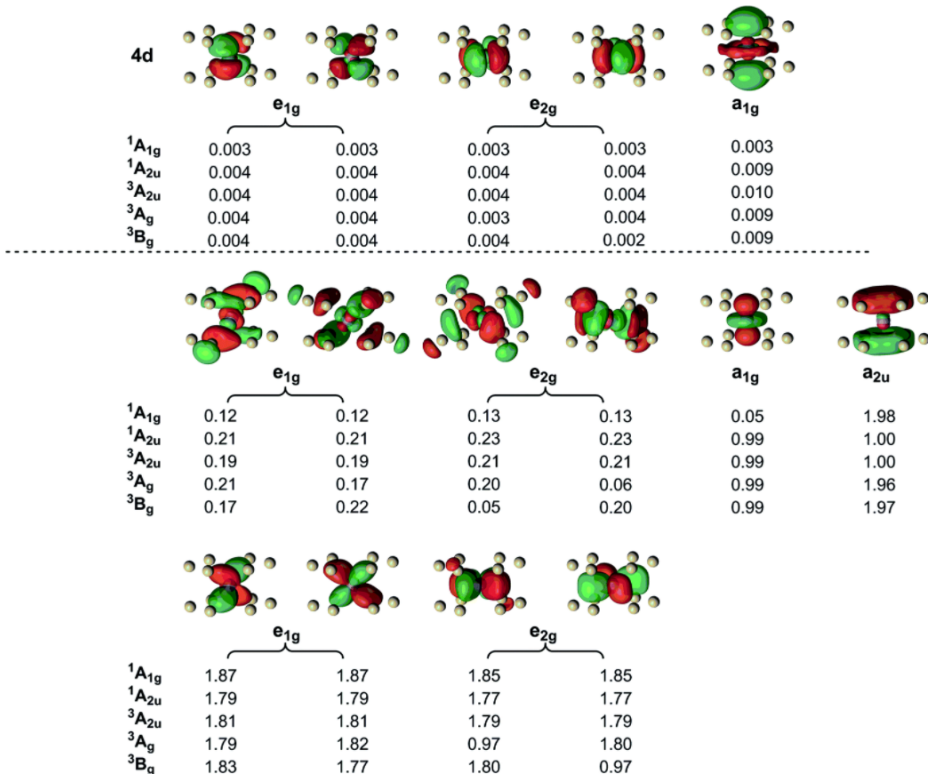


Figure 1.8: Natural orbitals and occupation numbers for (10,15) active space of various states of $[MnSi_{12}]^+$. Reproduced from [15].

correlation which increases the dimension of the problem beyond the limit that can be tackled by a conventional active space. Hence, the dimension of the CI expansion needs to be restricted. Therefore, methods like Generalized Active Space Self-Consistent Field (GASSCF) and Restricted Active Space Self-Consistent Field (RASSCF), which limit the number of configurations, need to be used. However, achieving a balanced treatment of both static and dynamic correlation to calculate energies of isomers still remains a challenge.

1.6 Synopsis

In this thesis, the geometry and electronic structure of some silicon clusters containing two Mn atoms will be explored using a combination of theory and experiment. DFT calculations will be used to scan the potential energy surface and identify low-lying iso-

mers for each cluster. By comparing the IR-MPD spectra (measured by Ewald Janssens and co-workers) and the computed vibrational spectra for candidate structures, the experimentally observed isomers will be identified. The information content of the spectra will be expanded by identifying vibrational signatures and assigning vibrational modes to peaks. The influence of the functional choice on the relative energies of different isomers will be studied. Going beyond the functional roulette, multiconfigurational self-consistent field (MC-SCF) theory will be employed to get an alternative perspective on bonding. Important contributions to static correlation in these clusters will be probed and attempts will be made to account for the residual dynamic correlation.

Chapter 2

Theoretical Background

The purpose of this chapter is to provide sufficient theoretical background that is required to understand the chapters that follow. It begins with the initial developments in quantum chemistry and then builds on to methods used in modern day computational research. Concepts of molecular symmetry are also discussed because of their use in chemical analysis.

2.1 Electronic Structure Theory

2.1.1 Introduction

The paramount aim of computational chemistry is to find the total energy of a given system which requires solving the time-independent Schrödinger equation (TISE) :

$$\hat{H}\Psi = E\Psi \tag{2.1}$$

where $\hat{H}$ is the Hamiltonian operator. For a given system, it takes into account the interactions that contribute to the total energy. It can be written as a sum of the kinetic

energy ($\hat{T}$) and potential energy operators ($\hat{V}$) :

$$\hat{H} = \hat{T} + \hat{V} \tag{2.2}$$

For a system comprising of electrons and nuclei, the kinetic energy operator can be simply expressed as a sum of kinetic energy operators for electrons and nuclei.

$$\hat{T} = \hat{T}_e + \hat{T}_n \tag{2.3}$$

The potential energy operator can be written as:

$$\hat{V} = \hat{V}_{ne} + \hat{V}_{ee} + \hat{V}_{nn} \tag{2.4}$$

In equation 2.4, the term corresponding to interelectronic repulsions $\hat{V}_{ee}$ makes it impossible to solve the time-independent Schrödinger equation for any system with more than one electron because the magnitude of repulsion between a pair of electrons depends on the separation between them. Being negatively charged, electrons try to avoid each other to minimise the Coulomb repulsion. Hence, their positions are not independent but are correlated. Moreover, as a consequence of their quantum nature, the position of electrons cannot be described precisely. Hence, one employs a probability distribution to specify their positions. All these factors make the interaction potential between pairs of electrons impossible to evaluate analytically. Hence, computational chemistry methods aim to find approximate solutions to the Schrödinger equation. The Born-Oppenheimer approximation helps in simplifying the solution of the time-independent Schrödinger equation. Since the mass of an atomic nuclei is much more than that of an electron, the Born-Oppenheimer approximation states that the nuclei can be assumed to be static on the time-scale of

movement of electrons. As a result, the electronic Hamiltonian can be written as:

$$\hat{H}_e = \hat{T}_e + \hat{V}_{ne} + \hat{V}_{ee} \tag{2.5}$$

This is because the kinetic energy contribution of the nuclei ($\hat{T}_n$) vanishes and the internuclear repulsion ($\hat{V}_{nn}$) is constant. Hence the electronic Schrödinger equation is given as:

$$\hat{H}_e \Psi_e = E_e \Psi_e \tag{2.6}$$

The variation theorem offers a way of finding approximate energies and wavefunctions of a system. It involves guessing a trial wavefunction ψ_{trial} for a system. The theorem states that the corresponding energy ϵ will always be higher than the true ground state energy E_0 of the system.

$$\epsilon = \frac{\langle \psi_{trial} | \hat{H} | \psi_{trial} \rangle}{\langle \psi_{trial} | \psi_{trial} \rangle} \tag{2.7}$$

$$\epsilon \geq E_0 \text{ for any } \psi_{trial} \tag{2.8}$$

The equality in equation 2.8 only holds true when the trial wavefunction ψ_{trial} is the same as the true ground state wavefunction ψ_0. The variation theorem can allow us to change the trial wavefunction ψ_{trial} in order to lower ϵ towards E_0. Usually, one or more parameters are used to express the trial wavefunction ψ_{trial}. The variation principle looks for values of these parameters that minimize ϵ. Consequently, the corresponding wavefunction is the optimum function of that form.

2.1.2 Hartree-Fock theory

The difficulty in describing the interelectronic interactions while composing the Schrödinger equation poses an issue. Hartree-Fock theory proposes a way of handling the interaction between electrons. It assumes that each electron moves in an averaged potential defined by all other electrons. The total wavefunction (for a system with N elec-

trons) can then be written as an antisymmetrized product of N one-electron wavefunctions and is usually expressed as a determinant called a Slater determinant.

$$\psi_{HF} = \frac{1}{\sqrt{N!}} \begin{vmatrix} \psi_1(1) & \psi_2(1) & \dots & \psi_N(1) \\ \psi_1(2) & \psi_2(2) & \dots & \psi_N(2) \\ \vdots & \vdots & \ddots & \vdots \\ \psi_1(N) & \psi_2(N) & \dots & \psi_N(N) \end{vmatrix} \tag{2.9}$$

In this determinant, each element depicts a one-electron wavefunction which is referred to as a molecular orbital (MO). Each row correlates to a particular electron. Since the wavefunction is expressed as a determinant, it is antisymmetric with respect to exchange of any pair of electrons and hence follows the Pauli principle. The next task is to find expressions for molecular orbitals. The Linear Combination of Atomic Orbitals (LCAO) method can be used to construct molecular orbitals ψ_i from the atomic orbitals.

$$\psi_i = c_A\phi_A + c_B\phi_B + \dots \tag{2.10}$$

In the above equation 2.10, ϕ_A and ϕ_B are atomic orbitals and c_A and c_B are their coefficients in the expansion of ψ_i.

The variation theorem can be used to minimize the energy and find the optimum wavefunction. Since the wavefunction is expressed in terms of one-electron molecular orbitals which are in turn given as linear combinations of atomic orbitals, optimising the coefficients of atomic orbitals in equation 2.10 can help us achieve the minimum energy. The Hartree-Fock equations are used to optimise these coefficients.

$$\hat{f}_i\psi_a(i) = \varepsilon_a\psi_a(i) \tag{2.11}$$

In equation 2.11, for electron i in spin-orbital a, ψ_a is the one-electron eigenfunction and ε_a is the energy eigenvalue of the one-particle operator $\hat{f}_i$ which is called the Fock

operator.

$$\hat{f}_i = \hat{H}_i + \hat{G}_i \tag{2.12}$$

$$\hat{H}_i = -\frac{1}{2}\nabla_i^2 - \sum_A^M \frac{Z_A}{r_{iA}} \tag{2.13}$$

$$\hat{G}_i = \sum_b [2\hat{J}_b(i) - \hat{K}_b(i)] \tag{2.14}$$

The one-electron Hamiltonian $\hat{H}_i$ in the Fock operator $\hat{f}_i$ consists of kinetic energy and electron-nuclear attraction energy operators. The Hartree-Fock potential $\hat{G}_i$ consists of the Coulomb operator $\hat{J}$ and the exchange operator $\hat{K}$ and is summed over all occupied spin-orbitals.

$$\hat{J}_b(i)\psi_a(i) = \left(\int \psi_b^*(j)\psi_b(j)\frac{1}{r_{ij}} dv_j \right) \psi_a(i) \tag{2.15}$$

$$\hat{K}_b(i)\psi_a(i) = \left(\int \psi_b^*(j)\psi_a(j)\frac{1}{r_{ij}} dv_j \right) \psi_b(i) \tag{2.16}$$

The Coulomb operator describes the influence of charge cloud $\psi_b^*(j)\psi_b(j)$ on electron i. Describing the electrostatic interaction due to interchange of orbitals of electrons i and j, the exchange operator is difficult to understand since it does not have any classical equivalent. Because of a lack of a single defined value at every point in space, the exchange operator is sometimes referred to as a "non-local" quantity. The essence of Hartree-Fock theory is highlighted through these operators. It uses one-electron potentials in which the position of one electron has been averaged in place of two-electron potentials which depend on the instantaneous position of two electrons. It must also be noted that for the case when a = b, the Coulomb and exchange operators are identical.

Given that the Fock operator depends on the orbitals ψ_a (equations 2.15 and 2.16), it is evident that the Hartree-Fock equations cannot be solved directly. Hence, an iterative technique must be employed which involves guessing a starting set of orbitals (or coefficients of atomic orbitals) and solving the Hartree-Fock equations. The solution is then used to generate a new set of orbitals. Until the input and output orbitals are sufficiently

similar, this process is repeated and the method is known as the "Self-consistent field" (SCF) method.

Since Hartree-Fock theory assumes that an electron is only affected by the average position of the other, it allows electrons to approach each other more closely than they should at any given point. Hence, the theory ignores the correlated movement of each electron with every other. This limitation paves way for other electronic structure methods like Density Functional Theory, which introduces the effect of correlation through the Hamiltonian and post-Hartree-Fock methods, that expand the wavefunction beyond the Hartree-Fock single determinant.

2.1.3 Density functional theory

The wavefunction, dependent on three spatial coordinates and one spin coordinate for every electron, is not by any means easily interpretable and intuitive for systems with multiple electrons. Density functional theory (DFT) attempts to replace this wavefunction with something more tangible - the electron density which is only a three-dimensional variable. The theory demonstrates the use of this function to obtain observables like energy. Two theorems by Hohenberg and Kohn [16] form the theoretical backbone of contemporary DFT:

- The energy is uniquely defined by the electron density, ρ.
- The ground-state energy can be obtained variationally: the density that minimises the total energy is the exact ground-state density.

These theorems are important since they prove that electron density can be used to obtain the ground state energy. However, they do not tell us how the electron density can be used to find the ground state energy. One way of finding the molecular energy using only electron density is to assume the system to be classical. In this case, the potential energy

can be given as:

$$V[\rho(r)] = \frac{1}{2}\int\int \frac{\rho(r_1)\rho(r_2)}{|r_1 - r_2|} dr_1 dr_2 - \sum_{k}^{nuclei} \int \frac{Z_k}{|r - r_k|}\rho(r) dr \tag{2.17}$$

In the above equation, the first term is the self-repulsion of a classical charge distribution where r_1 and r_2 are integration variables running over all space and the second term is the attraction between the density and the nuclei.

Expressing the kinetic energy of a system in terms of the electron density is slightly more challenging. Thomas and Fermi in 1927 used fermion statistical mechanics to come up with an expression for the kinetic energy of a specific system. This system was made up of an infinite number of electrons moving in an infinite volume of space with a uniformly distributed positive charge.

$$T[\rho(r)] = \frac{3}{10}(3\pi^2)^{2/3} \int \rho^{5/3}(r) dr \tag{2.18}$$

In the expressions of potential and kinetic energy (2.17 and 2.18), the terms depend on density, which itself is a function of three spatial coordinates. Hence, these terms are called density functionals (since they are functions whose arguments are also functions). The Thomas-Fermi equations were one of the earliest attempts of computing the energy of a system without using the wavefunction. However, they have no applications in contemporary chemistry due to their inaccurate assumptions.

In order to improve the accuracy of kinetic energy calculation, exact expressions in terms of orbitals are used. Considering a system of N non-interacting electrons:

$$T_0 = \sum_{i}^{N} \langle \psi_i | -\frac{1}{2}\nabla^2 | \psi_i \rangle \tag{2.19}$$

$$\rho(r) = \sum_{i}^{N} |\psi_i(x)|^2 \tag{2.20}$$

Kohn and Sham developed a methodology wherein the electron density is modelled as a system of fictitious non-interacting electrons which occupy the 'Kohn-Sham orbitals' and reproduce the real density. Hence, the kinetic energy expression 2.19 can be used. The total energy is given as:

$$E[\rho(r)] = T_0[\rho(r)] + \frac{1}{2}\int\int \frac{\rho(r_1)\rho(r_2)}{|r_1 - r_2|} dr_1 dr_2 - \sum_k^{nuclei} \int \frac{Z_k}{|r - r_k|}\rho(r) dr + E_{xc}[\rho(r)] \tag{2.21}$$

In the above expression, E_{xc} is called the exchange-correlation energy. It contains the correction to the kinetic energy deriving from the interacting nature of the electrons, and all non-classical corrections to the electron–electron repulsion energy.

This leads to a set of 1-electron Kohn-Sham equations which can be solved iteratively using the self-consistent method like the Hartree Fock equations:

$$\hat{H}_{KS}\psi_i(r) = \epsilon_i \psi_i(r) \tag{2.22}$$

$$\hat{H}_{KS} = -\frac{1}{2}\nabla_i^2 - \sum_k^{nuclei} \frac{Z_k}{|r_i - r_k|} + \int \frac{\rho(r')}{|r_i - r'|} dr' + V_{xc} \tag{2.23}$$

V_{xc} is called the exchange-correlation potential. Its exact form is not known, but there are several approximations for this potential which give rise to a range of exchange-correlation functionals.

2.1.3.1 Exchange-correlation functionals

The major challenge for the successful implementation of DFT is finding an accurate approximation for the exchange-correlation functional. The Local Density Approximation (LDA) is a straightforward approximation where the value of the exchange-correlation energy at some point can be computed solely from the value of density at that point.

$$E_{xc}^{LDA}[\rho] = \int \rho(r)\epsilon_{xc}(\rho(r)) dr \tag{2.24}$$

In the above equation, ϵ_{xc} is the exchange-correlation energy per particle. It can be written as a sum of the individual exchange and correlation terms.

The LDA functionals based on the uniform electron gas model have been somewhat successful. The advantage of using this model stems from the fact that the description of exchange-correlation energy functionals is accurate for this model. The uniform electron gas model can provide a rational description of simple metals but not for molecules where the electron density is not homogeneous. Hence, for chemical applications, the local density approximation is not sufficiently accurate. Its accuracy can be improved by incorporating the gradient of the density which accounts for the extent to which the density is locally changing. Similar to including the first two terms of the Taylor expansion of electron density, the exchange-correlation energy for this Generalized Gradient Approximation (GGA) is given as follows:

$$E_{xc}^{GGA}[\rho] = \int \rho(r)\epsilon_{xc}(\rho(r), \nabla\rho(r))dr \tag{2.25}$$

A number of commonly used functionals like BLYP [17][18] and PBE [19] fall under this category. These functionals often offer sufficient accuracy at a reasonable cost.

GGA functionals have a tendency of over-correcting errors of Hartree-Fock theory. High-spin states are generally favoured by HF theory when dealing with transition metals. GGA functionals on the other hand favour low-spin states. Intuitively, these two methods have been combined to give "hybrid functionals". In these functionals, part of the electronic exchange is given as in Hartree-Fock theory and a DFT functional is used to deal with correlation. B3LYP [20][18] is one of the most commonly used hybrid functional. These functionals can be composed in a number of ways.

$$E_{xc}^{hybrid} = \alpha E_x^{GGA} + (1-\alpha)E_x^{HF} + E_c^{GGA} \tag{2.26}$$

The above expression shows a simple hybrid functional where a fraction of the GGA

exchange energy has been replaced by that from HF theory. For PBE0, a functional which uses PBE as the GGA basis, the value of α is 0.25. [21] This value of α comes from perturbation theory. However, based on theoretical grounds or fitting results to experimental data, different parameterizatons are possible. Three such parameters are used in the popular functional B3LYP [20].

Development of new and more accurate functionals is an ongoing area of research. By including more terms of the Taylor expansion of electron density, attempts have been made to get improved functionals. Meta-GGA functionals have also been developed which include the Laplacian of the density or the kinetic energy density. Like using HF exchange in hybrid functionals, MP2 theory can be used to describe the correlation term. Since the exact exchange-correlation fuctional remains unknown, any of these methods might accurately describe a chemical system. However, a functional that works well for a variety of systems at a reasonable cost would be ideal.

2.1.4 Post-Hartree-Fock methods

In Hartree-Fock theory, the wavefunction, being an antisymmetric product of all occupied one-electron orbitals in the system, is expressed as a Slater determinant. The existence of these one-electron orbitals is a consequence of the mean-field approximation where one electron is influenced only by the average position of the other. As stated earlier, this leads to uncorrelated motion of electrons which renders HF theory inaccurate and creates a need of including electron correlation.

The electronic configuration of a system is reflected in the Slater determinant. For the ground state of He atom, the Slater determinant is given as:

$$\Psi_{He} = \frac{1}{\sqrt{2}} \begin{vmatrix} \phi_{1s}(1)\alpha(1) & \phi_{1s}(1)\beta(1) \\ \phi_{1s}(2)\alpha(2) & \phi_{1s}(2)\beta(2) \end{vmatrix} \tag{2.27}$$

$$= \frac{1}{\sqrt{2}}(\phi_{1s}(1)\phi_{1s}(2)) \times (\alpha(1)\beta(2) - \beta(1)\alpha(2)) \tag{2.28}$$

This wavefunction incorporates the possibility of one electron being spin-α and the other spin-β and vice versa. For open shell systems, wavefunctions can often not be described by a single Slater determinant. For the open-shell singlet excited state of He:

$$\Psi^*_{He} = \frac{1}{2}(\phi_{1s}(1)\phi_{2s}(2) + \phi_{1s}(2)\phi_{2s}(1)) \times (\alpha(1)\beta(2) - \beta(1)\alpha(2)) \tag{2.29}$$

$$= \frac{1}{2}\begin{vmatrix} \phi_{1s}(1)\alpha(1) & \phi_{2s}(1)\beta(1) \\ \phi_{1s}(2)\alpha(2) & \phi_{2s}(2)\beta(2) \end{vmatrix} - \frac{1}{2}\begin{vmatrix} \phi_{1s}(1)\beta(1) & \phi_{2s}(1)\alpha(1) \\ \phi_{1s}(2)\beta(2) & \phi_{2s}(2)\alpha(2) \end{vmatrix} \tag{2.30}$$

The wavefunction cannot be described by either of these determinants alone. The first determinant describes the α electron in ϕ_{1s} and β in ϕ_{2s}. The second determinant describes the opposite scenario. Hence, we need both of these determinants to describe the configuration. Such a linear combination is called a "configuration state function" (CSF).

Other configuration state function can be added to expand our wavefunction which makes the wavefunction more flexible, while still retaining the one-electron orbitals. This method is called "configuration interaction" (CI) method since it is similar to mixing excited electronic states into the ground state. The resulting wavefunction is then a linear combination of CSFs whose coefficients need to be optimized. Efforts to include all possible CSFs in the wavefunction are futile for all but the smallest systems because such a calculation would be equivalent to the many-body problem and will scale exponentially with the number of electrons. Therefore, one must decide which CSFs should be included in the wavefunction. This is reasonable since the contribution of very high energy states to the wavefunction will usually not be significant. By including states that describe the excitation of a few electrons, one can curtail the expansion. An example of such a technique is the "CISD" method where all single and double excitations are included. The use of CI in this form is limited due to a poor cost-accuracy tradeoff.

2.1.4.1 CASSCF

The description of a wavefunction with a single Slater determinant may be insufficient for systems with low-lying excited states which can be attributed to the quantum mechanical mixing of states. It is important that these states are accounted for in the description of the wavefunction and is usually dealt with a multiconfigurational self-consistent field (MC-SCF) approach. This is often the case for first row transition metal complexes with weak metal-ligand bonds and molecules undergoing bond dissociation. The weak Mn-Mn bonds in many of the clusters to be discussed lie close to this dissociation limit, and the use of MC-SCF methods in this context will be illustrated in Chapter 5. The complete active space self-consistent field (CASSCF, or CAS) method, where the orbitals of a molecule are divided into three categories, falls into this category of MC-SCF methods.

1. Occupied - Doubly occupied orbitals
2. Active - Orbitals with all possible occupation numbers with significant contribution to the multiconfigurational character of the wavefunction
3. Virtual - Vacant orbitals

With an active space containing m electrons in n orbitals, CASSCF calculations are represented as CAS(m,n). In such a calculation, the occupied orbitals are treated with HF theory. Allowing all possible arrangements of electrons in the active space, the orbitals and configuration state function coefficients are optimized.

An important feature of the CASSCF method is state averaging. Since this method is designed for systems with low-lying excited states that have a significant contribution to the ground state wavefunction, it can be beneficial to use orbitals that are constructed by averaging over a given set of excited states. The choice of these excited states depends on the system being studied and the aim of the calculation. It is also possible to only use the ground state or a single excited state to construct the orbitals.

The aim of post-Hartree-Fock methods is to overcome the limitations of the Hartree-Fock method by incorporating electron correlation. Hence, the expression for correlation energy is given as:

$$E_{corr} = E^{exact} - E^{HF} \tag{2.31}$$

Electron correlation can be divided into static and dynamic correlation. The main error in the Hartree-Fock mean field approximation stems from disregarding the correlated motion of each electron with every other. This type of correlation is called dynamic correlation. Static correlation arises due to the single-determinant description of the wavefunction for systems with degenerate or near-degenerate electronic configurations. It is also referred to as non-dynamic correlation. It is important to understand the difference between the two as it can help in selecting an appropriate theoretical method. CASSCF method only deals with static correlation. However, in order to get accurate energy values, dynamic correlation must also be considered. Perturbation theory corrections are often applied to account for dynamic correlation. An example of such a method which uses perturbation theory to calculate this energy correction is the CASPT2 method.

2.1.4.2 RASSCF

In a lot of cases it is required to restrict the number of electronic excitations in the active space. This is because CASSCF calculations become exceedingly expensive as the size of the active space increases. Hence, it becomes necessary to remove configurations that hardly contribute to the wavefunction. Restricted active space self-consistent field (RASSCF) is a method that imposes restrictions on the active space. It divides the occupied molecular orbitals into two broad groups: inactive orbitals, which are always doubly occupied, and active orbitals. The active orbitals are further divided into three categories: RAS1, 2 and 3. RAS1 orbitals are doubly occupied. However, a maximum number of holes are permitted in this subspace. RAS2 contains orbitals with all possible occupations. RAS3 has unoccupied orbitals. A maximum number of electrons are permitted in

this subspace. CASSCF calculations can be carried out by only adding orbitals to RAS2.

2.1.4.3 GASSCF

Generalized active space self-consistent field (GASSCF) is another method that imposes restrictions on the active space. The active space is partitioned into an arbitrary number of smaller sub-groups (GAS1, GAS2, ..). We specify the accumulated minimum and maximum numbers of electrons for GAS1, GAS1+GAS2, GAS1+GAS2+GAS3, etc. There are no restrictions on excitations within a sub-group. However, restrictions can be imposed on excitations between these groups.

Provided the sub-spaces are chosen correctly, this method can allow one to access large active spaces. This is particularly useful for doubly-doped silicon clusters presented in subsequent chapters where there is a possibility of "left-right" correlation between electrons on the two metal centers in addition to the "in-out" correlation in the metal-silicon bonds.

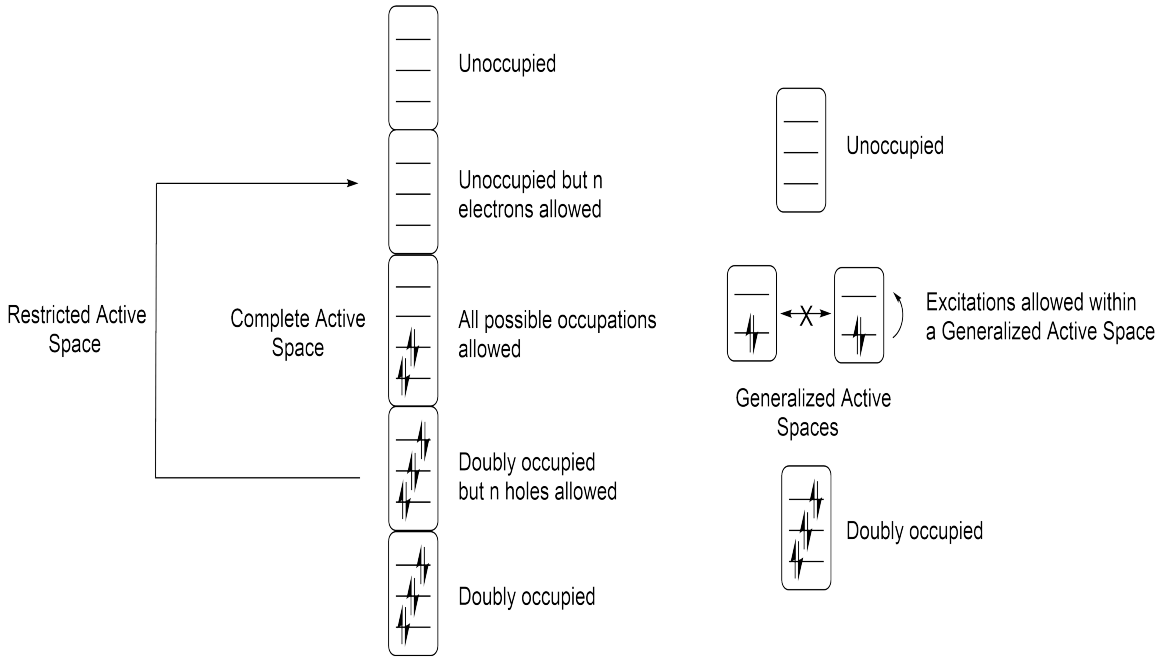


Figure 2.1: Representation of restricted, complete and generalized active spaces.

2.1.5 Basis functions

The methods described in the previous sections lay out ways to calculate the electronic structure of chemical systems. All these methods require a set of basis functions. All molecular orbitals and wavefunctions are constructed using these functions.

2.1.5.1 Slater-type orbitals

The description of orbitals obtained from the solution of the Schrödinger equation for hydrogen atom offers an intuitive starting point for composing basis functions. For such hydrogenic orbitals, the radial part depends on distance as:

$$\psi(r) \propto L(r)e^{-\alpha(r)} \tag{2.32}$$

In the above expression, L(r) are the Legendre polynomials that depend on the quantum numbers of orbitals and decide the number of radial nodes. Slater-type orbitals (STOs) are similar to such hydrogenic orbitals:

$$\psi^{STO}(r) = Nr^{n-1}e^{-\zeta r} \tag{2.33}$$

where N is the normalization constant, n is the principal quantum number and ζ is a measure of how contracted the function is. In very simple (minimal) basis sets, ζ is related to Slater's effective nuclear charge, which controls radial behaviour, and can be calculated using Slater's simple empirical rules.

Such orbitals have the same exponential decay as hydrogenic orbitals. Hence, they are able to reproduce the shape of hydrogenic orbitals close to the nucleus. However, unlike hydrogenic orbitals, STOs do not contain any radial nodes. A single STO is used to model atomic orbitals by a minimal basis. Larger basis tend to use several STOs to describe each atomic orbital. The shape of atomic orbitals can be changed by the inclusion of

polarization functions to the basis set. This can allow one to achieve dumbbell shape for p orbitals, double dumbbell shape for d orbitals and so on as required in a molecule. For instance, to allow the s orbital to distort from being perfectly spherical, p-type polarization functions might be added which can help in modelling subtle changes in the wavefunction by providing greater flexibility.

There are a few challenges associated with the use of STOs. They cannot be separated into x, y and z components. Moreover, the products of STOs are often complicated. These issues make computation of two-electron Coulomb and exchange integrals extremely expensive. Hence, STOs are usually not a practical choice for most electronic structure calculations. However, they are used by the Amsterdam Density Functional (ADF) software package.

2.1.5.2 Gaussian-type orbitals

Gaussian-type orbitals (GTOs) have the form:

$$\psi^{GTO}(r) = Nr^l e^{-\zeta r^2} \tag{2.34}$$

where l stands for the orbital angular momentum quantum number.

These orbitals differ from Slaters because the exponent decay is $e^{-\zeta r^2}$ instead of $e^{-\zeta r}$. As a consequence, these orbitals decay too rapidly at large r, and fail to reproduce the cusp at the nucleus found in real atomic orbitals. Thus they are less accurate representations of real atomic orbitals. However, GTOs have two major advantages. They are separable in x, y and z directions. Moreover, the product of two GTOs on different centres is just a different GTO centred somewhere in between. These characteristics of GTOs make computation of two electron integrals much easier and help in speeding up calculations.

Even though GTOs offer these mathematical advantages, they do not represent atomic orbitals accurately. In order to tackle this problem, a linear combination of several GTOs

(called primitives) is employed to represent each atomic orbital. Because of their mathematical advantages, it is easier to compute integrals with a large number of GTOs than to compute integrals with STOs. Just like STOs, polarization functions can be added to GTOs. It is also possible to add diffuse functions with very low ζ values to describe weakly bound electrons, particularly for anions. GTOs are used by software packages like ORCA and OpenMolcas. A basis set using GTOs will be employed for GASSCF, RASSCF, RASPT2 and CASPT2 calculations on doubly-doped silicon clusters which will be discussed in subsequent chapters.

2.1.5.3 Size, quality, and notation

Owing to the similarities between Slater-type and hydrogenic orbitals, a Slater-type basis is slightly simple to describe. The size of the basis set is usually given in terms of ζ to refer to the exponents in the STOs. A minimal "single zeta" basis uses one STO per atomic orbital. Similarly, a "double zeta" (DZ) basis describes each atomic orbital with two STOs. Since each valence orbital is separated into multiple basis functions, this is known as "split valence". "TZP" denotes a triple-zeta basis with one polarization function for each atomic orbital.

Gaussian-type orbitals are slightly difficult to describe because several GTOs can be used and multiple basis sets have been developed. Each STO is modelled by n Gaussians in Pople's STO-nG basis sets. Like STOs, split valence basis sets have also been developed for GTOs. Pople split valence basis sets, given as X-YZG, employ X Gaussian primitives for each core orbital. Each valence orbital is split into two basis functions composed of Y and Z primitives respectively. * is used to denote a polarization function, while diffuse functions are given by a $+$. For instance, 6-31+G^* is a double-zeta basis set with one diffuse function and one polarization function for every atomic orbital. Several newer basis sets have been developed which give more accurate results. For example, def2-SVP is a Karlsruhe "def2" basis set [22] with double zeta and polarization. def2-TZVP is a triple

zeta basis set with polarization. Diffuse functions are denoted by D. Since a large basis set allows the wavefunction to be constructed to a finer level of detail, it can give better results than a smaller one.

2.1.5.4 Core electrons

Core orbitals of large atoms do not generally participate in bonding because of their close proximity to the nucleus. For atoms with few electrons, it is possible to include all electrons in calculations. This is usually not the case for heavier atoms. For such atoms, only the valence orbitals are described while the core orbitals are treated approximately which reduces the cost of the calculation significantly while maintaining sufficient accuracy. There are two ways to model the cores of heavy atoms. In the first method, calculations include all electrons but do not involve optimisation of core orbitals in the SCF process. This is called the "frozen core" approximation. The second method uses an electrostatic object located around the nucleus to model the nucleus and the core. Valence electrons interact with this object (called "pseudopotential"). Calculations employing Slater and Gaussian type orbitals can use both of these methods.

2.2 Molecular Symmetry

In one of the previous sections, molecular orbitals were constructed with the linear combination of atomic orbitals (LCAO) method. The symmetry properties of molecules can be used to describe their electronic structure. Group theory and matrix algebra provide the mathematical justification behind this property. In the study of clusters presented in subsequent chapters, symmetry analysis plays an important role. Moreover, the Amsterdam Density Functional (ADF) software package makes extensive use of symmetry. Hence, it is important to understand principles of molecular symmetry. Symmetry also simplifies multiconfigurational self-consistent field (MC-SCF) calculations. This will be discussed in

the chapter on GASSCF calculations of doubly doped silicon clusters. The role of symmetry will again be highlighted while discussing the vibrational modes of these clusters. Molecules can possess different kinds of symmetries like rotational, reflective and so on. A symmetry operation refers to a transformation that leaves the molecule unchanged. For example, a 180° rotation is a symmetry operation for water molecule since it leaves the molecule unchanged. The axis of rotation is the symmetry element for the 180° rotation symmetry operation in water. A specific combination of symmetry elements possessed by a molecule defines a point group. Since a point group is a mathematical group, the corresponding symmetry elements follow the postulates of group theory. This allows us to extend the results of group theory to chemical systems. In a point group, a function of space can only transform in a finite number of ways under the symmetry operations of the group. Each of these ways is called an "irreducible representation", or "irrep". The "totally symmetric irreducible representation" (TSIR) is present in each group. As the name suggests, it is symmetrical under every operation in the group. At the beginning of any electronic structure calculation for a molecule, the effect of each symmetry operation on every valence orbital of constituent atoms is considered. Subsequently, the group of valence orbitals is represented by a sum of irreps which enables the construction of molecular orbitals of particular symmetries through linear combinations of appropriate atomic orbitals.

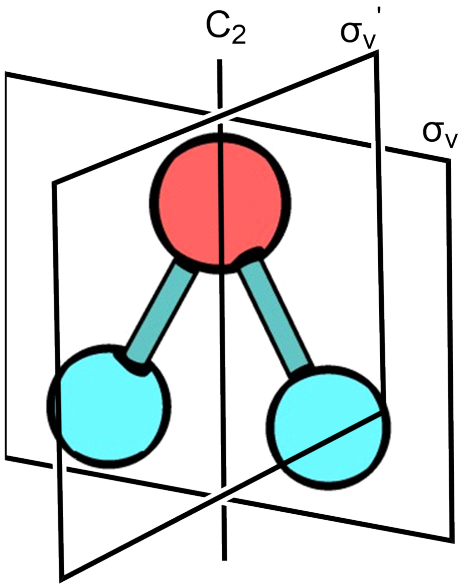


Figure 2.2: Symmetry elements of a water molecule.

A water molecule has three symmetry operations in addition to the trivial identity (E). A 180 ° rotation axis (C_2), a mirror plane containing all atoms (σ_v), and another perpendicular mirror plane encompassing only the oxygen atom ($\sigma_v^{'}$) are the symmetry elements. Hence, water has a C_{2v} point group which is defined by these symmetry elements. Table 2.1 gives the character table for this point group. It gives information about the group. In the top row of this table, the symmetry operations are shown. The first column gives the irreducible representations of the group. For each irrep, there is an associated number for every symmetry operation, called its character. Under an operation, a character of 1 represents that the irrep is symmetric while -1 means that it is anti-symmetric. For example, a_1 is symmetric under all symmetry operations. Hence it is the totally symmetric irreducible representation. In the atomic orbitals of constituent atoms of water, the s

	E	C_2	σ_v	$\sigma_v^{'}$
a_1	1	1	1	1
a_2	1	1	-1	-1
b_1	1	-1	1	-1
b_2	1	-1	-1	1

Table 2.1: Character table for the C_{2v} point group.

orbital on oxygen is unchanged by all symmetry operations and transforms as a_1. Similarly, the $2p_z$ orbital is also unchanged by all operations. Hence, it also transforms as a_1. The $2p_x$ orbital changes sign under a two-fold rotation. It also changes sign when reflected through the yz-plane, but remains unchanged when reflected in the xz-plane. Hence, the characters of the $2p_x$ orbital are 1, -1 ,1 and -1. Thus, it transforms as b_1. Following the same analysis for the $2p_y$ orbital tells us that it transforms as b_2. The 1s orbitals on both hydrogen atoms are considered together because the individual orbitals do not have all symmetries of the point group. These orbitals span two irreducible representations:

$$\Gamma_{H1s} = a_1 + b_2 \tag{2.35}$$

These can be assigned to the in-phase and out-of-phase combinations. The in-phase combination is unchanged by all symmetry operations, so it transforms as the totally symmetric irreducible representation. The out-of-phase combination has b_2 symmetry. Since such combinations allow the hydrogen 1s basis to be expressed as a sum of two irreps, they are called symmetry-adapted linear combinations (SALCs).

Symmetry-adapted linear combinations can only interact with each other if they have the same symmetry species. This property allows us to identify the oxygen SALCs which can interact with hydrogen SALCs in water. Both in-phase combination of H 1s orbitals and oxygen $2p_z$ orbital have a_1 symmetry. Hence, they can interact to give bonding and anti-bonding combinations. Similarly, the out-of-phase combination of hydrogen 1s orbitals can interact with the $2p_y$ orbital on oxygen. The $2p_x$ orbital on oxygen remains non-bonding since its symmetry does not match with any combination of hydrogen 1s orbitals. Using this analysis, a molecular orbital diagram for H_2O can be constructed and is shown in Figure 2.3.

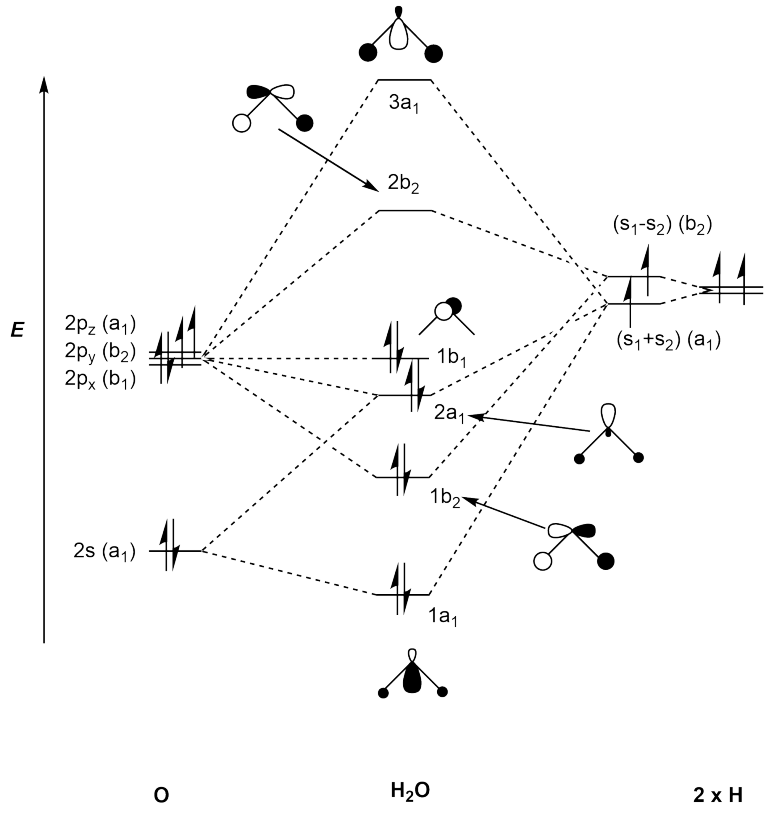


Figure 2.3: Molecular orbital diagram of H_2O.

2.3 Vibrational Frequencies

Calculation of the vibrational spectra of clusters forms an important part of subsequent chapters. The harmonic oscillation model is used to calculate molecular normal modes. In its equilibrium geometry, a molecule is located at the minimum of the potential energy surface (PES). At this point, the cross-section of the PES can be assumed to be nearly parabolic which allows the second derivative of energy with respect to a nuclear coordinate to be taken as a force constant for the harmonic oscillation of an atom along this coordinate. For polyatomic molecules this model is generalized to several nuclear coordinates. The normal modes and frequencies are the eigenvectors and eigenvalues of the force constant matrix called the Hessian:

$$H_{ij} = \frac{\partial^2 E}{\partial R_i \partial R_j} \tag{2.36}$$

Analytical calculations of Hessian are somewhat rare. It can be constructed by numerical differentiation of the energy gradients but this is often very time-consuming.

The IR intensities can also be calculated using the dipole gradients.

$$I_{IR} = \frac{N\pi}{3c^2} \sum_{\alpha} \left(\sum_{j} \frac{\partial \mu_\alpha}{\partial R_j^m} Q_j^m \right)^2 \tag{2.37}$$

In the above expression, the x, y and z components of the dipole moment μ are denoted by α and the mass-weighted vibrational normal mode is given as Q^m [23, 24, 25].

Chapter 3

Evolution of Vibrational Spectra in the Manganese-Silicon Clusters Mn_2Si_n, n = 10, 12, 13, and cationic $[Mn_2Si_{13}]^+$

3.1 Introduction

Over the past two decades, the spectroscopy and electronic structure of endohedral clusters of silicon have been explored from both experimental and computational perspectives, the ultimate goal being to understand how the electronic properties of the metal impact on the cluster and *vice versa*.[26, 27, 28] Beyond the intrinsic interest in the nature of the chemical bonds in these clusters, they can be viewed as minimal models for transition metals impurities in bulk silicon, an issue of considerable significance in the semiconductor industry. From the outset, this family of clusters has challenged conventional models of chemical bonding, and the emergence of Density Functional Theory (DFT) as a viable means of exploring potential energy surfaces has provided a platform for many studies that

seek to link structure and spectroscopy to composition. There is, however, still no clear consensus on what the "best" functional is for clusters of this type, and the choice is often motivated by the authors' previous success in related studies. The influence of Hartree-Fock exchange (present in hybrid functionals such as the popular B3LYP) on the computed energies of different spin states is well documented: larger proportions of Hartree-Fock exchange tend to favour unpaired spin density, and hence higher multiplicities.[29] Less well documented, but of particular relevance here, is the fact that even when the multiplicity is fixed, functional choice can have a substantial impact on the relative energies of different local minima, particularly in cases where the nature of the chemical bonding differs qualitatively between them. In the family of M@Si_{14} clusters (where M is the encapsulated metal dopant), for example, the BLYP functional (and its hybrid, B3LYP) tends to favour "open" structures with three-connected vertices while the PBE functional (and its hybrid, PBE0), in contrast, stabilizes deltahedral structures with more highly connected vertices.[30] These structural differences mark a transition between localised σ/π bonding (similar to that in the carbon-based fullerenes) in the "open" structures to multi-centre delocalised bonding typical of the heavier group 14 elements in the deltahedral alternatives. The balance between these two paradigms appears to be particularly delicate in silicon clusters, leading to extreme sensitivity of the relative energies of the different isomers to the choice of functional.[30, 27, 26, 31, 32, 10, 33, 8, 34, 35, 36, 28] Multiconfigurational self-consistent field (MC-SCF) techniques are increasingly being used as an alternative to DFT in studies of these clusters, but the balanced treatment of static and dynamic correlation required to compute meaningful energies remains a challenge.[37, 15, 38, 39, 40, 41, 42, 43, 44]

Given the inherent difficulties in calculating relative energies, an alternative strategy is to compare computed spectroscopic fingerprints for various candidate structures to a measured spectrum. This approach has been used with some success in the context of vibrational, [13] photo-electron,[45, 46, 47, 48, 49, 50, 11, 51, 52] and X-ray absorption spectroscopies,[12] and underpins much of our current understanding of these clusters.

In this chapter, the majority of which has been published in *The Journal of Physical Chemistry A* [53], we use DFT as a tool to interrogate the vibrational signatures of a series of mass-selected manganese-doped silicon clusters, Mn_2Si_{10}, Mn_2Si_{12} and Mn_2Si_{13}, along with cationic $[Mn_2Si_{13}]^+$. The strong electron-electron repulsions within the 3*d* orbitals of the first-row transition metals are a particular challenge to DFT, and these are compounded in this case by the presence of two Mn atoms and hence the possibility of metal-metal bonding. As a result, studies of this general class of clusters have only begun to emerge in the last few years.[54, 55, 56, 57, 58, 14, 59, 60, 61, 62, 63, 64] Through careful comparison between experiment and theory across the Mn_2Si_x series, we can identify the most plausible structural candidates that are consistent with the available data. Moreover, by identifying common symmetry elements, we can trace the evolution of vibrational modes through the series and connect these observations to the underlying patterns of electronic structure.

3.2 Methodology

3.2.1 Experimental Techniques

All spectroscopic measurements were performed by our collaborators, Pieterjan Claes, Ewald Janssens and Peter Lievens from KU Leuven, Belgium and André Fielicke from Fritz-Haber-Institut der Max-Planck-Gesellschaft, Germany. This data was submitted by Pieterjan Claes as part of his PhD thesis at KU Leuven. These measurements are performed in a molecular beam setup[65] coupled to a beamline of the Free Electron Laser for Infrared eXperiments (FELIX) user facility.[66] The clusters are produced in a dual-target dual-laser vaporization cluster source by pulsed ablation of manganese and silicon plate targets.[67] Cluster–xenon complexes are formed by condensation of the vaporized material in a short pulse of He gas containing a fraction (2.5%) of isotopically enriched ^{129}Xe and cooled in a thermalization channel attached to the source (115 K). Resonant

absorption of IR light heats the cluster–xenon complexes through internal vibrational redistribution, which may result in dissociation of the complex. Infrared multiple photon dissociation (IR-MPD) spectra are constructed by recording the intensities of the ionic complexes as a function of the FELIX frequency in the 230–560 cm^{-1} range using a time-of-flight mass spectrometer. Neutral clusters are post-ionized, after excitation by the infrared laser and before extraction into the mass spectrometer, using a weakly focused beam of 7.87 eV photons from an F_2 excimer laser.

3.2.2 Computational Techniques

All DFT calculations were performed using the Amsterdam Density Functional (ADF) package, version 2020.103.[25] Slater-type basis sets of triple-zeta and two polarization functions (TZ2P) were used on all atoms.[68] The number of fit functions were increased by adding the subkey 'FitType QZ4P' of the key BASIS and a fine grid was used for numerical integration (keyword 'BECKEGRID Quality good'). The Perdew-Becke-Ernzerhof (PBE)[19] functional was used in all calculations unless stated otherwise. B3P86 was implemented as a LibXC functional with ADF (LibXC is a library of approximate exchange-correlation functionals). All calculations were performed using spin-unrestricted DFT. The initial structures were obtained in two ways: by carrying out literature surveys for reported structures of similar systems (doubly doped silicon clusters) or obtained by adding a second metal atom to previously outlined structures for singly doped silicon clusters. The computed infrared spectra were generated with a Lorentzian line shape of 5 cm^{-1} full width at half maximum. The calculated frequency values were not scaled. A zip folder (Chapter3_Optimized_Coordinates) containing the Cartesian coordinates of all optimized structures can be found in the Oxford University Research Archive (https://doi.org/10.5287/bodleian:QRG2eZvxr).

3.3 Results and Discussion

3.3.1 IR-MPD spectroscopy of Mn_2Si_{10}, Mn_2Si_{12}, Mn_2Si_{13} and $[Mn_2Si_{13}]^+$

IR-MPD spectra of the neutral clusters Mn_2Si_x, x = 10, 12, 13 and cationic $[Mn_2Si_{13}]^+$ are collected in Figure 3.1. The spectra of Mn_2Si_{12} and $[Mn_2Si_{13}]^+$ appear related in so much as both have their most intense feature in the window between 250 and 320 cm^{-1}, and less intense bands between 325 and 400 cm^{-1}. The spectrum of Mn_2Si_{13} also features intense absorptions in the 250-300 cm^{-1} and 375-425 cm^{-1} windows, but the bands are much less distinct. The striking similarities between the spectra suggest that the clusters may share common structural features that determine at least the gross features of the vibrational manifold. The spectrum of Mn_2Si_{12} is also conspicuously similar to that reported previously for $[Co_2Si_{12}]^+$,[69] although the relative intensities of the bands in the low-frequency region (below 300 cm^{-1}) are somewhat lower for the cobalt analogue. The spectrum of Mn_2Si_{10} stands out as being quite different from any of the others: its most intense band is a broad feature centered at $\sim$450 cm^{-1}, with less intense peaks at 260 cm^{-1} and 310 cm^{-1}. Again, these features are mirrored in the published spectrum of $[Co_2Si_{10}]^+$, where a pronounced double peak is centered on $\sim$430 cm^{-1}.[69] This data set is clearly rich in information and, in the following sections, we use DFT to explore the potential energy surface and vibrational properties of these clusters with the aim of establishing the extent to which shared structural characteristics lead to similarities and differences in the measured IR-MPD spectra.

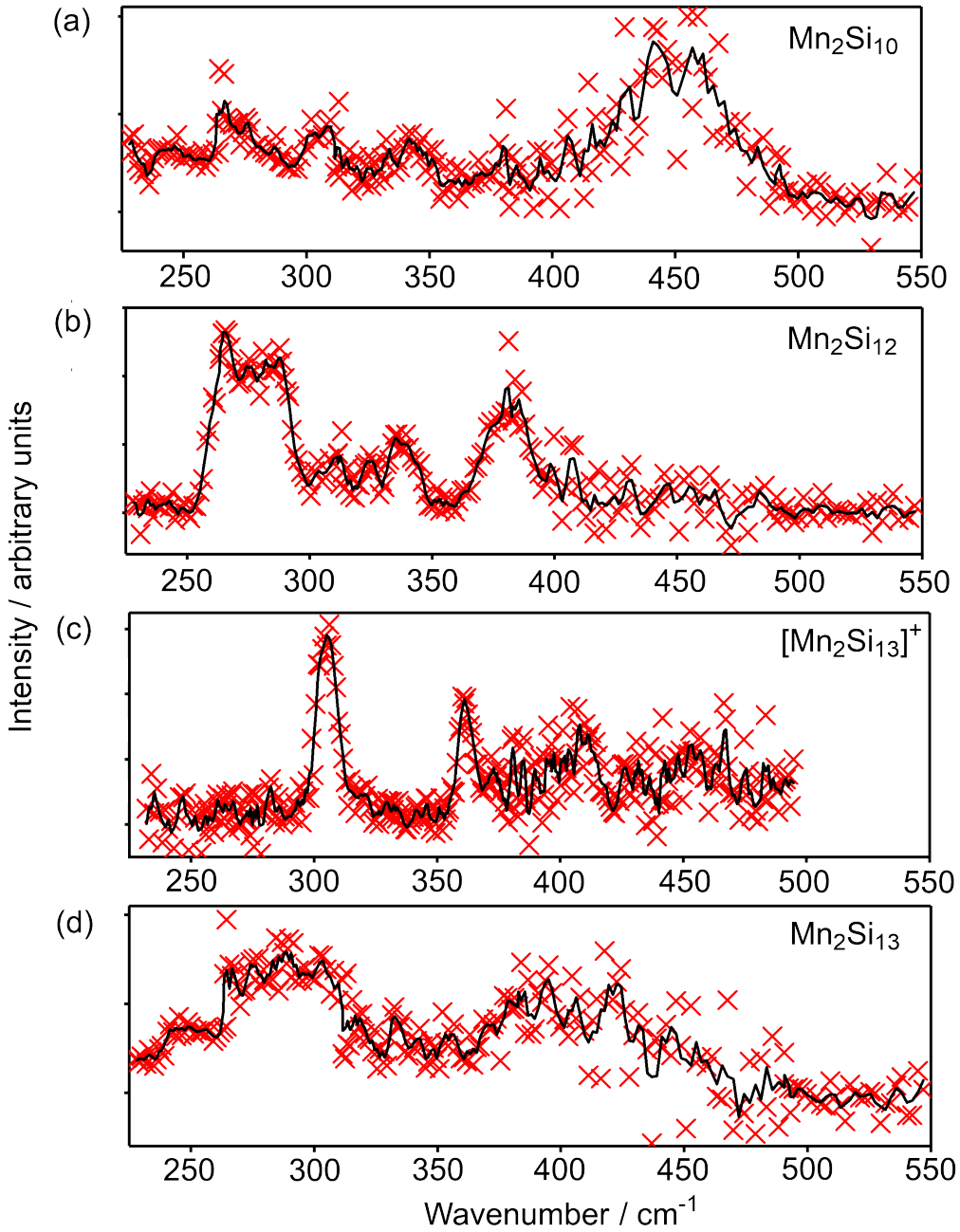


Figure 3.1: IR-MPD spectra of (a) Mn_2Si_{10}, (b) Mn_2Si_{12}, (c) $[Mn_2Si_{13}]^+$ and (d) Mn_2Si_{13} measured by Pieterjan Claes, Ewald Janssens and Peter Lievens from KU Leuven, Belgium and André Fielicke from Fritz-Haber-Institut der Max-Planck-Gesellschaft, Germany. The spectra were measured by monitoring Xe loss from the corresponding Xe-tagged complexes. The experimental data points (red crosses) are overlaid with a three-point running average (black line).

3.3.2 Density Functional Theory

3.3.2.1 Ground-state structure and vibrational spectrum of Mn_2Si_{12}

Our survey of the potential energy surface of Mn_2Si_{12} (using the PBE functional) reveals two low-lying local minima with hexagonal anti-prismatic geometries, one a triplet identified as ^{3}**12** and the other a quintet, ^{5}**12** (Figure 3.2). We have also identified a hexagonal prismatic septet (^{7}**12**). All three isomers have one endohedral Mn and a second one capping a hexagonal face, with either exact or approximate C_{6v} point symmetry. The most stable of these is ^{3}**12**, with the quintet and septet lying 0.59 eV and 1.13 eV higher in energy, respectively. We have also reported the relative Gibbs free energies of different isomers. We observe that these energies follow the same trend as the relative energies. The same hexagonal anti-prismatic structure was identified as the equilibrium structure of the 59/60-electron clusters Mo_2Si_{12} and $[Nb_2Si_{12}]^{-/2-}$.[70, 47] Taken at face value, these data appear quite definitive in identifying the ^{3}**12** isomer as the one observed in the experiment, but we have emphasised above the extreme sensitivity of computed total energies to functional choice. Our choice of the gradient-corrected PBE functional was based on its common usage in group-14 cluster chemistry,[14, 30, 28] but there is a substantial body of work in the field that employs hybrid functionals such as B3LYP or B3P86 rather than gradient-corrected alternatives.[10, 65, 13, 71, 72] To try to unravel the impact of different choices of functional, we have recomputed the energies of the low-lying states of Mn_2Si_{12} using the gradient-corrected functionals BLYP and BP86 and also the hybrids, PBE0, B3LYP and B3P86. In this way, we can separate the influence of the exchange/correlation functional from the effects of Hartree-Fock exchange. The relative energies of the three states, shown in Figure 3.3, reveal a complex picture, where the identity of the ground state is indeed highly dependent on functional choice. Whilst PBE, BLYP, BP86 and B3P86 concur in identifying the ^{3}**12** isomer as the ground state, PBE0 favours the quintet, ^{5}**12**, and B3LYP predicts the hexagonal prismatic septet, ^{7}**12**.

The influence of Hartree-Fock exchange is immediately apparent: it stabilizes the quintet relative to the triplet and the septet relative to the quintet, the result being that the relative energies of the three states are very close for all three hybrids. A second, more subtle, feature is that the LYP correlation functional (in BLYP and B3LYP) stabilizes the $^{7}\mathbf{12}$ isomer by $\sim$0.5 eV relative to the other two, with the result that this isomer emerges as the global minimum only for B3LYP. This is precisely the trend identified previously in the family of M@Si_{14} clusters, where the BLYP functional (and its hybrid) tends to favour "open" structures with three-connected vertices (in this case the hexagonal prism) over those with more highly connected vertices (in this case the hexagonal anti-prism). The trends identified in Figure 3.3 are also apparent in the work of Khanna and co-workers on Fe_2Si_{12}[14] and Liang et al. on $[Cr_2Ge_{12}]^-$.[51] In the first of these, using the PBE functional, the hexagonal anti-prismatic architecture was clearly the most stable whereas in the second, performed with B3P86, the hexagonal prism was identified as a very low-lying transition state that could facilitate rapid rearrangement. Our conclusion here is simply that the calculated total energies using any single functional are a poor criterion on which to base an assignment of the ground-state structure.

The computed IR spectrum of the $^{3}\mathbf{12}$ isomer (the blue spectrum in Figure 3.2) appears to provide a good match to the experimental data. Prominent bands at 272 cm^{-1} and 288 cm^{-1} (both with e_1 symmetry) map on to the broad experimental feature between 260 and 290 cm^{-1}, while the a_1-symmetric modes at 345 cm^{-1} and 385 cm^{-1} are consistent with features at $\sim$340 cm^{-1} and $\sim$380 cm^{-1}, respectively. We show later that the 345 cm^{-1} mode has significant Mn-Mn stretching character and is a direct signature of the presence of the Mn-Mn bond. Although less prominent, an a_1-symmetric vibration at 317 cm^{-1} also corresponds to a less intense experimental feature around 320 cm^{-1}. The $^{5}\mathbf{12}$ isomer shows very similar features, although the splitting of the two low-frequency peaks is rather more pronounced. The $^{7}\mathbf{12}$ alternative also has prominent bands in the 250-300 cm^{-1} region, but the spectrum is devoid of intense features above 350 cm^{-1}, and does

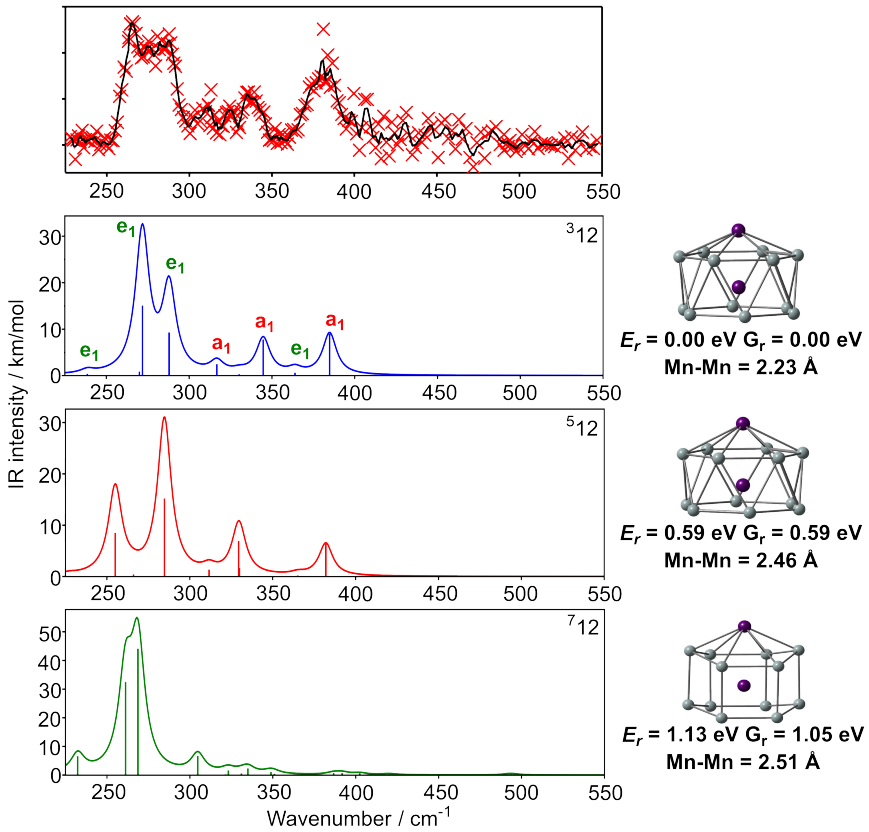


Figure 3.2: IR-MPD spectrum of the Mn_2Si_{12}·Xe complex (intensity in arbitrary units), optimized structures and computed IR spectra of the ^{3}**12**, ^{5}**12** and ^{7}**12** states of Mn_2Si_{12}, all calculated with the PBE functional.

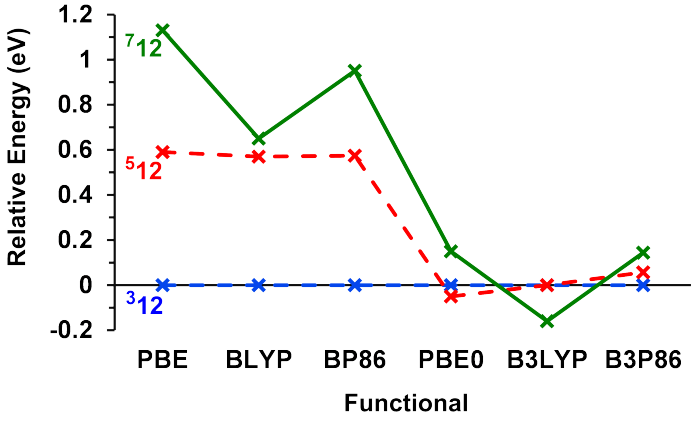


Figure 3.3: Functional dependence of the relative energies of the low-lying states (^{3}**12**, ^{5}**12**, ^{7}**12**) of Mn_2Si_{12}. The ^{3}**12** state (blue) is chosen as the point of reference for all functionals.

not, therefore, offer an obvious assignment for the peak observed around 380 cm^{-1} in the experimental data. On this basis, it seems that the ^{3}**12** isomer is the most plausible

candidate for the experimentally-observed cluster. As a corollary to this observation, the PBE functional (along with BP86 and BLYP) appears to identify the correct ground state isomer while the B3LYP functional does not.

The identification of a triplet ground state in Mn_2Si_{12} indicates that the majority of the intrinsic magnetic moment of the component Mn atoms is quenched. The role of the Si_{12} cage in quenching the moment of the endohedral metal has been explored in detail by Khanna and co-workers in the context of $CrSi_{12}$[7, 8] and also by Arcisauskaite et al. in the context of isoelectronic $[MnSi_{12}]^+$[15]: in short, there is very substantial covalence that delocalizes the electron density onto the cage, favouring spin pairing. As a result, any residual spin moment is localized strongly on the external Mn ion, which is only partially coordinated by one Si_6 hexagon. A spin density plot for Mn_2Si_{12} is shown in Figure 3.4, and the projected Mulliken spin densities (PBE functional) are +2.83 and -0.22 on the external and endohedral Mn centers, respectively, with a further 0.61 spin-β electrons localized on the Si_{12} cage. The Mn-Mn separation of 2.23 Å in the ^{3}**12** ground state is much shorter than typical Mn-Mn single bonds (2.895 Å in $Mn_2(CO)_{10}$, for example[73]) and, whilst bond-length-bond-order correlations are notoriously difficult to establish with certainty when bridging ligands (such as Si_{12}, here) are present, such a short bond is certainly indicative of strong Mn-Mn bonding. The frontier Kohn-Sham orbitals for the triplet ground state in Figure 3.5(a) include a doubly-occupied Mn-Mn σ orbital, $5a_1$ and also a doubly occupied degenerate Mn-Mn π^* orbital, $6e_1\alpha$, and hence a formal Mn=Mn double bond, qualitatively similar to that in O_2. Much like the calculated energies of the various states, these computed Mulliken spin densities (and also the values of $\langle S^2 \rangle$) are extremely sensitive to functional choice, and the corresponding values with the hybrid PBE0 (+4.24 and -2.73 on external and endohedral Mn, respectively), indicate a much more extreme degree of polarization. This striking functional dependence indicates substantial static correlation that we will explore in Chapter 5 using Multiconfigurational SCF techniques.

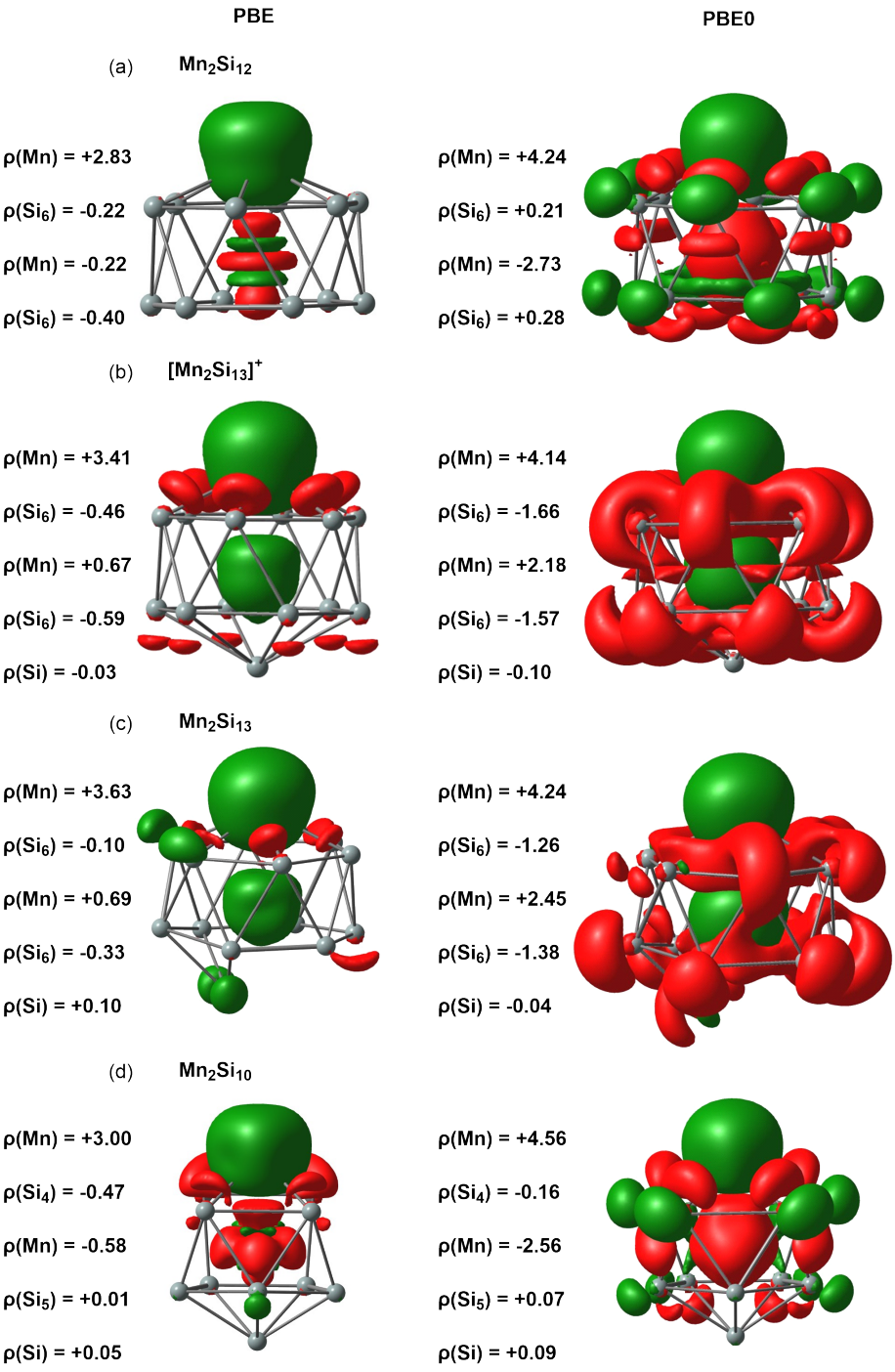


Figure 3.4: Spin density plots and Mulliken projected spin densities of (a) Mn_2Si_{12}, (b) $[Mn_2Si_{13}]^+$, (c) Mn_2Si_{13} and (d) Mn_2Si_{10} (with PBE and PBE0 functionals).

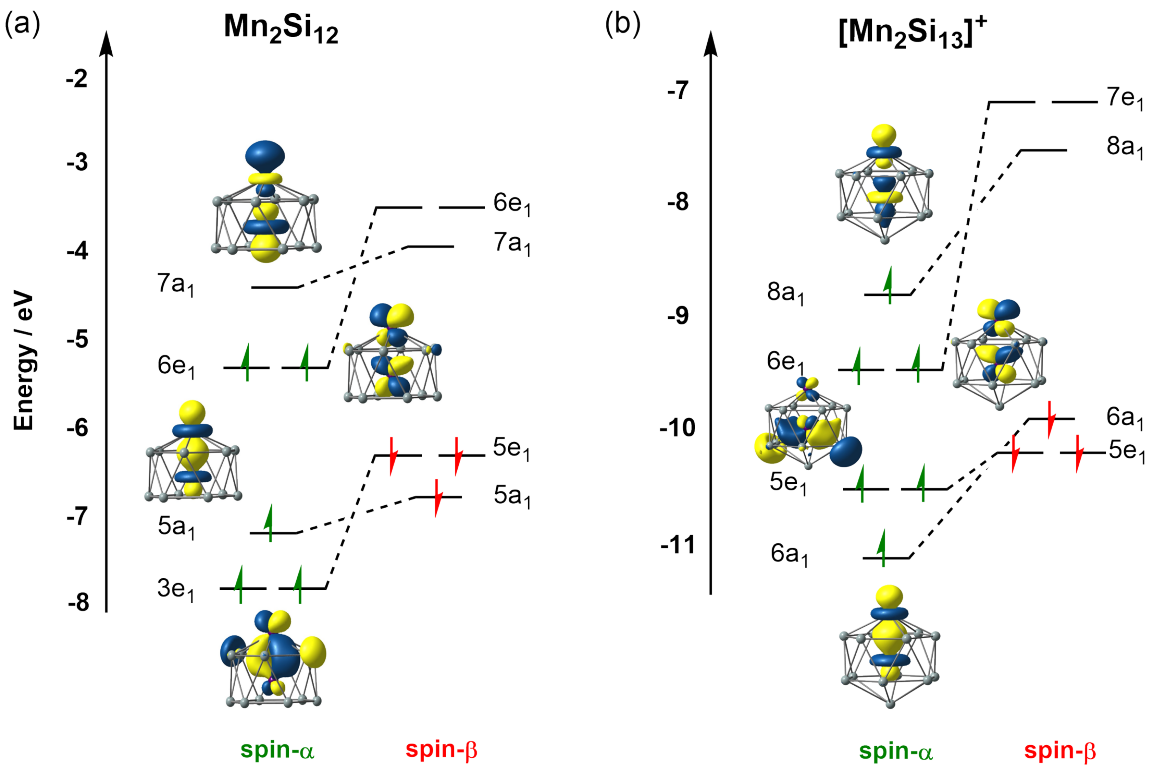


Figure 3.5: Frontier Kohn-Sham orbitals for (a) the ^{3}**12** state of Mn_2Si_{12} and (b) the ^{4}**13**$^{+}$**(a)** state of $[Mn_2Si_{13}]^{+}$.

3.3.2.2 Ground-state structure and vibrational spectrum of $[Mn_2Si_{13}]^+$

The optimized geometries of two low-lying states of $[Mn_2Si_{13}]^+$ are collected in Figure 3.6, along with their computed vibrational fingerprints. The energies reported in the figure relate to the PBE functional, which we adopt, on the basis that it identified the equilibrium structure of Mn_2Si_{12} correctly. Our survey of the potential energy surface identifies as the global minimum a C_{6v}-symmetric isomer, $^4\mathbf{13}^+\mathbf{(a)}$, derived, at least conceptually, from the Mn_2Si_{12} anti-prism by capping the remaining hexagonal face with a Si^+ ion. The axial symmetry again allows for a clean separation of the vibrational peaks into parallel (a_1) and perpendicular (e_1) modes, and the two prominent peaks in the experimental spectrum are readily assigned to the computed modes at 310/315 and 359 cm^{-1}, all of which have e_1 symmetry. The alternative 'prism-like' isomer, $^4\mathbf{13}^+\mathbf{(b)}$, is 0.19 eV higher in energy with the PBE functional, and the computed spectrum of the $^4\mathbf{13}^+\mathbf{(b)}$ isomer offers a significantly worse match to experiment. For this reason we assign the ground state as $^4\mathbf{13}^+\mathbf{(a)}$. It is worth noting, however, that the $^4\mathbf{13}^+\mathbf{(b)}$ is computed to be more stable than $^4\mathbf{13}^+\mathbf{(a)}$ for all other functionals tested (Figure 3.7), again underlining the pitfalls of relying solely on computed relative energies to identify structure. The spin density in the $^4\mathbf{13}^+\mathbf{(a)}$ ground state is again localized strongly on the external Mn ion (+3.41) while the moment at the endohedral metal remains largely quenched (+0.67). The presence of the additional Si atom on the principal axis serves to weaken the Mn-Mn bond compared to Mn_2Si_{12}, and the Mn-Mn σ^* orbital shown in Figure 3.5(b) is now singly occupied. As a result, the Mn-Mn bond length is 2.35 Å, 0.12 Å longer than in Mn_2Si_{12}. Unlike the Mn_2Si_{12} case, there is no obvious signature of the Mn-Mn bonding in the vibrational spectrum: all modes with significant Mn-Mn stretching character are found at very low frequencies and with low intensities, and in fact the only a_1-symmetric mode with substantial intensity (at 419 cm^{-1}) has dominant Mn-Si, rather than Mn-Mn, character. The experimental spectrum above 400 cm^{-1} does not show well-defined peaks, but there is evidence for an increase in intensity at $\sim$410 cm^{-1} that we assign to this mode.

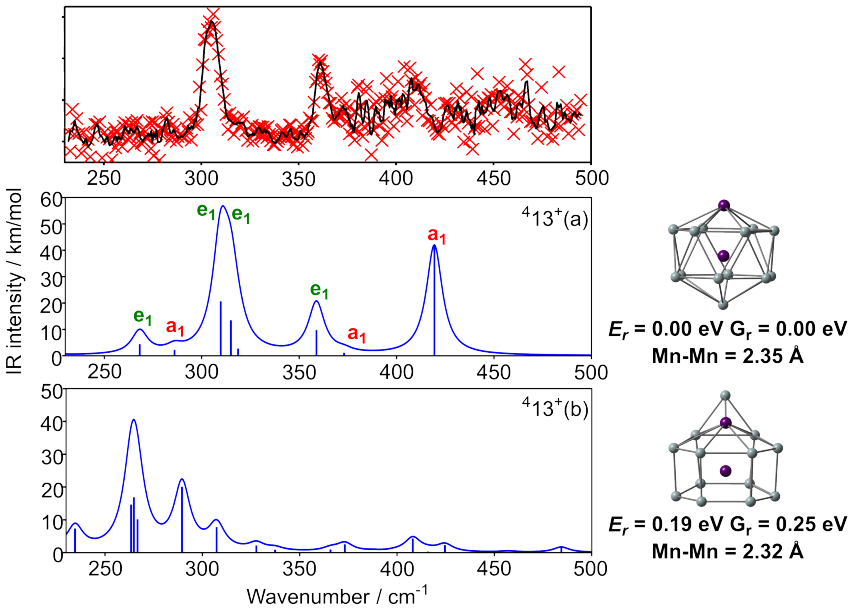


Figure 3.6: IR-MPD spectrum of $[Mn_2Si_{13}]^+$·Xe complex (intensity in arbitrary units), optimized structures and computed IR spectra of the low-lying $^4\mathbf{13}^+$**(a)** and $^4\mathbf{13}^+$**(b)** isomers of $[Mn_2Si_{13}]^+$ (PBE functional)

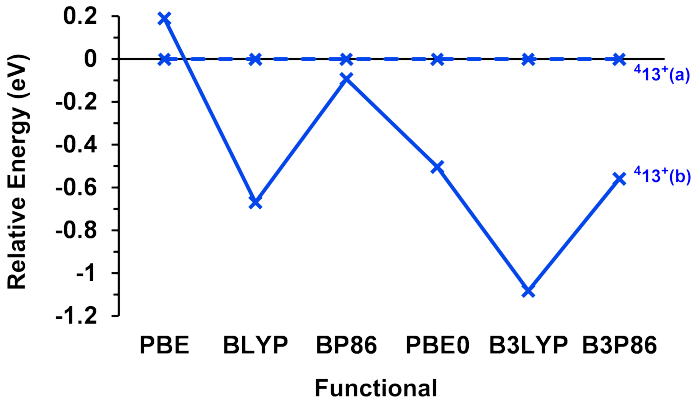


Figure 3.7: Variation of relative energies of different isomers of $[Mn_2Si_{13}]^+$ with different functionals.

3.3.2.3 Symmetry analysis and comparison of Mn_2Si_{12} and $[Mn_2Si_{13}]^+$

The fact that the computed ground states of Mn_2Si_{12} and $[Mn_2Si_{13}]^+$ share a hexagonal anti-prismatic core with a common 6-fold rotation axis allows for a clean separation between modes involving motion along the principal axis and perpendicular to it. The uncapped hexagonal anti-prism, $[MnSi_{12}]^+$, therefore represents a natural reference point

for the following discussion. The $[MnSi_{12}]^+$ cation has been the subject of a number of studies in its own right, and the ground state is in fact a hexagonal prism rather than the anti-prism that we consider here, which is located 0.46 eV higher in energy (PBE). The fact that the hexagonal anti-prism is not the ground state of $[MnSi_{12}]^+$ is not critical here: its role is simply to act as a reference point for the discussion of the capped analogues that are known.

The spectra (experimental and computed) of Mn_2Si_{12} and $[Mn_2Si_{13}]^+$ are compared in Figure 3.8, alongside the computed spectrum of the anti-prismatic isomer of $[MnSi_{12}]^+$. Atomic displacements for the significant vibrational modes are shown in Figure 3.9, where they are separated into parallel (a_1) and perpendicular (e_1) subsets. Modes that feature prominently in the experimental spectrum are enclosed in red boxes. The spectrum of the $[MnSi_{12}]^+$ reference shows many of the features noted above for Mn_2Si_{12} and $[Mn_2Si_{13}]^+$, most notably an intense e_1-symmetric vibration at 277 cm^{-1} that involves the motion of the endohedral Mn in the *xy* plane. There are two further modes of e_1 symmetry that carry significant intensity, at 190 and 364 cm^{-1}, both involving canting of the two Si_6 rings. Amongst the parallel set, an intense b_2-symmetric mode at 314 cm^{-1} involves motion of the Mn atom along the principal axis, coupled to an out-of-phase contraction/expansion of the two Si_6 rings. Although not allowed in the infra-red spectrum of D_{6d}-symmetric $[MnSi_{12}]^+$, modes of a_1 and e_5 symmetry are also shown in the figures because they correlate with a_1 and e_1 modes in C_{6v} symmetry, and so become allowed when capping atoms are introduced in Mn_2Si_{12} and $[Mn_2Si_{13}]^+$. Amongst these, the two a_1-symmetric modes are breathing modes of the Si_{12} cage, either in the *xy* plane (300 cm^{-1}) or along the principal axis (386 cm^{-1}). The e_5 modes involve either canting of the rings (200 cm^{-1}) or deformation of the individual Si_6 rings (295 cm^{-1}).

The intense 277 cm^{-1} perpendicular mode in $[MnSi_{12}]^+$ can be tracked through the 288 cm^{-1} mode in Mn_2Si_{12} and then to the 310 cm^{-1} mode in $[Mn_2Si_{13}]^+$, all of which are dominated by motion of the Mn atom in the *xy* plane. Similarly, the characteristic

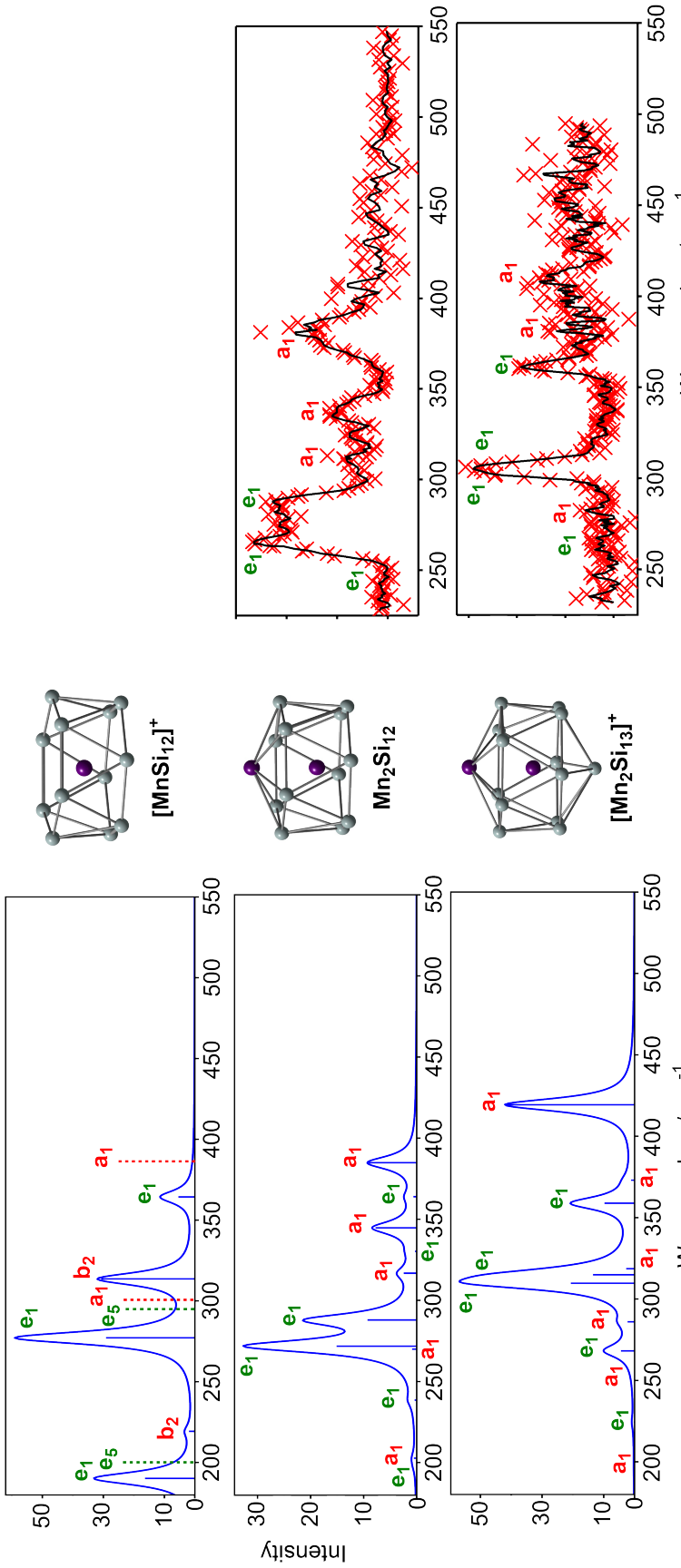


Figure 3.8: Evolution of the vibrational spectra of $[MnSi_{12}]^+$, Mn_2Si_{12} and $[Mn_2Si_{13}]^+$.

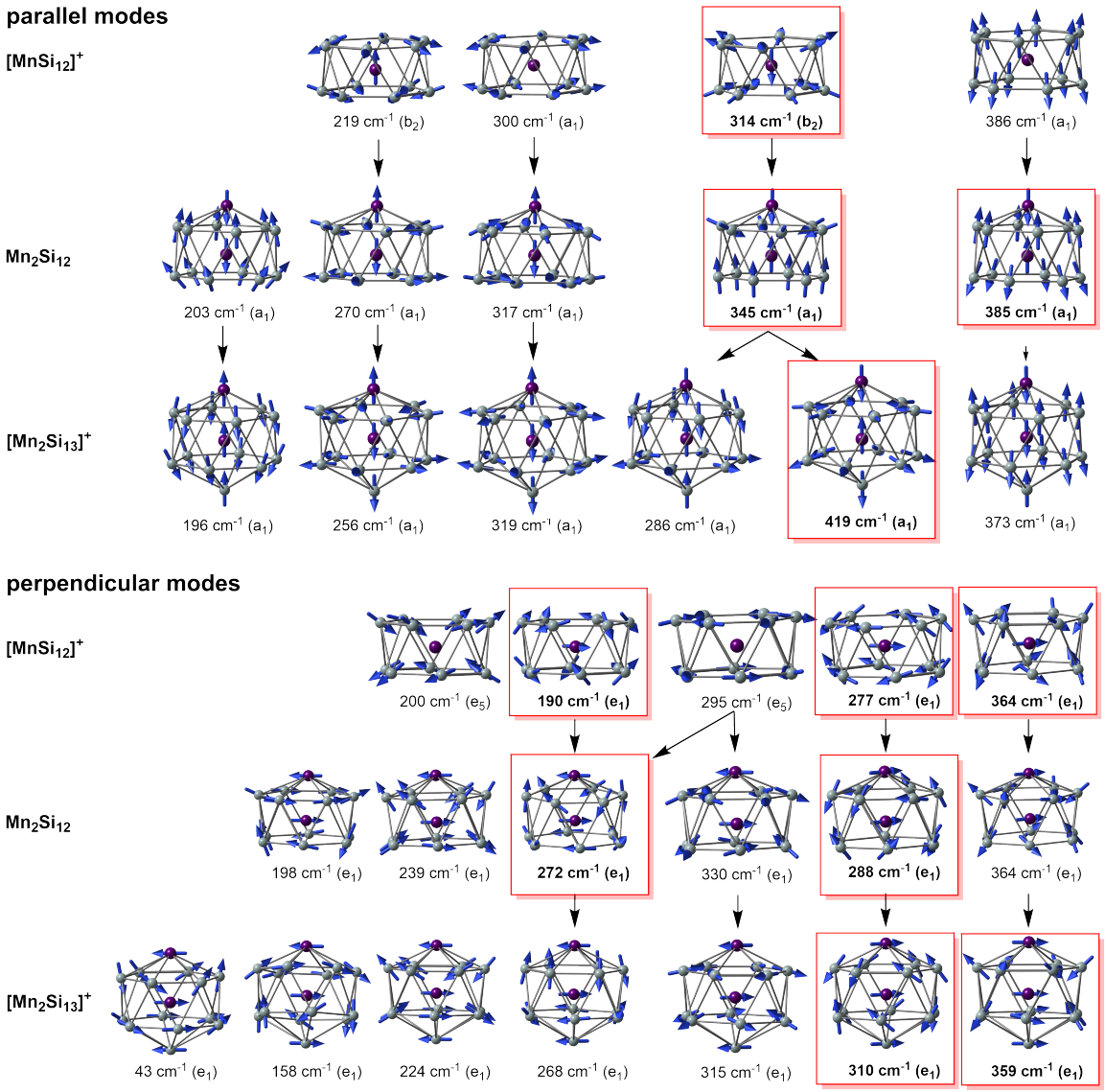


Figure 3.9: Evolution of the parallel and perpendicular vibrational modes in the series $[MnSi_{12}]^+$, Mn_2Si_{12} and $[Mn_2Si_{13}]^+$. Modes that feature prominently in the spectra are enclosed in red boxes.

canting of the rings in the 364 cm^{-1} mode in $[MnSi_{12}]^+$ is also found in the 364 cm^{-1} mode of Mn_2Si_{12} and also the 359 cm^{-1} mode of $[Mn_2Si_{13}]^+$. The most striking feature of the spectrum of Mn_2Si_{12} is the appearance of an additional e_1-symmetric mode with high intensity, at 272 cm^{-1}, which is responsible for the striking broadening in the experimental spectrum in the 250-300 cm^{-1} window. The displacements in this mode show that it is derived from a linear combination of the e_1 and e_5-symmetric modes of $[MnSi_{12}]^+$ at 190

and 295 cm^{-1}, respectively, both of which transform as e_1 in C_{6v} symmetry. The "e_5" character is apparent in the lower Si_6 ring while the "e_1" character is localised in the upper ring. The significant intensity of this mode (the most intense peak in the computed spectrum) is a direct consequence of the presence of the capping Mn atom: without it, the intensity drops to zero. We can follow the same displacements through to the 268 cm^{-1} mode of $[Mn_2Si_{13}]^+$, which has much lower intensity and is barely discernible above the baseline in the experiment. The reduction in intensity compared to Mn_2Si_{12} signals a return to a more symmetric, "*pseudo*-D_{6d}" environment for the cage, where both Si_6 faces are capped: the intensity would tend to zero in the limit that the Mn and Si caps were electronically identical.

A similar pattern of behaviour can be identified in the parallel modes. The intense b_2-symmetric peak at 314 cm^{-1} in $[MnSi_{12}]^+$ can be tracked into the 345 cm^{-1} mode of Mn_2Si_{12}, and from there to the antisymmetric Si-Mn-Mn stretch at 419 cm^{-1} in $[Mn_2Si_{13}]^+$. The corresponding symmetric stretch at 286 cm^{-1} is much less intense, but a small feature in this region just discernible above the baseline in the experimental spectrum. The second prominent band of a_1 symmetry in the spectrum of Mn_2Si_{12}, at 385 cm^{-1}, is closely related to the axial symmetric breathing of $[MnSi_{12}]^+$ at 386 cm^{-1} which was strictly forbidden in D_{6d} symmetry. This mode therefore owes its intensity entirely to the polar environment created by the capping Mn atom, and it vanishes again when the counter-balancing Si cap is introduced in $[Mn_2Si_{13}]^+$ (373 cm^{-1}). The forbidden a_1-symmetric equatorial breathing mode of $[MnSi_{12}]^+$ at 300 cm^{-1} also "lights up" in the presence of the capping Mn atom of Mn_2Si_{12}, in the 317 cm^{-1} mode that appears as a weak feature in the experimental spectrum. The corresponding 319 cm^{-1} mode in $[Mn_2Si_{13}]^+$ is reduced in intensity, again signalling a return to a *pseudo*-D_{6d} symmetric environment.

When considered against the reference point of the rigorously D_{6d}-symmetric $[MnSi_{12}]^+$ anti-prism, it becomes clear that we can understand the spectra of Mn_2Si_{12} and $[Mn_2Si_{13}]^+$

in terms of the extent to which the anti-prismatic $MnSi_{12}$ core deviates from the high-symmetry D_{6d} limit. The intense, allowed, bands involving motion of the endohedral Mn atom in the *xy* plane are apparent in both spectra (288 and 364 cm^{-1} in Mn_2Si_{12}, 310 and 359 cm^{-1} in $[Mn_2Si_{13}]^+$) while the parallel motion of the endohedral Mn atom in $[MnSi_{12}]^+$ (314 cm^{-1}) shifts into an Mn-Mn stretch at 345 cm^{-1} in Mn_2Si_{12} and an antisymmetric Si-Mn-Mn stretch at 419 cm^{-1} in $[Mn_2Si_{13}]^+$. The spectrum of Mn_2Si_{12} contains additional features because the polar environment allows bands that are formally forbidden in D_{6d} symmetry to acquire significant intensity. Thus, we see new features at 272 cm^{-1} (e_1), 317 and 385 cm^{-1} (both a_1) that can be traced to modes that are formally forbidden at the high-symmetry limit. All three of these extra bands are discernible in the experimental spectrum. The fact that these additional features disappear in the spectrum of $[Mn_2Si_{13}]^+$ reflects the rather similar electronic effects of the capping Mn and Si atoms, which restore approximate D_{6d} symmetry to the anti-prismatic $MnSi_{12}$ core. The more complex spectrum of Mn_2Si_{12} compared to that of $[Mn_2Si_{13}]^+$ is, therefore, a clear indication of the more polar, less symmetric, structure of the former.

3.3.2.4 Vibrational spectrum of Mn_2Si_{13}

The IR-MPD spectrum of Mn_2Si_{13} has a lower signal-to-noise ratio than those reported above, but nevertheless we can identify similar features, notably a region of high intensity in the 275-300 cm^{-1} region and another between 375 and 425 cm^{-1}. The very broad peaks are immediately indicative of a lower symmetry structure, and indeed, we find that while the lowest energy structure, ^{5}**13(a)**, has the same bi-capped hexagonal anti-prismatic structure as the corresponding cation, the capping Si atom has moved off the principal axis (Mn-Mn-Si = 159.5°) to give an approximately C_s-symmetric structure (Figure 3.10). The C_{6v}-symmetric structure (^{5}**13(b)** in Figure 3.10) has multiple imaginary frequencies which stem from an orbitally degenerate ground state. The reduction in symmetry splits all of the degenerate perpendicular vibrations into distinct a' and a'' components, and

also amplifies the difference between the upper and lower Si_6 hexagonal faces. The result is a return to a spectrum typical of Mn_2Si_{12}, where the modes involving motion of the endohedral Mn are complemented by additional features that would be forbidden in the anti-prism itself. The additional (and, as in Mn_2Si_{12}, more intense) bands are exemplified by the a'' mode at 315 cm^{-1}, the analogue of the 272 cm^{-1} mode in Mn_2Si_{12}, and the a' mode at 373 cm^{-1}, the analogue of the 385 cm^{-1} breathing mode in Mn_2Si_{12}. The 388 cm^{-1} mode contains a large contribution from the asymmetric Mn-Mn-Si stretch seen at 419 cm^{-1} in the cation, the lower frequency reflecting the displacement of the capping Si off the principal axis. The striking similarities between the spectra of Mn_2Si_{13} and Mn_2Si_{12} therefore reflect a common polar structure where the upper and lower hexagonal faces are sharply differentiated, compared to the rather simpler spectrum of $[Mn_2Si_{13}]^+$ where the anti-prism is more symmetrically capped.

3.3.2.5 Vibrational spectrum of Mn_2Si_{10}

Finally, for this chapter, we turn to the spectrum of Mn_2Si_{10}, which is strikingly different from all others in so much as the maximum intensity is found above 400 cm^{-1}. The structures of two low-lying isomers of Mn_2Si_{10}, $^3\mathbf{10}$ and $^7\mathbf{10}$, both with C_s symmetry, are compared in Figure 3.12. Whilst the lower symmetry makes it harder to classify the structures, it is clear that the connectivity of the Si vertices in $^3\mathbf{10}$ is high (4 or 5) and in that sense the structure resembles the hexagonal anti-prism of Mn_2Si_{12} (connectivity 4) rather more than the prism (connectivity 3). Conversely, the $^7\mathbf{10}$ isomer bears closer resemblance to the prisms in the sense that the Si vertices are 2, 3 or 4 connected, and indeed both the multiplicity (7) and the Mn-Mn bond length (2.75 Å) resemble those in the $^7\mathbf{12}$ structure of Mn_2Si_{12}. With the PBE functional the $^3\mathbf{10}$ isomer is the more stable of the two, with the $^7\mathbf{10}$ state 0.23 eV higher, but the situation is reversed for the hybrids, PBE0 and B3LYP, where the $^7\mathbf{10}$ isomer is the more stable by 0.25 eV and 0.42 eV, respectively (Figure 3.13). We see precisely the same systematic bias of the

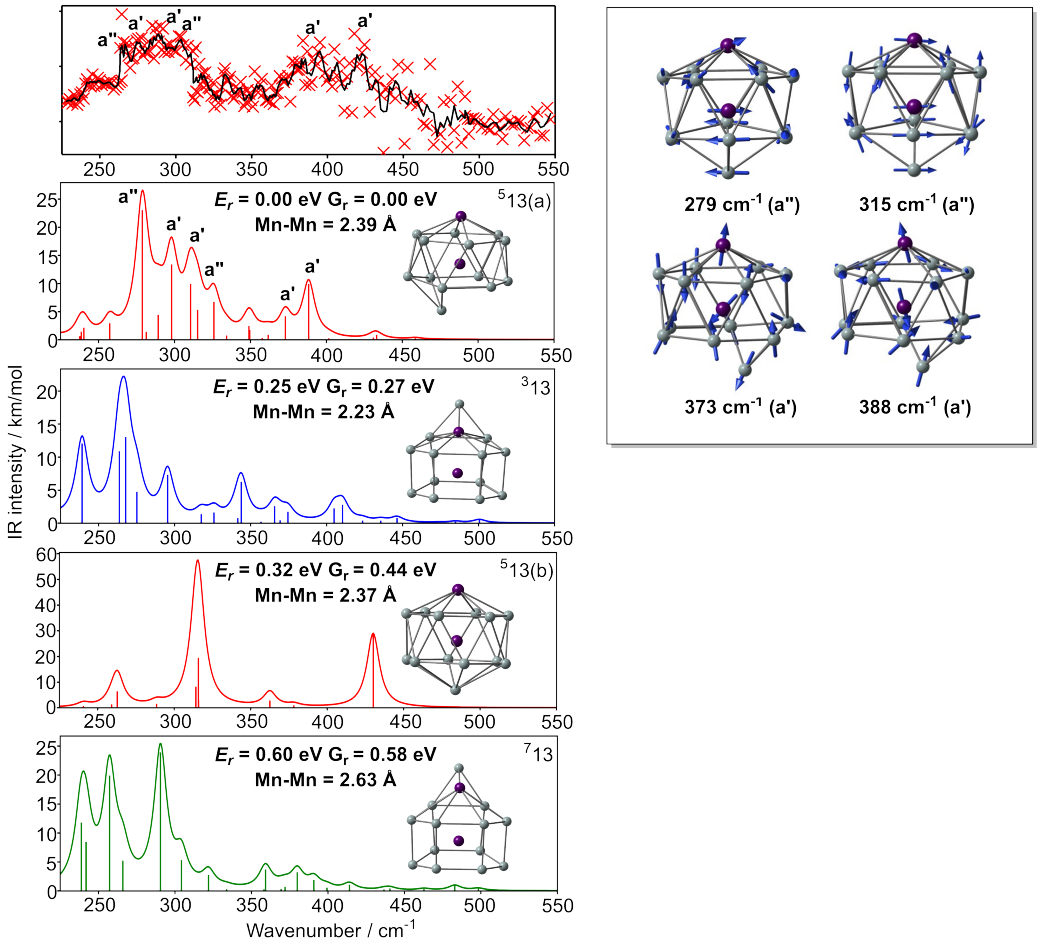


Figure 3.10: IR-MPD spectrum of Mn_2Si_{13}·Xe complex (intensity in arbitrary units), optimized structures and computed IR spectra of the low-lying isomers of Mn_2Si_{13} (PBE functional). Vibrational modes corresponding to intense peaks in the computed spectrum of ^{5}**13(a)** are also shown. Note that ^{5}**13(b)** is a second order saddle point, not a minimum.

LYP correlation functional towards low-connectivity structures that was identified for all other clusters considered here. Again, we conclude that the computed energies are highly functional dependent, and are therefore an unreliable metric upon which to base any assignment of the ground state.

The comparison between the measured IR-MPD spectrum and the DFT-computed fingerprints, also shown in Figure 3.12, indicates that the ^{3}**10** isomer provides a good match to the experiment, with three bands in the 425-475 cm^{-1} window, coincident with the broad absorption feature observed in this region. We also note here that the rather

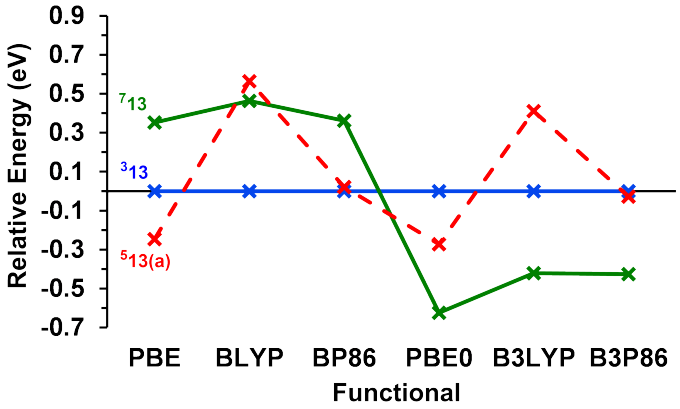


Figure 3.11: Variation of relative energies of different isomers of Mn_2Si_{13} with different functionals.

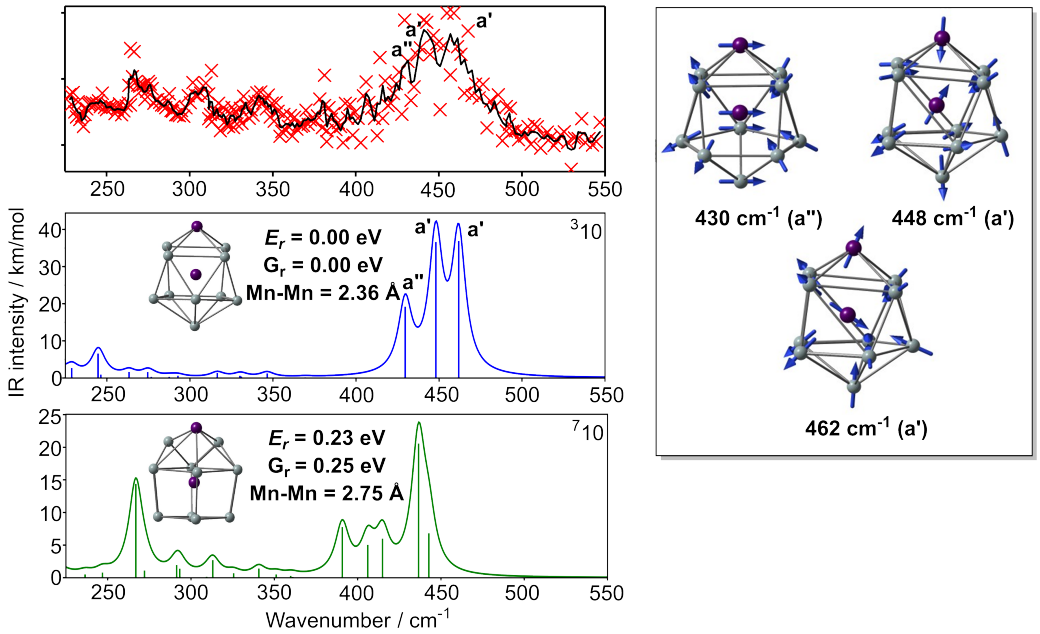


Figure 3.12: IR-MPD spectrum of Mn_2Si_{10}·Xe complex (intensity in arbitrary units), optimized structures and computed IR spectra of the low-lying isomers of Mn_2Si_{10}. Vibrational modes corresponding to intense peaks in the computed spectrum of ^{3}**10** are also shown. (PBE functional)

similar spectrum of $[Co_2Si_{10}]^+$ was previously assigned to a structure almost identical to ^{3}**10**, despite the fact that it was computed (using the hybrid B3P86 functional) to be less stable than the analogue of ^{7}**10**.[69] The absence of a 3-fold or higher rotational axis again splits the modes involving motion perpendicular to the principal axis into distinct *a′* and *a″* components, and also mixes the parallel and perpendicular modes in *a′* symmetry.

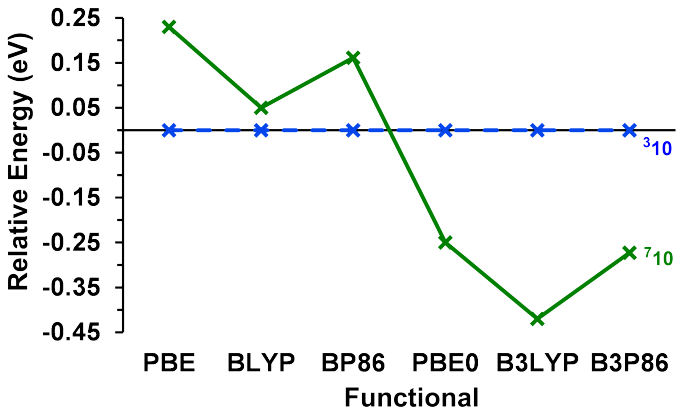


Figure 3.13: Variation of relative energies of different isomers of Mn_2Si_{10} with different functionals.

Nevertheless, we can identify the perpendicular motion of the Mn atom in the a'' mode at 430 cm^{-1}, while the other two intense features at 448 and 462 cm^{-1} have mixed parallel and perpendicular character. The major impact of the smaller cage (Si_{10} vs Si_{12}) is therefore to shift the perpendicular modes to higher frequencies by $\sim$150 cm^{-1} where they mix with the parallel modes that are found in a similar region in all of the spectra discussed previously.

3.4 Summary and Conclusions

In this chapter we have compared the IR-MPD spectra of a series of silicon clusters containing a Mn_2 unit, Mn_2Si_x, with $x = 10$, 12 and 13, and also the cation $[Mn_2Si_{13}]^+$ to the DFT-computed fingerprints of various candidate structures. We have been able to identify the isomers which offer the best match to experiment. In all cases, these are based on anti-prismatic architectures, which are identified consistently as the most stable only by the PBE functional. The B3LYP functional, in contrast, shows a systematic bias towards alternative structures with low-connectivity vertices (prisms rather than anti-prisms).

The ground-state structures of Mn_2Si_{12} and $[Mn_2Si_{13}]^+$ are both axially symmetric, which allows us to trace the evolution of the vibrational modes involving motion parallel (a_1) and perpendicular (e_1) to the principal axis. The isomeric D_{6d}-symmetric hexagonal

anti-prismatic $[MnSi_{12}]^+$ is a useful reference point in this regard because the high symmetry leads to a relatively simple vibrational spectrum. The major peaks in the spectrum of $[Mn_2Si_{13}]^+$ have very similar character (in terms of atomic displacements) to those in $[MnSi_{12}]^+$, reflecting the fact that the capping Mn and Si atoms on opposite hexagonal Si_6 faces exert a rather similar electronic influence on the anti-prism, giving a *pseudo*-D_{6d} environment. The vibrational spectrum of Mn_2Si_{12}, in contrast, shows a number of additional features that can be traced to modes that are forbidden in D_{6d} symmetry but acquire intensity in the polar C_{6v} environment imposed by the single capping Mn atom. In particular, the prominent peak around 380 cm^{-1} corresponds to the symmetric breathing mode of the Si_{12} cage, and is the clearest manifestation of the reduced symmetry. The neutral Mn_2Si_{13} cluster has a similar structure to the cation, except that the capping Si atom has moved off the principal axis. The resulting loss of axial symmetry splits the degenerate modes into two, and also amplifies the difference between the upper and lower Si_6 faces that led to a more complex spectrum in Mn_2Si_{12}. It is no coincidence, therefore, that the IR-MPD spectra of Mn_2Si_{12} and Mn_2Si_{13} are striking similar, both showing high-intensity features that correspond to vibrations that are forbidden in the parent anti-prism. Our analysis shows that these spectra are much more than mere fingerprints, and, when fully assigned, are rich in information about structure and also the interplay between Mn-Mn, Mn-Si and Si-Si bonding.

Chapter 4

Divergence from the unequivocal assignment of IR-MPD spectra

4.1 Introduction

In the previous chapter, we saw how Density Functional Theory can be successfully used to unravel the structures of some manganese doped silicon clusters. However, as the number of atoms in a cluster increase, it becomes increasingly difficult to assign structures using chemical intuition. Moreover, there are a number of limitations associated with the use of IR-MPD spectroscopy for structural elucidation. In the experiment, there is a possibility of forming clusters that are not necessarily in the ground state due to kinetic reasons which makes the unequivocal assignment of the spectrum to a single isomer difficult. Binding of the Xe tag can also be isomer discriminating: $[MnSi_7]^+$ does not bind to the Xe atom effectively due to electronic reasons [74]. Hence, the influence of the Xe tag on the geometry and spectrum of the cluster should also be considered.

In this chapter, we have considered cases where the unequivocal assignment of the IR-MPD spectrum to a single isomer is difficult. A different technique of generating initial structures of clusters has also been explored which is based on using an unbiased algorithm

instead of chemical intuition. The merits and demerits of both these techniques have been evaluated.

4.2 Methodology

4.2.1 Experimental Techniques

All spectroscopic measurements were conducted by Ewald Janssens, André Fielicke and co-workers as described in section 3.2.1.

4.2.2 Computational Techniques

All DFT calculations were performed using the Amsterdam Density Functional (ADF) package, version 2020.103.[25] Slater-type basis sets of triple-zeta and two polarization functions (TZ2P) were used on all atoms.[68] The number of fit functions were increased by adding the subkey 'FitType QZ4P' of the key BASIS and a fine grid was used for numerical integration (keyword 'BECKEGRID Quality good'). The Perdew-Becke-Ernzerhof (PBE)[19] functional was used in all calculations unless stated otherwise. All calculations were performed using spin-unrestricted DFT. For section 4.3.1, the initial structures were obtained in two ways: by carrying out literature surveys for reported structures of similar systems (doubly doped silicon clusters) or obtained by adding a second metal atom to previously outlined structures for singly doped silicon clusters. For section 4.3.3, the initial structures were obtained using a random structure generator (python script). The computed infrared spectra were generated with a Lorentzian line shape of 5 cm^{-1} full width at half maximum. The calculated frequency values were not scaled. Zip folders (Chapter4_Optimized_Coordinates and Chapter4_Mn2Si15__Random_Optimized_Coordinates) containing the Cartesian coordinates of all optimized structures can be found in the Oxford University Research Archive (https://doi.org/10.5287/bodleian:QRG2eZvxr).

4.3 Results and Discussion

4.3.1 Density Functional Theory

4.3.1.1 Ground-state structure and vibrational spectrum of $[Mn_2Si_{14}]^+$

The optimised structures of the low-lying isomers of $[Mn_2Si_{14}]^+$ are collected in Figure 4.1. The figure also includes their computed IR spectra with PBE functional. Based on the values of relative energies, there are four structures within 0.06 eV of each other. Hence, it is not reasonable to claim that any one of them is more significant than the others on energetic grounds. The relative energies of these isomers are yet again found to depend on the choice of the functional used (Figure 4.2). Both BLYP and B3LYP functionals tend to favour the fullerene-like derivative (^{4}**14$^+$(a)**) which again shows the bias of these functionals towards structures with low vertex connectivity. PBE0 predicts the ^{6}**14$^+$(b)** isomer to be the global minimum, again showing a preference for high spin multiplicity. The isomer ^{4}**14$^+$(a)** is derived from the fullerene-like isomer of W@Si_{14} reported by Hiura and co-workers. [75] It has 3-connected silicon vertices, an endohedral Mn atom and another Mn capping a pentagonal face. The computed IR spectrum of this isomer offers a poor match to the experiment; it is devoid of intense peaks above 280 cm^{-1}. The isomer ^{6}**14$^+$(a)**, with a short Mn-Mn distance of 2.51 Å, appears to be derived from the hexagonal anti-prismatic isomer of Mn_2Si_{12}, with the two extra silicon atoms capping a hexagonal face. The Gibbs free energy of this isomer is found to be lower than that of ^{4}**14$^+$(a)**. The relative energies of these two isomers only differ by 0.01 eV. For ^{6}**14$^+$(a)**, there are more lower frequency vibrations than ^{4}**14$^+$(a)** which might contribute to the entropy and yield a lower value for the Gibbs free energy. The computed spectrum of this isomer offers a fair match to the experiment up to 375 cm^{-1}. The feature centered at 290 cm^{-1} (encompassing several peaks) maps on to the experimental feature at 280 cm^{-1}. The peak at 343 cm^{-1} matches with the peak at around 340 cm^{-1} in the IR-MPD spectrum. Most of the vibrational features in the computed spectrum (shown in Figure

4.1 (a)) can be traced back to those of the ^{3}**12** state of Mn_2Si_{12}. Like the ^{3}**12** state, the upper and lower hexagonal faces are sharply differentiated in this isomer. The mode at 283 cm^{-1} involves the perpendicular motion of the endohedral Mn, just like the e_1 mode at 272 cm^{-1} in the ^{3}**12** state of Mn_2Si_{12}. The mode at 294 cm^{-1} is similar to the a_1 mode at 345 cm^{-1}, involving a Mn-Mn stretch and contraction of the Si_6 ring capped by the external Mn. The mode at 363 cm^{-1} involves breathing of the silicon cage, just like the a_1 mode at 385 cm^{-1}. The peak at 343 cm^{-1} corresponds to a slightly different mode, involving a Mn-Si stretch. The lack of symmetry in this isomer destroys the clean parallel/perpendicular separation, and we see a mixture of both in some vibrational modes. The remaining isomers (^{6}**14$^+$(b)** and ^{4}**14$^+$(b)**) are derivatives of the arachno structure reported by Kumar and co-workers [36] and contain an endohedral Mn in an arachno Si_{14} cage, with the external Mn capping a quadrangle face. Out of these two, the IR spectrum of ^{4}**14$^+$(b)**, which has a slightly longer Mn-Mn separation of 3.38 Å, offers a better match to the IR-MPD spectrum. In the computed spectrum, the peak at 282 cm^{-1} corresponds to the movement of the endohedral Mn perpendicular to the C_2 axis. The a_1 mode at 332 cm^{-1} corresponds to the movement of the endohedral Mn parallel to the C_2 axis. Another a_1 mode at 370 cm^{-1} is observed which corresponds to the stretching of the Si_{14} cage. Figure 4.1 (b) shows the key vibrational modes of this isomer. Unlike the smaller clusters, there is no single isomer whose computed spectrum offers a compelling match to the experiment across the whole spectral range. The computed spectra of ^{6}**14$^+$(a)** and ^{4}**14$^+$(b)** isomers offer a reasonable match to the experiment up to 375 cm^{-1}.

4.3.1.2 Ground-state structure and vibrational spectrum of $[Mn_2Si_{15}]^+$

Figure 4.3 shows three low-lying isomers of $[Mn_2Si_{15}]^+$. Like $[Mn_2Si_{14}]^+$, the relative energies of different isomers are too close to assign any single one as the global minimum with any confidence. The relative energies of the three isomers discussed here are dependent on the choice of functional used (Figure 4.4). The ^{6}**15$^+$(a)** isomer is found to be the global

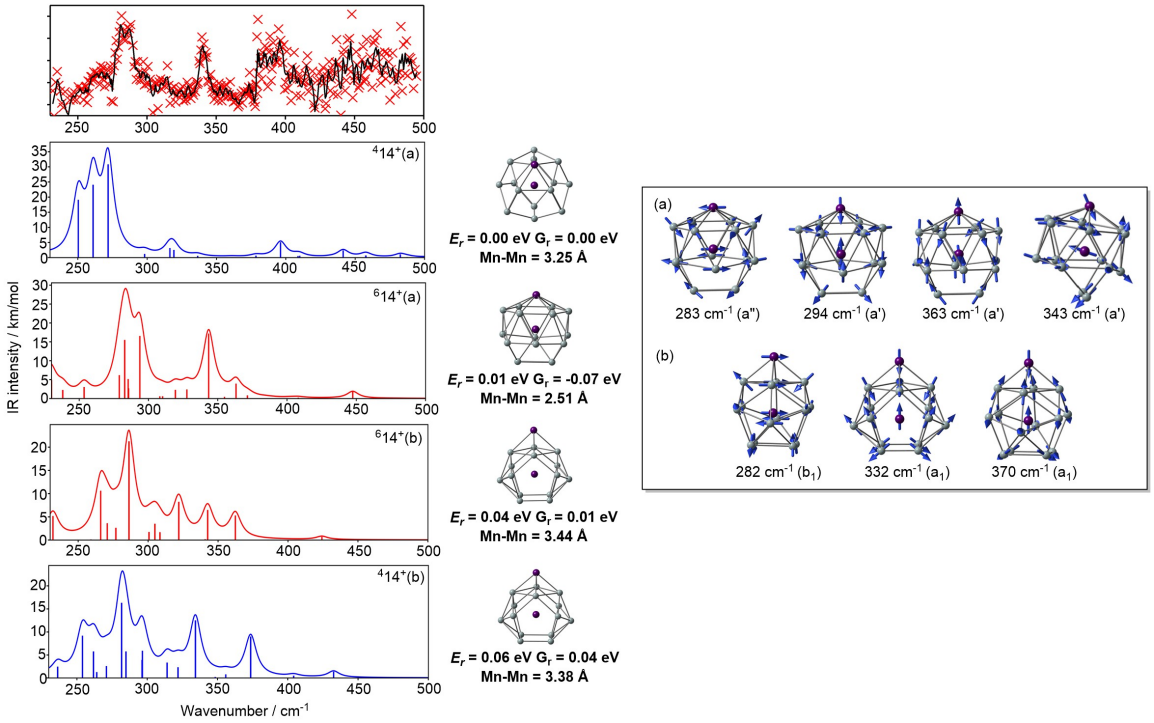


Figure 4.1: IR-MPD spectrum of $[Mn_2Si_{14}]^+$·Xe complex (intensity in arbitrary units), optimized structures and computed IR spectra of the low-lying isomers of $[Mn_2Si_{14}]^+$. Vibrational modes corresponding to intense peaks in the computed spectra of (a) ^{6}**14$^+$(a)** and (b) ^{4}**14$^+$(b)** are also shown. (PBE functional)

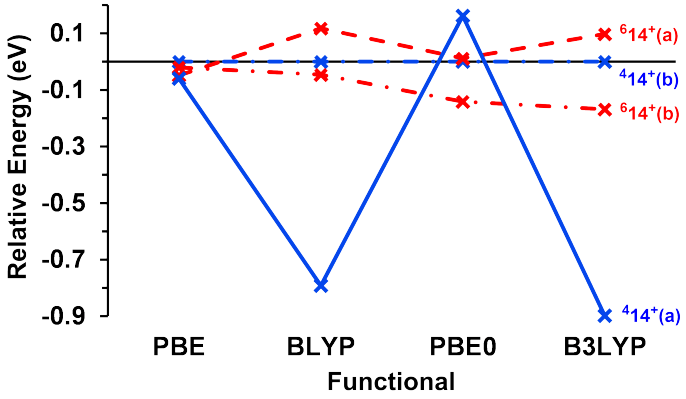


Figure 4.2: Variation of relative energies of different isomers of $[Mn_2Si_{14}]^+$ with different functionals.

minimum with all the functionals tried (PBE, BLYP, PBE0 and B3LYP). However, this isomer is stabilised significantly by BLYP and B3LYP which again reflects the bias of LYP functionals towards structures with low vertex connectivity. The isomer ^{6}**15$^+$(a)** bears similarities with the fullerene-like derivative ^{4}**14$^+$(a)** discussed in the previous section. It

exhibits slight distortions from the fullerene-like structure and has an additional Si atom capping a Si-Si edge. However, its computed IR spectrum does not seem to offer a good match to the experiment. The next isomer ^{6}**15$^+$(b)** is derived from the arachno structures (^{6}**14$^+$(b)** and ^{4}**14$^+$(b)**) discussed in the previous section, with an additional silicon atom capping a pentagonal face. The computed IR spectrum of this isomer matches well with the experiment only in the 240-320 cm^{-1} region. The lack of symmetry in this isomer yet again destroys the clean separation of vibrational modes. The peaks at 275 cm^{-1} and 297 cm^{-1} correspond to the movement of the endohedral Mn nearly perpendicular to what was the C_2 axis in the structures discussed previously (^{6}**14$^+$(b)** and ^{4}**14$^+$(b)**). The a' mode at 299 cm^{-1} corresponds to the nearly parallel movement of the endohedral Mn. These vibrational modes are shown in Figure 4.3 (a).

The third isomer ^{6}**15$^+$(c)**, with a relatively short Mn-Mn distance of 2.73 Å, is a derivative of the anti-prismatic isomer of Mn_2Si_{12}. It has three additional silicon atoms arranged in a triangle and capping the Si_6 ring of the anti-prism. Hence, the two hexagonal faces of the antiprism are yet again sharply differentiated. The computed spectrum of this isomer does not offer a great match to the IR-MPD spectrum across the entire spectral range, but we can see three peaks between 275 cm^{-1} and 325 cm^{-1} which are also seen in the experiment. In the computed spectrum, the peak at 283 cm^{-1} corresponds to the nearly perpendicular movement of the endohedral Mn (shown in Figure 4.3 (b)), similar to the e_1 mode at 288 cm^{-1} in the ^{3}**12** state of Mn_2Si_{12}. The mode at 309 cm^{-1} is similar to the a_1 mode at 345 cm^{-1} in Mn_2Si_{12}. However, it now involves a less prominent Mn-Mn stretch along with contraction of the Si_6 ring capped by the external Mn and expansion of the Si_3 triangle. Another peak is observed at 323 cm^{-1} which can be traced back to the e_1 mode at 364 cm^{-1} in Mn_2Si_{12} corresponding to the movement of the endohedral Mn perpendicular to the 6-fold rotation axis. The isomers ^{6}**15$^+$(b)** and ^{6}**15$^+$(c)** can be considered as viable candidates to account for the IR-MPD spectrum but there is no single isomer whose computed spectrum offers a good match to the IR-MPD spectrum across

the entire spectral range.

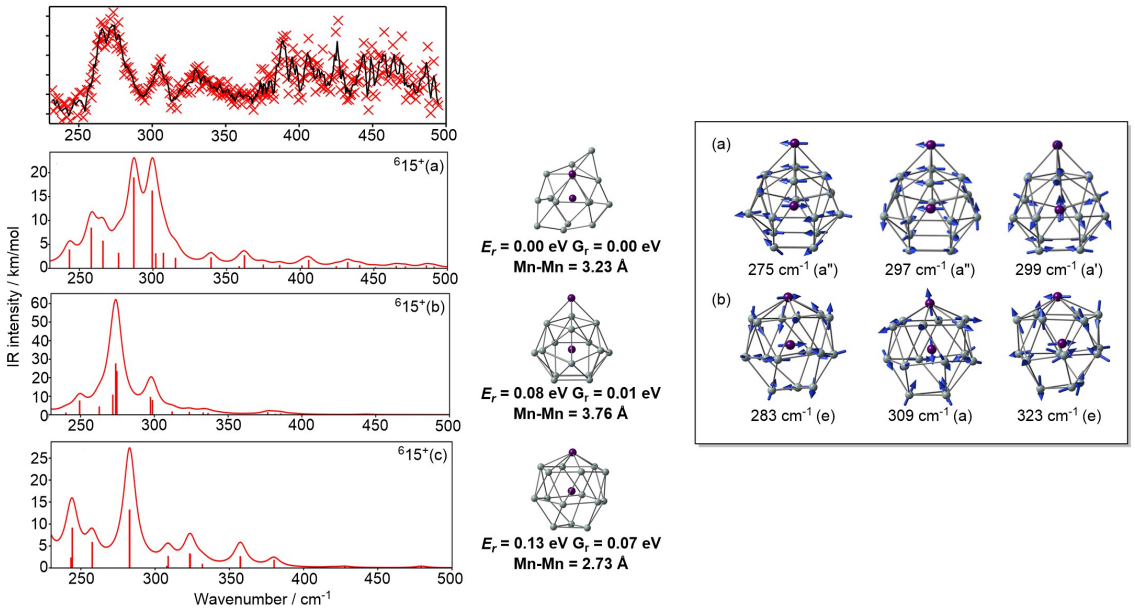


Figure 4.3: IR-MPD spectrum of $[Mn_2Si_{15}]^+$·Xe complex (intensity in arbitrary units), optimized structures and computed IR spectra of the low-lying isomers of $[Mn_2Si_{15}]^+$. Vibrational modes corresponding to intense peaks in the computed spectra of (a) $^6\mathbf{15}^+\mathbf{(b)}$ and (b) $^6\mathbf{15}^+\mathbf{(c)}$ are also shown. (PBE functional)

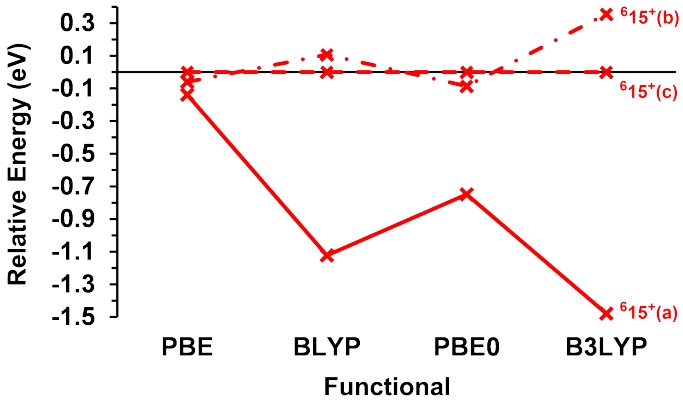


Figure 4.4: Variation of relative energies of different isomers of $[Mn_2Si_{15}]^+$ with different functionals.

4.3.1.3 Ground-state structure and vibrational spectrum of Mn_2Si_{11}

The low lying isomers of Mn_2Si_{11} are shown in Figure 4.5. Since all these isomers have little to no symmetry, it is not as straightforward to classify them as prism-like (low ver-

tex connectivity) or antiprism-like (high vertex connectivity) isomers, as was for Mn_2Si_{12}. Isomer ^{5}**11(c)** in Figure 4.5 closely resembles a prismatic cluster with 3-connected Si vertices. All other isomers have slight resemblance to antiprisms due to the higher connectivity of their Si vertices. As anticipated, the relative energies of these isomers are sensitive to the choice of the functional used (Figure 4.6). The ^{7}**11** isomer is found to be the global minimum with both hybrid functionals PBE0 and B3LYP which reinforces the fact that hybrid functionals tend to stabilize higher spin states. The two GGA functionals PBE and BLYP predict different structures, ^{5}**11(a)** isomer and the ^{5}**11(c)** isomer, to be the global minimum. Both BLYP and B3LYP functionals stabilise the ^{5}**11(c)** isomer to a great extent, again reflecting the bias of LYP functionals towards structures with low vertex connectivity. With no definitive answer regarding the identity of the ground state, the IR-MPD spectrum of Mn_2Si_{11} now plays a crucial role in deciding which isomer is observed experimentally. The spectrum appears to be similar to the one reported for $[Co_2Si_{11}]^+$. [69] For $[Co_2Si_{11}]^+$, the spectra of the prism like isomers in doublet and quartet spin states were reported to offer a fair match to the experiment. However, this is not the case for the corresponding Mn cluster. The calculated spectrum of ^{5}**11(c)** isomer of Mn_2Si_{11} has its most intense peak at 315 cm^{-1}. The IR-MPD spectrum has multiple peaks in this region but they are not as intense as the ones in the calculated spectrum of the ^{5}**11(c)** isomer. The spectrum of ^{5}**11(a)** isomer, which is the global minimum with PBE, offers a poor match to the experiment. The septet isomer (^{7}**11**), despite being the global minimum with both hybrid functionals, does not seem to be a viable candidate for the ground state structure. Its spectrum lacks highly intense peaks in the 250 to 300 cm^{-1} region. The Gibbs free energy of this isomer is found to be lower than that of ^{5}**11(c)**. The relative energies of these two isomers only differ by 0.01 eV. For ^{7}**11**, there are more lower frequency vibrations than ^{5}**11(c)** which might contribute to the entropy and yield a lower value for the Gibbs free energy. The spectrum of the ^{5}**11(b)** isomer, which lies 0.12 eV above the global minimum with PBE functional, offers a better match

to the IR-MPD spectrum, but lacks an intense peak at 425 cm^{-1} which is present in the measured spectrum. Hence, it could be an isomer that is observed experimentally, but the presence of other isomers cannot be disregarded. In the computed spectrum of the ^{5}**11(b)** isomer, the intense peak at 285 cm^{-1} corresponds to the movement of the inner Mn perpendicular to the Mn-Mn bond. The mode corresponding to the strong peak at 407 cm^{-1} is rather difficult to describe owing to the lack of symmetry in the cluster. It corresponds to a coupled stretching mode involving the endohedral Mn and the exohedral silicon atom.

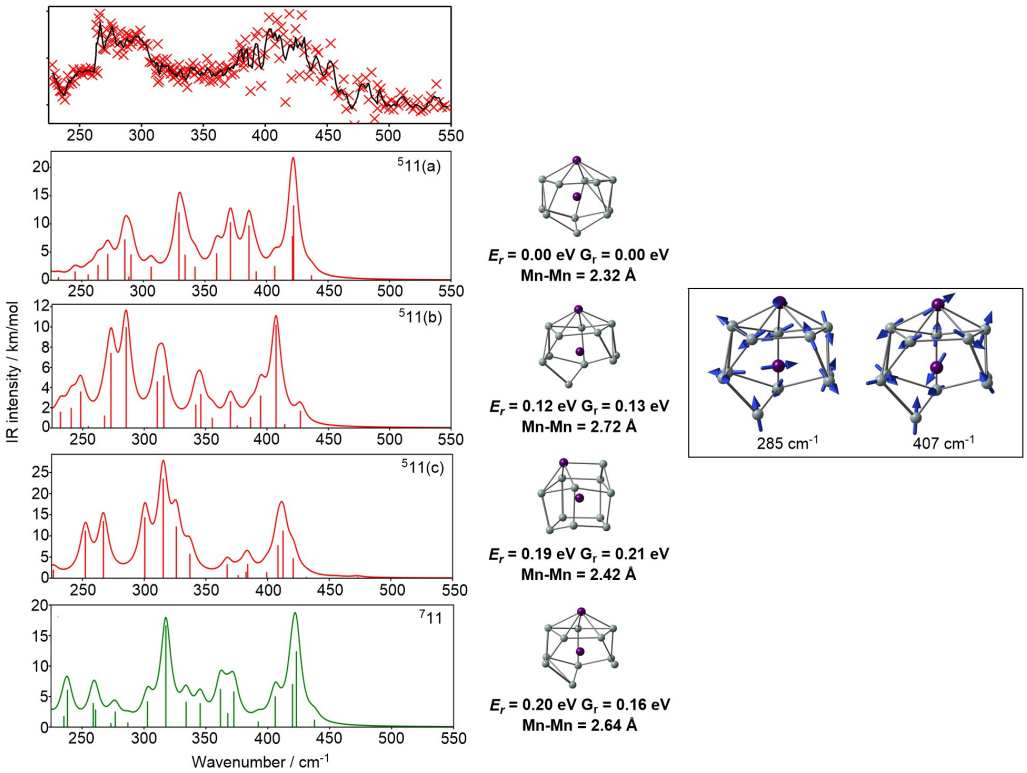


Figure 4.5: IR-MPD spectrum of Mn_2Si_{11}·Xe complex (intensity in arbitrary units), optimized structures and computed IR spectra of the low-lying isomers of Mn_2Si_{11}. Vibrational modes corresponding to intense peaks in the computed spectrum of ^{5}**11(b)** are also shown. (PBE functional)

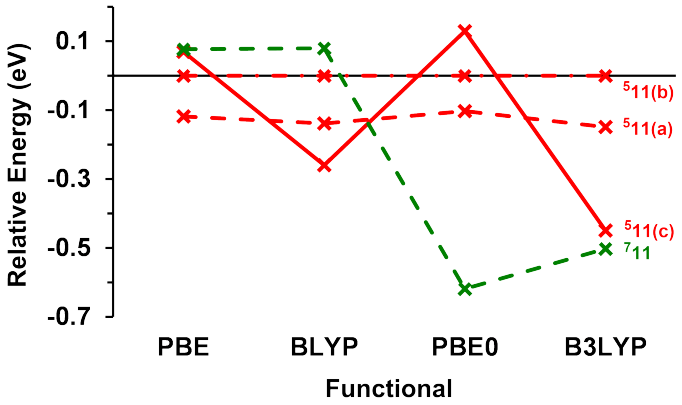
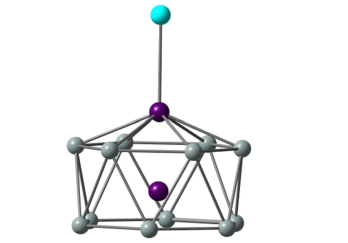


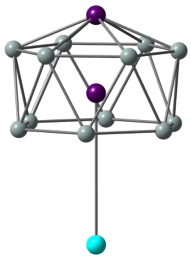
Figure 4.6: Variation of relative energies of different isomers of Mn_2Si_{11} with different functionals.

4.3.2 Effect of the Xe tag

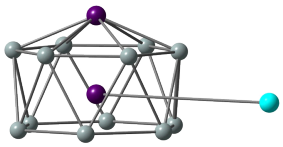
In all our DFT calculations, we have not taken into account the Xe tag that is an integral part of the experimental design. The interaction between the cluster and tag is, by design, weak, but it will nevertheless perturb the vibrations of the absorbing species to some extent. We have explored the triplet potential energy surface for the Mn_2Si_{12}·Xe complex using the same computational protocol but with the Grimme D4 corrections for dispersion to capture the van der Waals-like interactions involving Xe. We have identified three different minima (shown in Figure 4.7), the most stable of which involves the attachment of the Xe atom to the external Mn along the principal axis at a distance of 2.75 Å. The attachment of the Xe tag does not perturb the Mn-Mn interaction to any great extent: the Mn-Mn separation remains 2.23 Å and the spin densities are largely unchanged (Figure 4.8). The spectra of the clusters with and without tag are very similar (Figure 4.9), although the intensities of the parallel vibrational modes of Mn_2Si_{12} increase in the presence of the tag, due to the increase in dipole moment along the 6-fold rotation axis. This survey suggests, therefore, that the Xe tag does not have a significant influence on the geometry, electronic structure or vibrational spectrum of the cluster.



E_r = 0.00 eV Mn-Xe = 2.75 Å



E_r = 0.35 eV Mn-Xe = 4.35 Å



E_r = 0.50 eV Mn-Xe = 6.11 Å

Figure 4.7: Optimised structures of different isomers of the Mn_2Si_{12}·Xe complex (PBE functional).

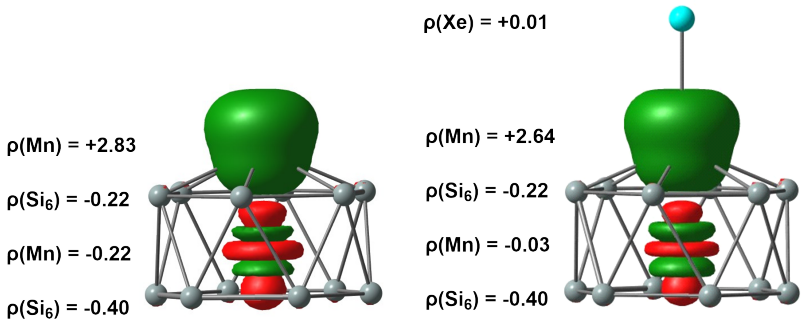


Figure 4.8: Comparison of the spin density plots and Mulliken projected spin densities of Mn_2Si_{12} and the Mn_2Si_{12}·Xe complex (PBE functional).

4.3.3 Choice of initial structures: Algorithms vs Chemical intuition

In the previous sections, we have used chemical intuition to obtain initial structures. The structures were obtained by carrying out literature surveys for reported structures of simi-

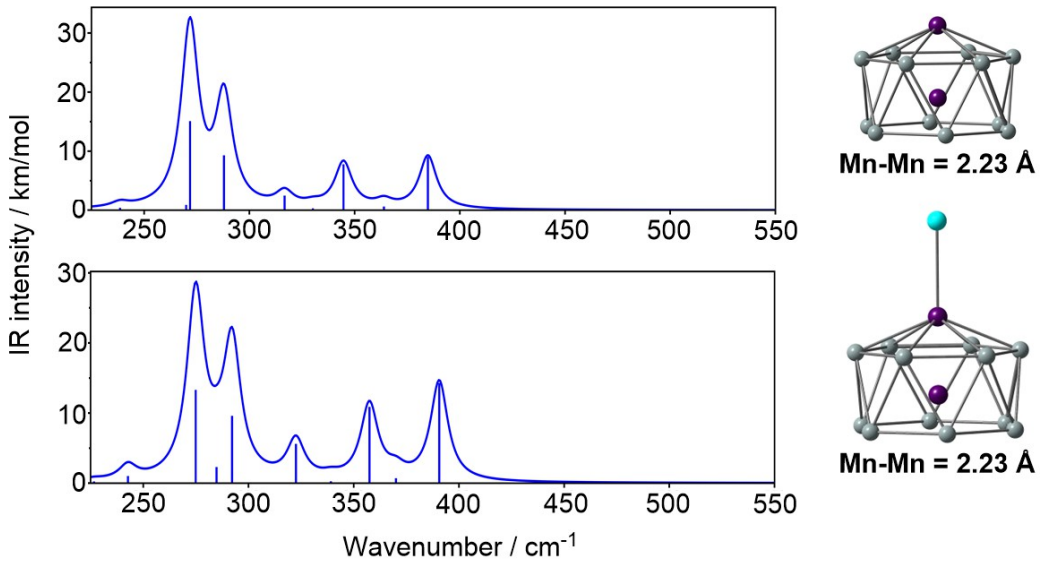


Figure 4.9: Comparison of the computed IR spectra of Mn_2Si_{12} and the Mn_2Si_{12}·Xe complex (PBE functional).

lar systems (doubly doped silicon clusters) or by adding a second metal atom to previously outlined structures for singly doped silicon clusters. Even though we have been successful in identifying the structures of some clusters, this technique still has its limitations. It is entirely possible to miss out isomers which could be more stable and whose computed spectra might offer a better match to the IR-MPD spectra, particularly for clusters containing a large number of atoms. As the size of the cluster increases, the possibility of different arrangements of atoms increases significantly. For both $[Mn_2Si_{14}]^+$ and $[Mn_2Si_{15}]^+$, we have not been able to identify a single isomer whose computed spectrum offers a match to the IR-MPD spectrum over the entire spectral range. We have been able to identify candidates which are close in energy and whose computed spectra match with the experiment over a given spectral range. There is a possibility of presence of multiple isomers in the experiment. Hence, we could account for the IR-MPD spectrum by considering the computed spectra of multiple low-lying isomers. However, in order to carry out an extensive survey of the potential energy surface, we have used a different strategy of generating initial structures.

A number of algorithms have been developed for finding the global minimum of clus-

ters. [76, 77, 78, 79] These algorithms often start by randomly generating initial structures for a cluster of a given composition. The structures are then optimised. New structures are then generated from previous ones. Different algorithms follow different ways of generating new structures. The CALYPSO method makes use of particle swarm optimization (PSO), which is inspired by the flocking and schooling behaviour of animals, to generate new structures. PSO is a stochastic global optimization algorithm based on self-improving structures using swarm intelligence. [76] The artificial bee colony (ABC) algorithm, which is based on the method by which bees find the best source of nectar, is employed by the ABCluster program. [78] This cycle is repeated till the lowest energy structures are found.

We have used a python script, which we will refer to as a random structure generator, to obtain initial structures. As the name suggests, this algorithm randomly generates structures for a given cluster. A truly random structure generator for clusters of composition Mn_2Si_x will produce a very large number of clusters that make little sense from a chemical perspective. In practical terms, this means that it will be extremely difficult to converge the initial SCF cycle. Given the size and complexity of the systems of interest, this would entail a very substantial commitment of computational resources. We have chosen to adopt a hybrid approach where constraints are placed on the initial arrangement of atoms, and additional filters are then applied to remove structures that are considered unrealistic. There is, of course, still a degree of user's bias/intuition here, but it was hoped that the hybrid approach would at least identify any low-lying isomers that resemble those shown in Figure 4.3 for $[Mn_2Si_{15}]^+$ (i.e. those with an endohedral Mn) that had been missed in the initial search.

The script, implemented as a Jupyter notebook, allows the user to select if endohedral structures are required. If this is the case, then the first atom is placed at the origin. The user is also supposed to enter the number of random configurations that they want to generate. Next, the number of atoms in the cluster have to specified. For restricting the separation between atoms, the user first has to specify the dimensions of a cubical

box that is centered at origin. Then, a range for the smallest distance between atoms is entered. In case of endohedral clusters, another range is specified for the distance between any given atom and the central atom. Finally, a list of all atoms is entered. Running the script then generates coordinates which satisfy the conditions imposed. These are also written into input files which are saved.

4.3.3.1 $[Mn_2Si_{15}]^+$

We have used the random structure generator to obtain initial structures for $[Mn_2Si_{15}]^+$. 300000 random structures have been generated. A cubical box with a height of 7.0 Å has been used and restrictions have been imposed on the smallest distance between atoms. Structures where the smallest distance was less than 2.0 Å or greater than 5.5 Å were rejected. Coordinates where atoms were closer than 1.0 Å to the endohedral atom were also rejected. For generating input files, we specified $+1$ as the charge, PBE as functional, DZP basis set, large core, 150 SCF iterations and 50 geometry steps. After applying these restrictions, only 5 to 10 structures were generated on each run, so in order to get several initial structures, the script was used multiple times. Alternatively, the number of randomly generated structures could have also been increased from 300000.

For each initial structure generated, three unrestricted DFT calculation were carried out with 3, 5 and 7 unpaired electrons. Due to restrictions on the number of calculations that could be done at a time, only a certain number of geometries could be optimised. Hence, the calculations were done in several batches. All in all, 123 initial optimisations were carried out. For a given batch, after optimisation with DZP basis set and a large core, the structures were examined and arranged on the basis of their bonding energies. The structures whose energies were within 1 eV of the most stable structure were further optimised with TZ2P basis set and no core. The infrared spectra were also computed for these isomers.

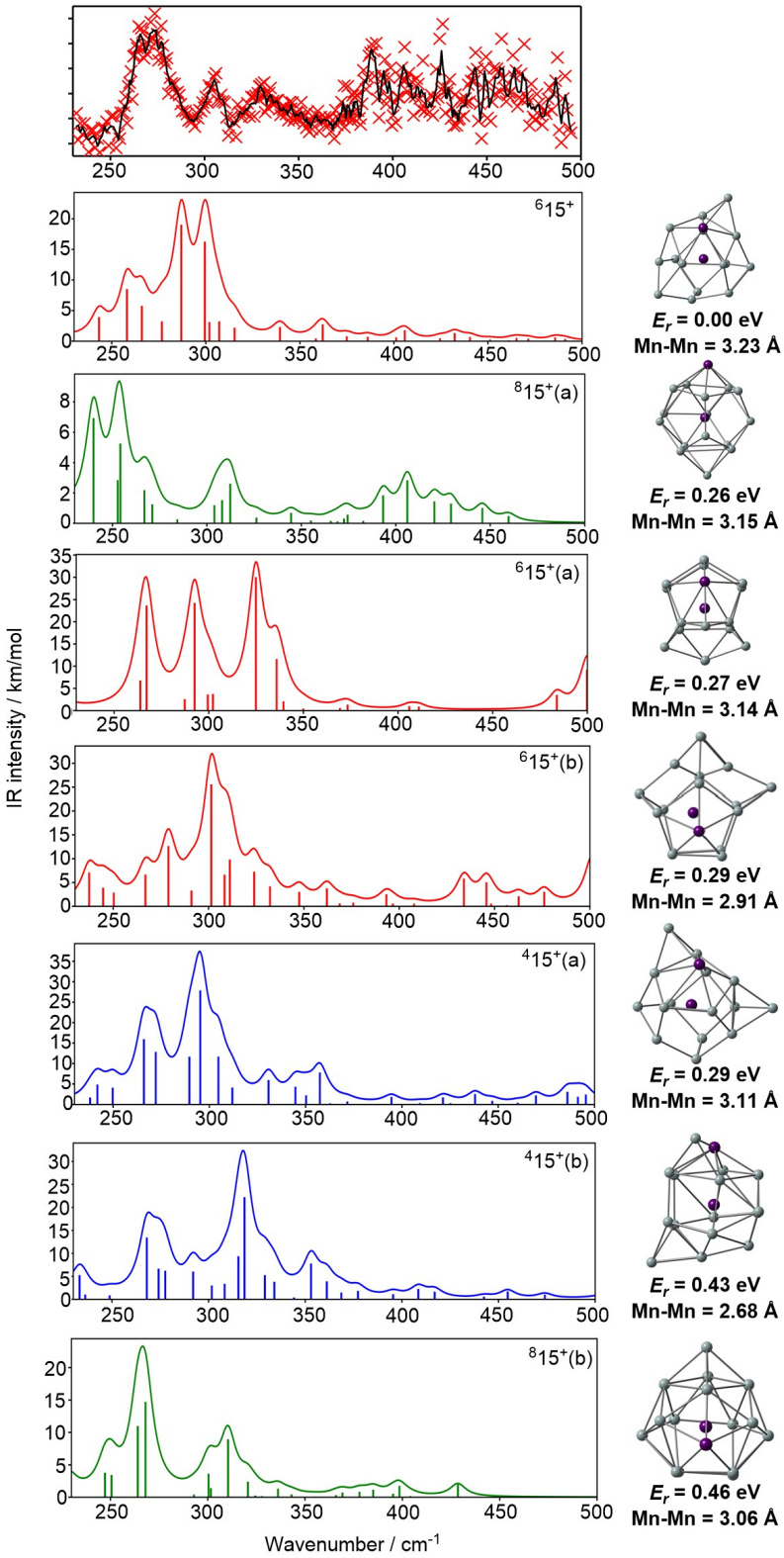


Figure 4.10: IR-MPD spectrum of $[Mn_2Si_{15}]^+$·Xe complex (intensity in arbitrary units), optimized structures and computed IR spectra of the low-lying isomers of $[Mn_2Si_{15}]^+$. Other than the most stable isomer, all other isomers were generated using the random structure generator. (PBE functional)

The optimized geometries of the low-lying states of $[Mn_2Si_{15}]^+$ are collected in Figure 4.10, along with their computed vibrational fingerprints. The most stable isomer in the figure ($^6\mathbf{15}^+$) is the one that was obtained by using chemical intuition for generating initial structures. It has been added to this figure to compare the energies of isomers generated by the random structure generator. We observe that this isomer is 0.26 eV more stable than the most stable isomer generated by the random structure generator ($^8\mathbf{15}^+\mathbf{(a)}$). We will now focus on the isomers that have been generated using the random structure generator. Due to lack of symmetry, it is difficult to classify these isomers as those similar to prisms (low vertex connectivity) or anti-prisms (high vertex connectivity). Yet again, we observe multiple isomers which are very close in energy. Hence, the IR-MPD spectrum plays a crucial role in deciding which isomers are observed in the experiment.

For the isomer $^8\mathbf{15}^+\mathbf{(a)}$, the computed spectrum shows peaks with high intensity centered around 250 cm^{-1}. There are a few peaks with less intensity around 310 cm^{-1} and between 390 cm^{-1} and 460 cm^{-1}. This computed spectrum does not offer a perfect match to the IR-MPD spectrum because despite having peaks at 310 cm^{-1} and between 390 cm^{-1} and 460 cm^{-1} which map on to peaks in the IR-MPD spectrum, the position of the most intense peak is different in both spectra. For the computed spectrum, this peak is centered at 250 cm^{-1} while in the IR-MPD spectrum, it is centered at 275 cm^{-1}. For the next isomer $^6\mathbf{15}^+\mathbf{(a)}$, the computed spectrum has intense peaks at 267 cm^{-1}, 292 cm^{-1} and 325 cm^{-1}. The position of these peaks roughly match with those seen in the experiment but the intensities of the last two peaks are much higher than those observed in the IR-MPD spectrum. Hence, the computed spectrum of this isomer does not match well with the IR-MPD spectrum. In the computed spectra of $^6\mathbf{15}^+\mathbf{(b)}$, $^4\mathbf{15}^+\mathbf{(a)}$ and $^4\mathbf{15}^+\mathbf{(b)}$ isomers, the position of the most intense peak does not match with the position of the corresponding peak in the IR-MPD spectrum (275 cm^{-1}). The computed spectrum of $^8\mathbf{15}^+\mathbf{(b)}$ isomer offers a reasonable match to the IR-MPD spectrum in the range 230 cm^{-1} to 325 cm^{-1} only.

Even after using the random structure generator, we have not been able to identify a single isomer whose computed spectrum matches with the IR-MPD spectrum over the entire spectral range. Moreover, the most stable isomer identified with this method is still 0.26 eV less stable than the one identified by chemical intuition, which creates a need for running more calculations with the random structure generator. Hence, such methods that employ algorithms to generate initial structures are computationally expensive and can involve optimisation of thousands of structures. Even after several optimisations, there is no guarantee of finding the global minimum.

4.4 Summary and Conclusions

In this chapter we have compared the IR-MPD spectra of three manganese doped silicon clusters ($[Mn_2Si_{14}]^+$, $[Mn_2Si_{15}]^+$ and Mn_2Si_{11}) with the DFT-computed spectra of different isomers. Unlike the previous chapter, we have not been able to assign the IR-MPD spectrum of each cluster to a single isomer. For the cationic cluster $[Mn_2Si_{14}]^+$, with PBE functional, we have identified multiple isomers which are very close in energy. However, the computed infrared spectra of none of these isomers match with the IR-MPD spectrum across the entire spectral range. The computed spectra of ^{6}**14$^+$(a)** and ^{4}**14$^+$(b)** isomers offer a good match to the experiment up to 375 cm^{-1}. The ^{6}**14$^+$(a)** isomer is a derivative of the hexagonal anti-prismatic Mn_2Si_{12} cluster with two additional silicon atoms capping a hexagonal face. However, the high D_{6d} symmetry of the anti-prismatic cage is lost. The case for $[Mn_2Si_{15}]^+$ is also not very different. With PBE functional, we have identified three isomers that are very close in energy. The IR-MPD spectrum cannot be accounted for by any one of these isomers alone. Two viable candidates (^{6}**15$^+$(b)** and ^{6}**15$^+$(c)**) have been identified whose computed spectra match well with the IR-MPD spectrum over a given spectral range. Out of these, the ^{6}**15$^+$(c)** isomer can again be considered as a derivative of the hexagonal anti-prismic Mn_2Si_{12} cluster. With three additional silicon

atoms arranged in the form of a triangle and capping a hexagonal face, there is a sharp differentiation between the two hexagonal faces. For Mn_2Si_{11}, no isomer has been identified that accounts for the IR-MPD spectrum over the entire spectral range. The ^{5}**11(b)** isomer has been identified as a viable candidate based on the reasonable match between its computed spectrum and the IR-MPD spectrum over a given spectral range. For all these clusters, we again see a bias of LYP functionals towards structures with low-vertex connectivity.

We have also explored how the geometry and IR spectrum of a cluster are nearly unperturbed despite of the presence of the Xe tag.

Since we were unable to assign the IR-MPD spectra of these clusters to single isomers, we switched to a different technique for obtaining initial structures. Instead of using chemical intuition, we used a python script to generate initial structures for $[Mn_2Si_{15}]^+$ randomly (subject to certain restraints). The structures generated by the script were optimized with a small basis set and a large core. The low-lying isomers obtained by the crude optimisation were then re-optimised with a larger basis set and no core. For these isomers, the infrared spectra were also computed. However, despite using this unbiased algorithm, we have still not been able to identify a single isomer for $[Mn_2Si_{15}]^+$ whose computed spectrum matches with the experiment over the entire spectral range. We can find limitations of both approaches. Deducing structures by chemical intuition can become challenging as the size of the cluster increases. Moreover, it is always possible to miss out certain isomers using this technique. Unbiased algorithms offer a different approach of exploring the potential energy surface. Considering the random structure generator used here, we can see that finding the global minimum can require hundreds of optimisations. Even after running several batches of calculations, there is no assurance of finding the global minimum. A combination of both these techniques can be considered, specially for larger clusters.

A number of limitations also stem from the use of IR-MPD spectroscopy for deducing

structures of clusters. As observed for $[Mn_2Si_{14}]^+$ and $[Mn_2Si_{15}]^+$, it can be extremely difficult to choose between isomers with similar vibrational spectra. Moreover, a poor signal-to-noise ratio also adds to the uncertainties in identifying peaks.

Chapter 5

Beyond DFT: the use of wavefunction-based methods

5.1 Introduction

In the last two chapters, Density Functional Theory (DFT) has been employed to investigate the electronic structure and geometries of manganese doped silicon clusters. The dependence of conclusions from DFT calculations on the choice of exchange-correlation functional used has been highlighted. This dependence poses a problem because different people use different criteria for selecting a functional. While a researcher's choice of functional is usually based on success in previous studies, choosing functionals that reproduce some experimentally measured entity is also common. As a result, we see several functionals being used to address the same research question. As far as the study of doped silicon clusters is concerned, we have noted how hybrid functionals stabilise high spin-states and LYP functionals favour prism-like clusters. On the other hand, PBE and PBE0 functionals tend to favour deltahedral structures.

In this chapter, we have employed a wavefunction based technique - Multiconfigurational Self-Consistent Field (MC-SCF) theory. It offers a more robust way of dealing

with correlation, where we can identify specific pairs of electrons that are correlated. This technique has been used for silicon clusters containing one transition metal atom [37, 44, 15, 38]. However, most of these studies employ the Complete Active Space Self-Consistent Field (CASSCF) method. For clusters containing two metal atoms, the size of the active space increases beyond the limit that can be tackled by this method. Hence, to restrict the dimension of the CI expansion, we have used the Generalized Active Space (GAS) and Restricted Active Space (RAS) methodologies in this chapter.

5.2 Methodology

5.2.1 Computational Techniques

GASSCF, RASSCF, RASPT2 and CASPT2 calculations were performed using the Open-Molcas code, [80, 81] pymolcas version py2.02, with an all-electron atomic natural orbital basis set (ANO-S-VDZ).[82] All calculations were done using the optimized geometries obtained from DFT calculations.

5.3 Results and Discussion

5.3.1 GASSCF Calculations of Mn_2Si_{12}

Having identified the triplet state of the hexagonal anti-prismatic structure (^{3}**12**) as the most likely candidate to account for the experimental data of Mn_2Si_{12}, we now turn to MC-SCF theory for an alternative perspective on Mn-Mn and Mn-Si bonding. In the unrestricted Kohn-Sham (UKS) calculations described in section 3.3.2.1, the converged solution proves to be spin contaminated, with $\langle S^2 \rangle = 2.53$ and Mulliken spin densities of +2.83, -0.22 and -0.61 on Mn(external), Mn(endohedral) and Si_{12} units, respectively. These are usually indicators of multiconfigurational character, and indeed CASSCF

methodology has been used to highlight the extensive "in-out" correlation between the electrons in the Mn-Si bonds of $[MnSi_{12}]^+$, where spin contamination is also significant in the UKS wavefunction. [15] The potential presence of Mn-Mn bonding in Mn_2Si_{12} adds a further dimension to the problem, offering the possibility of "left-right" correlation between electrons on the two Mn centers in addition to the "in-out" correlation in the Mn-Si bonds. It also increases the dimensions of the problem beyond the limits that can be tackled with a conventional active space, so in order to restrict the dimensions of the CI expansion, we use the Generalized Active Space (GAS) methodology wherein the active space is partitioned into smaller sub-groups. [83, 84, 85] In the case of the ^{3}**12** ground state of Mn_2Si_{12}, we have identified a GAS5(16,16) active space with five partitions (GASa-e) containing orbitals of local σ (a), π (b,c) and δ (d,e) symmetry, respectively. No excitations between different partitions were allowed in the CI expansion. The natural orbitals and occupation numbers are collected in Figure 5.1 (a). The occupation numbers of 1.53 and 0.47 for the two orbitals in the σ partition (GASa) are an immediate indication of the "left-right" correlation typical of a moderately strong σ bond, and the effective σ bond order (EBO) of 0.53 ((1.53 - 0.47) / 2) is substantially reduced below the formal value of 1.0. The π partition (GASb and c) contains six orbitals, including both Mn-Mn π bonding and antibonding orbitals. The antibonding pair is singly occupied and strongly localised on the external Mn center. The remaining four orbitals are Mn-Si bonding/antibonding pairs localized on the endohedral Mn and the Si_{12} cluster, and are very similar to the corresponding orbitals identified for $[MnSi_{12}]^+$. [15] Finally, GASd and e partitions contain eight orbitals of Mn-Mn δ symmetry, including Mn-Si bonding/antibonding pairs on both the endohedral and external Mn centers. Strong "in-out" correlation is again apparent in the occupation numbers of 1.72 and 0.29.

The orbitals in the Generalized Active Space discussed above map on to the Kohn-Sham orbitals. The two unpaired electrons reside in Mn-Mn π antibonding orbitals with both DFT and GASSCF calculations. The Mn-Mn σ and π bonding orbitals are fully

occupied in the unrestricted Kohn-Sham ansatz. These orbitals are also present in the Generalized Active Space with large occupation numbers (1.53 for σ and 1.86 for Mn-Mn π and Mn-Si bonding molecular orbitals). The σ antibonding orbital which is vacant in the UKS framework has a smaller occupation number in the GASSCF calculation (0.47).

Table 5.1 shows the configurations with the highest contribution to the GASSCF wavefunction. For Mn_2Si_{12}, the leading configuration has doubly occupied bonding orbitals while the corresponding anti-bonding orbitals are vacant. Despite being the leading configuration, it only has a 38% contribution to the wavefunction. This is an indication of significant mutliconfigurational character. One minor contributor with a weight of 6% is also shown which involves double excitation of electrons from the Mn-Mn σ bonding orbital to the corresponding σ^* anti-bonding orbital. There are multiple contributing configurations with weights less than 5%.

The GAS wavefunction is therefore qualitatively consistent with the UKS version, in so much as it predicts both σ and π contributions to the Mn-Mn bond, along with significant multiconfigurational character in the Mn-Si bonds, particularly those involving the endohedral Mn center.

5.3.2 GASSCF Calculations of $[Mn_2Si_{13}]^+$

In section 3.3.2.2, $^4\mathbf{13}^+\mathbf{(a)}$ was identified as the isomer to account for the IR-MPD spectrum of $[Mn_2Si_{13}]^+$ using DFT calculations. We have carried out GASSCF calculations for this isomer. Since both $^3\mathbf{12}$ state of Mn_2Si_{12} and the $^4\mathbf{13}^+\mathbf{(a)}$ isomer share a hexagonal anti-prismatic core, we can expect them to have similar Generalized Active Spaces. Like the GAS for Mn_2Si_{12}, we have identified a GAS5(17,17) active space with five partitions (GASa-e) containing orbitals of local σ (a), π (b,c) and δ (d,e) symmetry, respectively. The natural orbitals and occupation numbers are collected in Figure 5.1 (b). The orbitals with local π and δ symmetry and their occupation numbers are very similar to those reported for Mn_2Si_{12}. Again, strong "in-out" correlation is apparent in the occupation

numbers of 1.60 and 0.41. The major difference is in the subspace containing orbitals of local σ symmetry (a). Since this isomer has a quartet spin state, it possesses three unpaired electrons two of which reside in the same Mn-Mn π antibonding orbitals, as was the case for the ^{3}**12** state of Mn_2Si_{12}. However, the third unpaired electron is present in the σ antibonding orbital, which is in agreement with the frontier Kohn-Sham orbitals of ^{4}**13$^+$(a)** isomer shown in Figure 3.5 (b). If we now consider a subspace with just the Mn-Mn σ bonding and antibonding orbitals, then we would have three electrons in two orbitals. If it is a 3-electron-2-orbital GAS, there is no 2-electron excitation possible, so there is, in effect, no correlation. Therefore to "fix" the doubly occupied orbital in the active space, we need to introduce a third orbital which does offer a double excitation.

The configurations with the highest contribution to the wavefunction are shown in Table 5.1. Apart from the σ subspace, the leading configuration is similar to the leading configuration for Mn_2Si_{12}. It has occupied bonding orbitals and vacant anti-bonding orbitals. This configuration only contributes 40% to the wavefunction, again indicating significant multiconfigurational character. Two minor contributors are also shown in the table which involve one-electron excitations in the δ subspaces.

5.3.3 GASSCF Calculations of Mn_2Si_{10}

In section 3.3.2.5, we identified ^{3}**10** as the isomer that accounts for the IR-MPD spectrum of Mn_2Si_{10}. Just like Mn_2Si_{12}, the UKS solution for the ^{3}**10** isomer is spin contaminated ($\langle S^2 \rangle = 2.95$ and Mulliken spin densities of +3.00 and -0.58 on Mn(external) and Mn(endohedral)) which again is an indication of multiconfigurational character. In the case of the ^{3}**10** ground state of Mn_2Si_{10}, we have identified a GAS3(16,16) active space with three partitions (GASa-c) containing orbitals of local σ (a) , δ (b) and π (c) symmetry, respectively. The natural orbitals and occupation numbers are collected in Figure 5.2. The occupation numbers of 1.52 and 0.48 for the two orbitals in the σ partition (GASa) again indicate strong "left-right" correlation typical of a moderately strong σ bond (EBO

of 0.52). The π partition (GASc) again contains six orbitals, including both Mn-Mn π bonding and antibonding orbitals. The antibonding pair is singly occupied and yet again strongly localised on the external Mn center. The remaining four orbitals are very similar to the corresponding orbitals identified for Mn_2Si_{12}. Finally, the GASb partition contains eight orbitals of Mn-Mn δ symmetry, including Mn-Si bonding/antibonding pairs on both the endohedral and external Mn centers. Strong "in-out" correlation is again apparent in the occupation numbers of 1.41 and 0.60. The GAS wavefunction is again qualitatively consistent with the UKS version.

Table 5.1 shows the configurations with the highest contribution to the wavefunction of Mn_2Si_{10}. The leading configuration, with a weight of 30%, has doubly occupied bonding orbitals and vacant anti-bonding orbitals. The minor contributors shown in the table involve two and one-electron excitations in the δ subspace. The weights of these configurations indicate significant mutliconfigurational character.

For all three clusters considered in this chapter, the leading configurations have similar weights. Active orbitals with local π and δ symmetry have similar shapes, occupation numbers and share common features with the corresponding Kohn-Sham orbitals. The σ orbitals also have similar occupation numbers for Mn_2Si_{12} and Mn_2Si_{10} clusters. The similarities in the active spaces of these clusters could be a characteristic feature of silicon clusters containing a transition metal dimer where one transition metal atom lies inside the silicon cage and the other lies outside.

5.3.4 RASSCF/RASPT2 Calculations of $[Mn_2Si_{13}]^+$

Despite of the advantages that the GASSCF method offers, it has one major limitation. Currently, perturbation theory corrections cannot be applied to the energies obtained by this method. Hence, we cannot account for dynamic correlation. As discussed in section 2.1.4.2, RASSCF method also offers the advantage of limited number of configurations. Moreover, second order perturbation theory corrections can be applied to the energies

Cluster	Configuration			Weight (%)
	σ	π	δ	
Mn_2Si_{12}	$a_1^2a_1^0$	$b_1^2b_1^0b_1^1\ b_2^2b_2^0b_2^1$	$a_1^2a_1^0a_1^2a_1^0\ a_2^2a_2^0a_2^2a_2^0$	38
	$a_1^0a_1^2$	$b_1^2b_1^0b_1^1\ b_2^2b_2^0b_2^1$	$a_1^2a_1^0a_1^2a_1^0\ a_2^2a_2^0a_2^2a_2^0$	6
$[Mn_2Si_{13}]^+$	$a_1^2a_1^0a_1^1$	$b_1^2b_1^0b_1^1\ b_2^2b_2^0b_2^1$	$a_1^2a_1^0a_1^2a_1^0\ a_2^2a_2^0a_2^2a_2^0$	40
	$a_1^2a_1^0a_1^1$	$b_1^2b_1^0b_1^1\ b_2^2b_2^0b_2^1$	$a_1^2a_1^0a_1^1a_1^1\ a_2^2a_2^0a_2^2a_2^0$	5
	$a_1^2a_1^0a_1^1$	$b_1^2b_1^0b_1^1\ b_2^2b_2^0b_2^1$	$a_1^2a_1^0a_1^2a_1^0\ a_2^2a_2^0a_2^1a_2^1$	5
Mn_2Si_{10}	$a'^2a'^0$	$a''^2a''^0a'^2a'^0a''^1a'^1$	$a'^2a'^0a''^2a''^0a'^2a'^0a''^2a''^0$	30
	$a'^2a'^0$	$a''^2a''^0a'^2a'^0a''^1a'^1$	$a'^2a'^0a''^2a''^0a'^0a'^2a''^2a''^0$	6
	$a'^2a'^0$	$a''^2a''^0a'^2a'^0a''^1a'^1$	$a'^2a'^0a''^2a''^0a'^1a'^1a''^2a''^0$	6

Table 5.1: Leading configurations in the GASSCF wavefunctions of the ground states of Mn_2Si_{12}, $[Mn_2Si_{13}]^+$ and Mn_2Si_{10}.

obtained by this method (RASPT2).

It is challenging to get the same static correlation in a manageable RAS as we have in a (17,17) GAS for $[Mn_2Si_{13}]^+$. We have tried to achieve this for $[Mn_2Si_{13}]^+$ using the GAS calculation as a reference (Figure 5.1(b)). We placed the three singly occupied orbitals and the δ orbitals on the outer Mn into RAS2. All other nearly doubly occupied orbitals were placed in RAS1 and all nearly empty orbitals in RAS3. We then allowed up to two excitations from RAS1 and up to two electrons into RAS3. The natural orbitals and occupation numbers for this restricted active space are collected in Figure 5.3

All the important correlations on the outer Mn have been captured in this restricted active space. However, the RASSCF energy (-6054.7712 Eh) is slightly higher than the energy obtained from the GASSCF calculation (-6054.8647 Eh). This is because we are missing quadruple excitations on the inner Mn in the RASSCF calculation (for example $\pi_x^2\pi_x^{*0} \rightarrow \pi_x^0\pi_x^{*2}$ and $\pi_y^2\pi_y^{*0} \rightarrow \pi_y^0\pi_y^{*2}$ simultaneously). These quadruples are somewhat important as they are correlating electrons on the same Mn atoms, so are coupled (and they make a very significant contribution in the delta orbitals on the outer Mn, but these are included because those orbitals are in RAS2). On applying the perturbation theory correction to the RASSCF calculation described above, we obtained an energy of -6056.3297 Eh. We might expect the perturbation theory correction to also account for

the missing static correlation in the restricted active space calculation.

In order to check whether the perturbation theory correction accounts for the missing static correlation, we carried out another RASPT2 calculation. We decided to keep only the singly occupied orbitals in RAS2, and moved the other orbitals to RAS1 or RAS3. The natural orbitals and occupation numbers for this restricted active space are collected in Figure 5.4. On applying perturbation theory corrections, we obtained an energy of -6056.2854 Eh which is higher than the one obtained with the previous restricted active space (-6056.3297 Eh). The higher energy value might indicate that perturbation theory correction cannot account for the missing static correlation. On removing important excitations from the CI expansion, the energy from the RASSCF calculation increased. Perturbation theory corrections could not recover the lost static correlation completely leading to a higher RASPT2 energy. However, we should remember that perturbation theory corrections are not variational. Hence, we should not draw conclusions based on merely the perturbation theory corrected energy values.

5.3.5 CASPT2 Calculations of $[Mn_2Si_{13}]^+$

In order to further understand the effect of applying perturbation theory corrections, we have carried out CASPT2 calculations for $[Mn_2Si_{13}]^+$. We have used a (7,7) active space for this calculation. In order to compare our results with the RASPT2 calculations, we have added those orbitals to the active space which were present in RAS2 in the first RASSCF calculation. These include the three singly occupied orbitals and δ orbitals on the outer Mn. The natural orbitals and occupation numbers for this active space are collected in Figure 5.5.

On applying perturbation theory corrections to this CASSCF calculation, we obtained an energy of -6056.4953 Eh which is lower than the one obtained by the RASPT2 calculation (-6056.3297 Eh). On face value, this might indicate that inclusion of orbitals through restricted active spaces offers no advantage. It might seem that orbitals which

have occupation numbers close to 1.95 and 0.05 in the RASSCF calculation make no significant contributions to static correlation. However, this is not the case. We have already seen that these orbitals have occupation numbers of 1.88/1.87 and 0.12/0.13 in the generalised active spaces. Their inclusion in generalised active spaces allows us to include important quadruple excitations that correlate electrons on the same Mn atom. Therefore, perturbation theory corrections might be overestimated in this CASPT2 calculation. Overestimation is possible because these corrections do not follow the variational principle. Hence, we are not yet able to capture enough of the static "in-out" correlation in the MC-SCF part to make the perturbative treatment of the rest of the correlation accurate. It might be useful to apply perturbation theory corrections to GASSCF calculations which capture sufficient "in-out" correlation, but this has not been implemented yet.

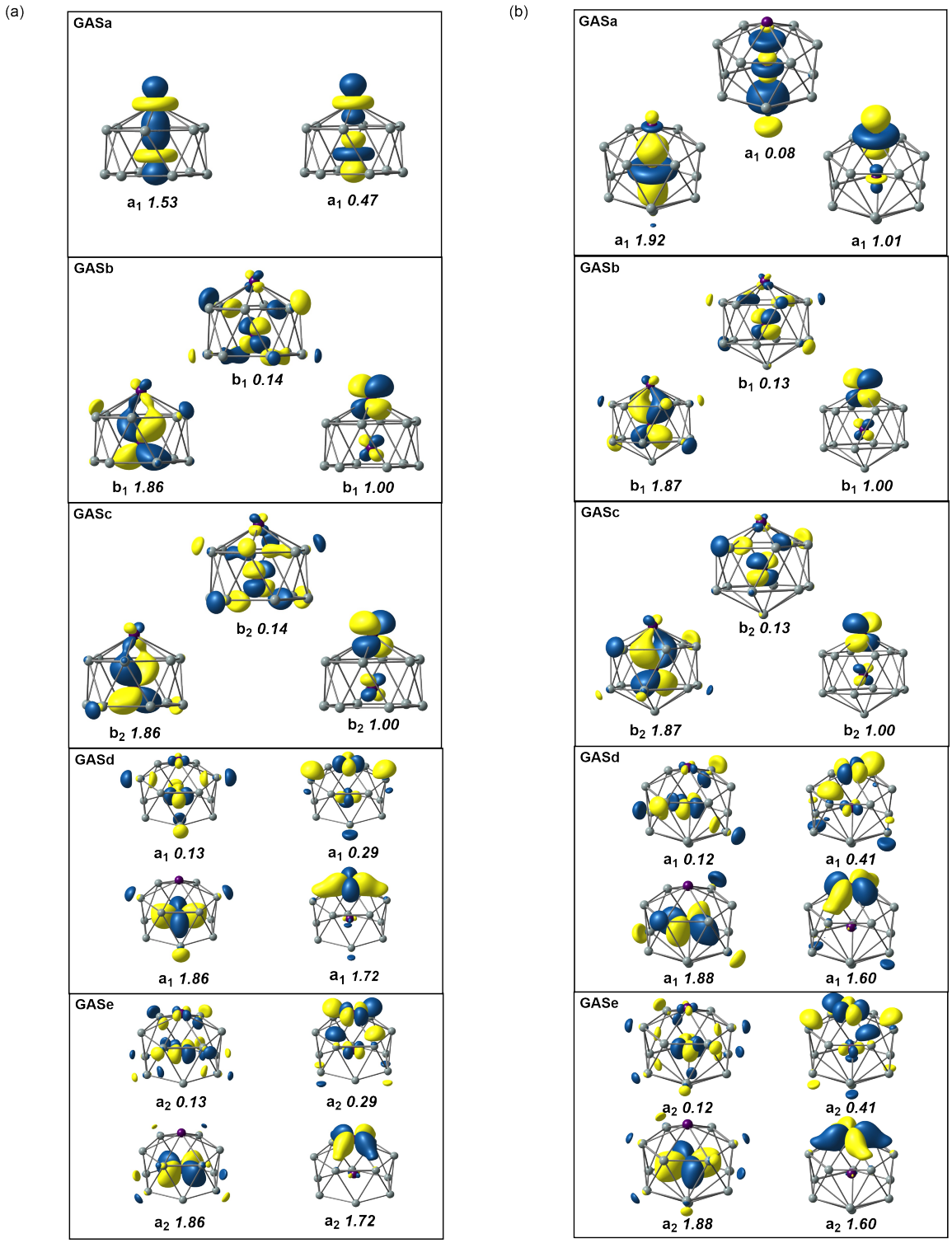


Figure 5.1: Natural orbitals and occupation numbers for (a) GAS5(16,16) active space of ^{3}**12** isomer of Mn_2Si_{12} and (b) GAS5(17,17) active space of ^{4}**13**$^+$**(a)** isomer of $[Mn_2Si_{13}]^+$. (Calculations on Mn_2Si_{12} and $[Mn_2Si_{13}]^+$ used the C_{2v} subgroup rather than the full C_{6v} point symmetry)

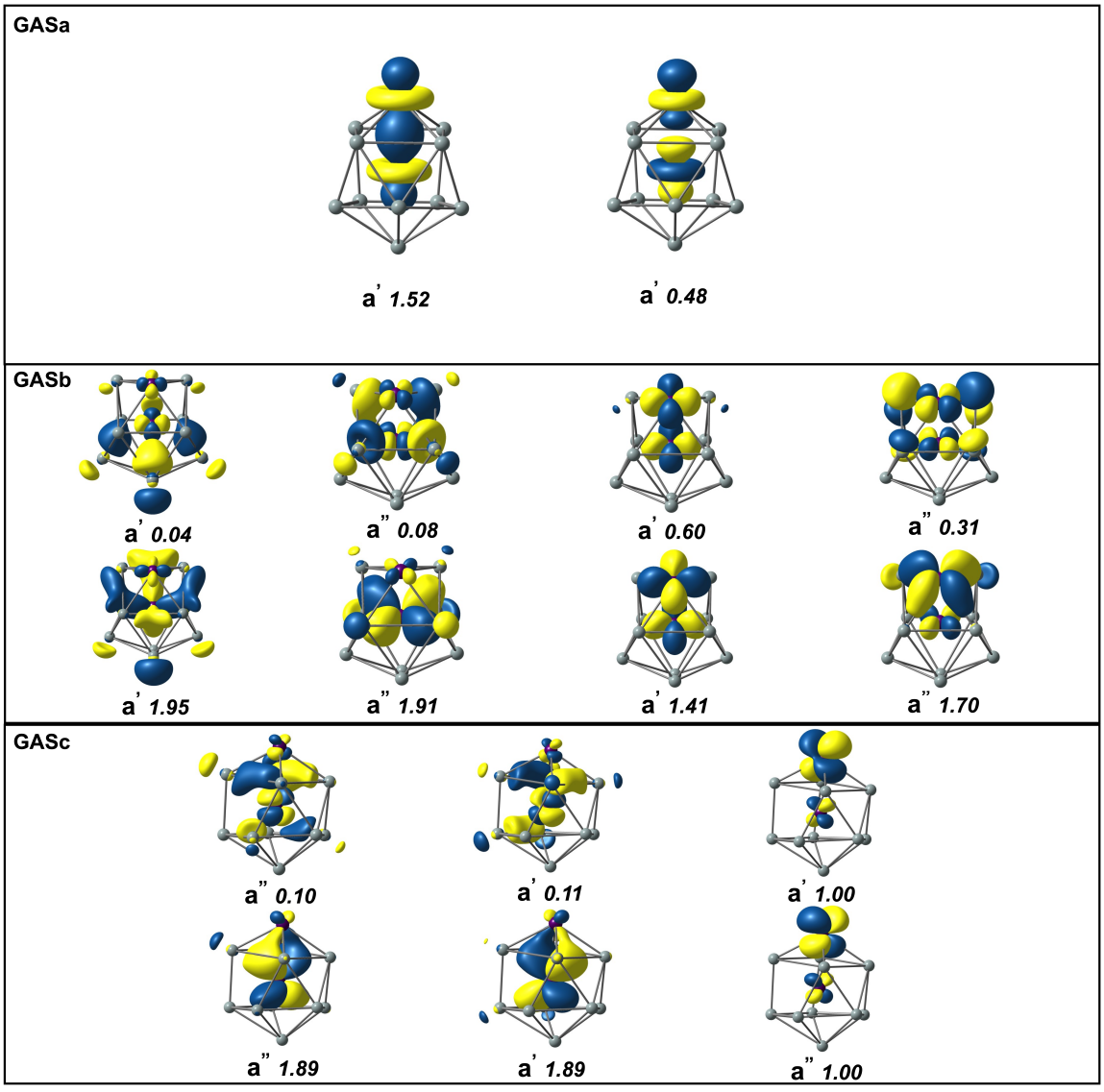


Figure 5.2: Natural orbitals and occupation numbers for the GAS3(16,16) active space of ^{3}**10** isomer of Mn_2Si_{10}. (Calculations on Mn_2Si_{10} used the C_s point group)

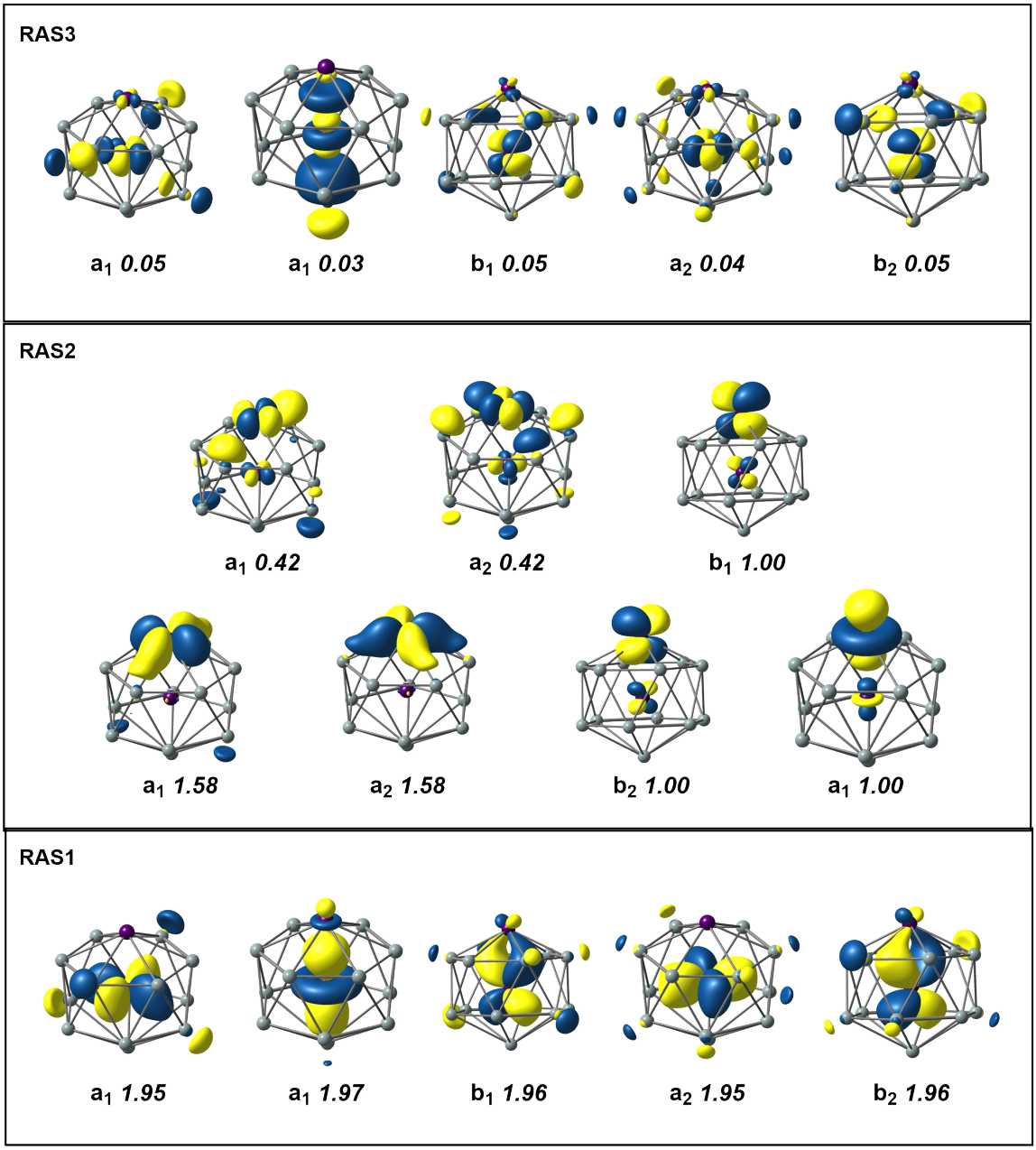


Figure 5.3: Natural orbitals and occupation numbers for the restricted active space of $^4\mathbf{13}^+\mathbf{(a)}$ isomer of $[Mn_2Si_{13}]^+$. (Calculations on $[Mn_2Si_{13}]^+$ used the C_{2v} subgroup rather than the full C_{6v} point symmetry)

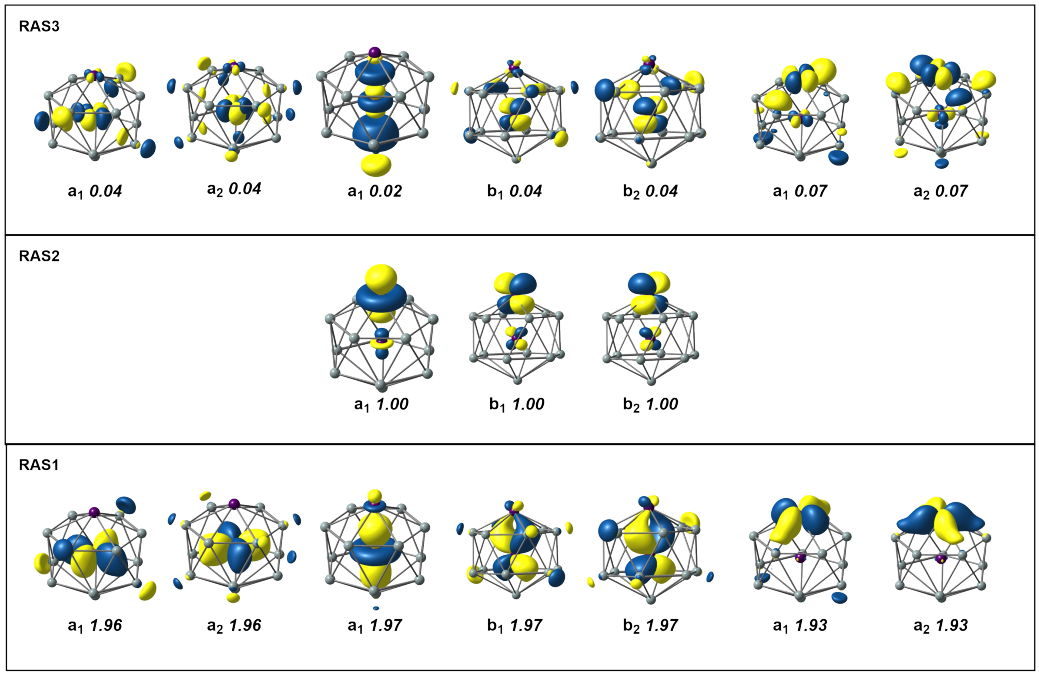


Figure 5.4: Natural orbitals and occupation numbers for the modified restricted active space of $^4\mathbf{13}^+\mathbf{(a)}$ isomer of $[Mn_2Si_{13}]^+$. (Calculations on $[Mn_2Si_{13}]^+$ used the C_{2v} subgroup rather than the full C_{6v} point symmetry)

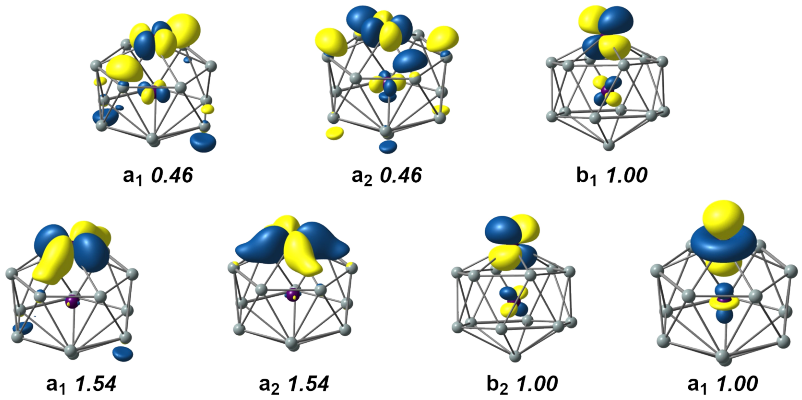


Figure 5.5: Natural orbitals and occupation numbers for the (7,7) active space of $^4\mathbf{13}^+\mathbf{(a)}$ isomer of $[Mn_2Si_{13}]^+$. (Calculations on $[Mn_2Si_{13}]^+$ used the C_{2v} subgroup rather than the full C_{6v} point symmetry)

5.4 Conclusions

In this chapter, GASSCF and RASSCF methods have been used to explore the multi-configurational character of some manganese doped silicon clusters. For Mn_2Si_{12} and Mn_2Si_{10}, "in-out" correlation between the electrons in the Mn-Si bonds and "left-right" correlation between electrons on the two Mn centers has been observed. For $[Mn_2Si_{13}]^+$, while "in-out" correlation has been observed, "left-right" correlation is diminished. By limiting the number of configurations, large active spaces containing orbitals of local σ, π and δ symmetry have been accessed. We have also seen how these Generalized Active Space orbitals map on to the frontier Kohn-Sham orbitals.

In order to account for dynamic correlation, RASPT2 calculations have been carried out for $[Mn_2Si_{13}]^+$. The effect of applying perturbation theory corrections to energies obtained by the RASSCF method has been studied. By comparing the corrected energies of two different restricted active space calculations for $[Mn_2Si_{13}]^+$, we have concluded that perturbation theory cannot account for static correlation that is lost on reducing the size of the active space. We also note in passing that such corrections should be interpreted carefully: the CASPT2 calculation for $[Mn_2Si_{13}]^+$ shows that these corrections can be overestimated.

Chapter 6

Summary

We have investigated the electronic structure and geometries of a series of manganese doped silicon clusters, Mn_2Si_{10}, Mn_2Si_{11}, Mn_2Si_{12} and Mn_2Si_{13}, along with cationic $[Mn_2Si_{13}]^+$, $[Mn_2Si_{14}]^+$ and $[Mn_2Si_{15}]^+$. A combination of infrared multiple photon dissociation (IR-MPD) spectroscopy, density functional theory (DFT) and multiconfigurational self-consistent field (MC-SCF) theory has been used in our studies.

The inspiration behind such an investigation was to understand the impact of the electronic properties of the metal on the cluster and vice versa. Another inspiration was to look for appropriate clusters that could be used as building blocks for magnetic materials, which could find applications in spintronics. Furthermore, these clusters could be viewed as minimal models for transition metal impurities in bulk silicon, which is an issue of importance in the semiconductor industry.

Silicon clusters doped with a single transition metal atom have been extensively studied, but extensions to multiple metals (where the complication of metal-metal as well as metal-silicon bonding emerges) are less common. Experimental characterization of these systems is heavily reliant on spectroscopic techniques, including infrared multiple photon dissociation spectroscopy (IR-MPD), photo-electron spectroscopy (PES) and X-ray absorption studies.

In this thesis, the infrared multiple photon dissociation (IR-MPD) spectroscopy data obtained by Ewald Janssens, André Fielicke and co-workers was used. Calculations with DFT were carried out with the aim of assigning the spectra to different isomers. While initial structures for these clusters were generated primarily using chemical intuition, unbiased algorithms to generate structures were also explored. For some clusters (Mn_2Si_{10}, Mn_2Si_{12} and Mn_2Si_{13}, along with cationic $[Mn_2Si_{13}]^+$), we were able to assign the IR-MPD spectra to single isomers and for others, we could identify a number candidates for the experimentally observed isomers. By assigning vibrational modes to various peaks, the information content of the spectra was expanded. For clusters with high symmetry and common features, the evolution of their vibrational modes could be traced as the cluster size increased.

A strong dependence of conclusions on the choice of exchange-correlation functional used was observed: the relative energies of various isomers, with different spin states, and the their computed infrared spectra changed significantly with the change in functional. The bias of LYP functionals (BLYP and B3LYP) towards structures with low-vertex connectivity and the preference of PBE and PBE0 functionals for deltahedral structures (high-vertex connectivity) was noted. It was realised that relative energies obtained from DFT calculations using a single functional were not the best criteria for selecting the ground-state structure of these clusters. Hence, the wavefunction based multiconfigurational self-consistent field (MC-SCF) theory was employed, which offered a more robust way of dealing with correlation.

For these doubly doped clusters, generalised and restricted active spaces were used instead of the complete active space to restrict the dimension of the CI expansion. "Left-right" correlation between electrons on the two metal centers was observed in addition to the "in-out" correlation between electrons in Mn-Si bonds. In order to account for the dynamic correlation, perturbation theory corrections were applied to the energies obtained by the restricted active space self-consistent field (RASSCF) method. However, sufficient

static correlation could not be captured in the RASSCF wavefunction to allow for a reliable perturbative treatment of the remaining, missing, correlation.

Bibliography

[1] Tsukasa Matsuo and Naoki Hayakawa. π-Electron systems containing Si=Si double bonds. *Sci. Technol. Adv. Mater.*, 19(1):108–129, 2018.

[2] Vijay Kumar and Yoshiyuki Kawazoe. Metal-encapsulated fullerenelike and cubic caged clusters of silicon. *Phys. Rev. Lett.*, 87:045503, 2001.

[3] Vijay Kumar and Yoshiyuki Kawazoe. Metal-encapsulated caged clusters of germanium with large gaps and different growth behavior than silicon. *Phys. Rev. Lett.*, 88:235504, 2002.

[4] Steven M. Beck. Studies of silicon cluster-metal atom compound formation in a supersonic molecular beam. *J. Chem. Phys.*, 87(7):4233–4234, 1987.

[5] Zheng Nie, Ping Guo, Jiming Zheng, Puju Zhao, Yun Wan, and Zhenyi Jiang. Electronic and magnetic properties of two dimensional cluster-assembled materials based on TM@Si_{12} (TM=3d transition metal) clusters. *Comput. Mater. Sci.*, 146:134–142, 2018.

[6] Steven M. Beck. Mixed metal–silicon clusters formed by chemical reaction in a supersonic molecular beam: Implications for reactions at the metal/silicon interface. *J. Chem. Phys.*, 90(11):6306–6312, 1989.

[7] S. N. Khanna, B. K. Rao, and P. Jena. Magic numbers in metallo-inorganic clusters: Chromium encapsulated in silicon cages. *Phys. Rev. Lett.*, 89:016803, 2002.

[8] J. Ulises Reveles and S. N. Khanna. Electronic counting rules for the stability of metal-silicon clusters. *Phys. Rev. B*, 74:035435, 2006.

[9] Marissa Baddick Abreu, Arthur C. Reber, and Shiv N. Khanna. Does the 18-electron rule apply to $CrSi_{12}$? *J. Phys. Chem. Lett.*, 5(20):3492–3496, 2014.

[10] Jiangang He, Kechen Wu, Caiping Liu, and Rongjian Sa. Stabilities of 3d transition-metal doped Si_{14} clusters. *J. Chem. Phys.*, 483(1):30–34, 2009.

[11] Bin Yang, Xi-Ling Xu, Hong-Guang Xu, Umar Farooq, and Wei-Jun Zheng. Structural evolution and electronic properties of $[CoSi_n]^-$ (n = 3-12) clusters: mass-selected anion photoelectron spectroscopy and quantum chemistry calculations. *Phys. Chem. Chem. Phys.*, 21:6207–6215, 2019.

[12] V. Zamudio-Bayer, L. Leppert, K. Hirsch, A. Langenberg, J. Rittmann, M. Kossick, M. Vogel, R. Richter, A. Terasaki, T. Möller, et al. Coordination-driven magnetic-to-nonmagnetic transition in manganese-doped silicon clusters. *Phys. Rev. B*, 88:115425, 2013.

[13] Vu Thi Ngan, Philipp Gruene, Pieterjan Claes, Ewald Janssens, André Fielicke, Minh Tho Nguyen, and Peter Lievens. Disparate effects of Cu and V on structures of exohedral transition metal-doped silicon clusters: A combined far-infrared spectroscopic and computational study. *J. Am. Chem. Soc.*, 132(44):15589–15602, 2010.

[14] Dinesh Bista, Arthur C. Reber, Vikas Chauhan, and Shiv N. Khanna. Electronic and magnetic properties of $Fe_2Si_n^{+/0/-}$ ($1 \leq n \leq 12$) clusters. *Chem. Phys. Lett.*, 706:113–119, 2018.

[15] Vaida Arcisauskaite, Domagoj Fijan, Mariano Spivak, Coen de Graaf, and John E. McGrady. Biradical character in the ground state of $[Mn@Si_{12}]^+$: a DFT and CASPT2 study. *Phys. Chem. Chem. Phys.*, 18:24006–24014, 2016.

[16] P. Hohenberg and W. Kohn. Inhomogeneous electron gas. *Phys. Rev.*, 136:B864–B871, 1964.

[17] A. D. Becke. Density-functional exchange-energy approximation with correct asymptotic behavior. *Phys. Rev. A*, 38:3098–3100, 1988.

[18] Chengteh Lee, Weitao Yang, and Robert G. Parr. Development of the colle-salvetti correlation-energy formula into a functional of the electron density. *Phys. Rev. B*, 37:785–789, 1988.

[19] John P. Perdew, Kieron Burke, and Matthias Ernzerhof. Generalized gradient approximation made simple. *Phys. Rev. Lett.*, 77:3865–3868, 1996.

[20] Axel D. Becke. Density-functional thermochemistry. III. The role of exact exchange. *J. Chem. Phys.*, 98(7):5648–5652, 1993.

[21] John P. Perdew, Matthias Ernzerhof, and Kieron Burke. Rationale for mixing exact exchange with density functional approximations. *J. Chem. Phys.*, 105(22):9982–9985, 1996.

[22] Florian Weigend and Reinhart Ahlrichs. Balanced basis sets of split valence, triple zeta valence and quadruple zeta valence quality for H to Rn: Design and assessment of accuracy. *Phys. Chem. Chem. Phys.*, 7:3297–3305, 2005.

[23] Liangyou Fan and Tom Ziegler. Application of density functional theory to infrared absorption intensity calculations on main group molecules. *J. Chem. Phys.*, 96(12):9005–9012, 1992.

[24] Liangyou Fan and Tom Ziegler. Application of density functional theory to infrared absorption intensity calculations on transition-metal carbonyls. *J. Phys. Chem.*, 96(17):6937–6941, 1992.

[25] G. te Velde, F. M. Bickelhaupt, E. J. Baerends, C. Fonseca Guerra, S. J. A. van Gisbergen, J. G. Snijders, and T. Ziegler. Chemistry with ADF. *J. Comput. Chem.*, 22(9):931–967, 2001.

[26] Xiao Jin and John E. McGrady. Structure and bonding in endohedral transition metal clusters. *Adv. Inorg. Chem.*, 73:265–304, 2019.

[27] José M. Goicoechea and John E. McGrady. On the structural landscape in endohedral silicon and germanium clusters, M@Si_{12} and M@Ge_{12}. *Dalton Trans.*, 44:6755–6766, 2015.

[28] Jijun Zhao, Qiuying Du, Si Zhou, and Vijay Kumar. Endohedrally doped cage clusters. *Chem. Rev.*, 120(17):9021–9163, 2020.

[29] Anton Römer, Lukas Hasecke, Peter Blöchl, and Ricardo A. Mata. A review of density functional models for the description of Fe(II) spin-crossover complexes. *Molecules*, 25(21):5176, 2020.

[30] Xiao Jin, Vaida Arcisauskaite, and John E. McGrady. The structural landscape in 14-vertex clusters of silicon, M@Si_{14}: when two bonding paradigms collide. *Dalton Trans.*, 46:11636–11644, 2017.

[31] Debashis Bandyopadhyay and Prasenjit Sen. Density functional investigation of structure and stability of Ge_n and Ge_nNi (n = 1-20) clusters: validity of the electron counting rule. *J. Phys. Chem. A*, 114(4):1835–1842, 2010.

[32] Kapil Dhaka and Debashis Bandyopadhyay. Study of the electronic structure, stability and magnetic quenching of $CrGe_n$ (n = 1-17) clusters: a density functional investigation. *RSC Adv.*, 5:83004–83012, 2015.

[33] Vikas Chauhan, Marissa Baddick Abreu, Arthur C. Reber, and Shiv N. Khanna. Geometry controls the stability of $FeSi_{14}$. *Phys. Chem. Chem. Phys.*, 17:15718–15724, 2015.

[34] M. M. Uță, D. Cioloboc, and R. B. King. Cobalt-centered ten-vertex germanium clusters: the pentagonal prism as an alternative to polyhedra predicted by the wade-mingos rules. *Inorg. Chem.*, 51(6):3498–3504, 2012.

[35] Emmanuel N. Koukaras, Christos S. Garoufalis, and Aristides D. Zdetsis. Structure and properties of the $Ni@Si_{12}$ cluster from all-electron ab initio calculations. *Phys. Rev. B*, 73:235417, 2006.

[36] Vijay Kumar and Yoshiyuki Kawazoe. Magic behavior of $Si_{15}M$ and $Si_{16}M$ (M = Cr, Mo, and W) clusters. *Phys. Rev. B*, 65:073404, 2002.

[37] Vu Thi Ngan, Kristine Pierloot, and Minh Tho Nguyen. $Mn@Si_{14}^{+}$: a singlet fullerene-like endohedrally doped silicon cluster. *Phys. Chem. Chem. Phys.*, 15:5493–5498, 2013.

[38] Minh Thao Nguyen, Quoc Tri Tran, and Van Tan Tran. The ground and excited low-lying states of $VSi_2^{0/-/+}$ clusters from CASSCF/CASPT2 calculations. *Chem. Phys, Lett.*, 721:111–116, 2019.

[39] Van Tan Tran, Xuan Mai Thi Tran, Minh Thao Nguyen, Huu Tho Nguyen, and Quoc Tri Tran. A new interpretation of the photoelectron spectrum of VSi_4^{-} cluster by density functional theory and multiconfigurational CASSCF/CASPT2 calculations. *Chem. Phys. Lett.*, 690:140–146, 2017.

[40] Van Tan Tran and Quoc Tri Tran. Low-lying electronic states of $FeGe_n^{-/0}$ (n = 1-3) clusters calculated with multireference second-order perturbation theory. *J. Phys. Chem. A*, 124(20):4095–4105, 2020.

[41] Van Tan Tran and Quoc Tri Tran. The electronic structures of $CoGe_n^{-/0}$ (n = 1-3) clusters from multiconfigurational CASSCF/CASPT2 and RASSCF/RASPT2 calculations. *J. Phys. Chem. A*, 122(31):6407–6415, 2018.

[42] Van Tan Tran, Minh Thao Nguyen, and Quoc Tri Tran. Computational investigation of the geometrical and electronic structures of $VGe_n^{-/0}$ (n = 1-4) clusters by density functional theory and multiconfigurational CASSCF/CASPT2 method. *J. Phys. Chem. A*, 121(40):7787–7796, 2017.

[43] Van Tan Tran and Quoc Tri Tran. A density matrix renormalization group investigation on the electronic states of $MnGe_n^{-/0/+}$ (n = 1-3) clusters. *Int. J. Quantum Chem.*, 121(10):e26619, 2021.

[44] Van Tan Tran. Electronic states of $[CoSi_n]^{-/0/+}$ (n = 1-3) clusters from density matrix renormalization group CASPT2 calculations. *J. Phys. Chem. A*, 125(26):5800–5810, 2021.

[45] Sheng-Jie Lu, Xi-Ling Xu, Hong-Guang Xu, and Wei-Jun Zheng. Structural evolution and bonding properties of $[Au_2Si_n]^{-/0}$ (n = 1-7) clusters: Anion photoelectron spectroscopy and theoretical calculations. *J. Chem. Phys.*, 148(24):244306, 2018.

[46] Xiaoming Huang, Sheng-Jie Lu, Xiaoqing Liang, Yan Su, Linwei Sai, Zeng-Guang Zhang, Jijun Zhao, Hong-Guang Xu, and Weijun Zheng. Structures and electronic properties of $[V_3Si_n]^-$ (n = 3-14) clusters: A combined *ab initio* and experimental study. *J. Phys. Chem. C*, 119(20):10987–10994, 2015.

[47] Sheng-Jie Lu, Hong-Guang Xu, Xi-Ling Xu, and Wei-Jun Zheng. Anion photoelectron spectroscopy and theoretical investigation on $[Nb_2Si_n]^{-/0}$ (n = 2-12) clusters. *J. Phys. Chem. C*, 121(21):11851–11861, 2017.

[48] Bin Yang, Hongguang Xu, Xiling Xu, and Weijun Zheng. Photoelectron spectroscopy and theoretical study of Cr_nSi_{15-n} (n = 1-3): Effects of doping Cr atoms on the structural and magnetic properties. *J. Phys. Chem. A*, 122(51):9886–9893, 2018.

[49] Hong-Guang Xu, Miao Miao Wu, Zeng-Guang Zhang, Jinyun Yuan, Qiang Sun, and Weijun Zheng. Photoelectron spectroscopy and density functional calculations of $[CuSi_n]^-$ (n = 4-18) clusters. *J. Chem. Phys.*, 136(10):104308, 2012.

[50] Li-Juan Zhang, Bin Yang, Da-Zhi Li, Umar Farooq, Xi-Ling Xu, Wei-Jun Zheng, and Hong-Guang Xu. Appearance of V-encapsulated tetragonal prism motifs in $[VSi_{10}]^-$ and $[VSi_{11}]^-$ clusters. *Phys. Chem. Chem. Phys.*, 22:22989–22996, 2020.

[51] Xiaoqing Liang, Xiangyu Kong, Sheng-Jie Lu, Yingying Huang, Jijun Zhao, Hong-Guang Xu, Weijun Zheng, and Xiao Cheng Zeng. Structural evolution and magnetic properties of anionic clusters Cr_2Ge_n (n = 3–14): photoelectron spectroscopy and density functional theory computation. *J. Phys. Cond. Matter*, 30(33):335501, 2018.

[52] Xiao-Qing Liang, Xiao-Jiao Deng, Sheng-Jie Lu, Xiao-Ming Huang, Ji-Jun Zhao, Hong-Guang Xu, Wei-Jun Zheng, and Xiao Cheng Zeng. Probing structural, electronic, and magnetic properties of iron-doped semiconductor clusters $Fe_2Ge_n^{-/0}$ (n = 3-12) via joint photoelectron spectroscopy and density functional study. *J. Phys. Chem. C*, 121(12):7037–7046, 2017.

[53] Vaibhav Khanna, Roshan Singh, Pieterjan Claes, Minh Tho Nguyen, André Fielicke, Ewald Janssens, Peter Lievens, and John E. McGrady. Evolution of vibrational spectra in the manganese–silicon clusters Mn_2Si_n, n = 10, 12, and 13, and cationic $[Mn_2Si_{13}]^+$. *J. Phys. Chem. A*, 126(10):1617–1626, 2022.

[54] Hung Tan Pham, Thu-Thuy Phan, Nguyen Minh Tam, Long Van Duong, My Phuong Pham-Ho, and Minh Tho Nguyen. $Mn_2@Si_{15}$: the smallest triple ring tubular silicon cluster. *Phys. Chem. Chem. Phys.*, 17:17566–17570, 2015.

[55] Hung Tan Pham, Cam-Tu Phan-Dang, Nguyen Tien Trung, and Vu Thi Ngan. Transformation between hexagonal prism and antiprism of the singly and doubly Cr-doped Ge_{12} clusters. *J. Phys. Chem. A*, 123(50):10721–10729, 2019.

[56] Kapil Dhaka and Debashis Bandyopadhyay. Magnetism, structures and stabilities of cluster assembled TM@Si nanotubes (TM = Cr, Mn and Fe): a density functional study. *Dalton Trans.*, 45:12432–12443, 2016.

[57] F. Hagelberg, C. Xiao, and William A. Lester. Cagelike Si_{12} clusters with endohedral Cu, Mo, and W metal atom impurities. *Phys. Rev. B*, 67:035426, 2003.

[58] Ju-Guang Han, Run-Ning Zhao, and Yuhua Duan. Geometries, stabilities, and growth patterns of the bimetal Mo_2-doped Si_n (n = 9 - 16) clusters: A density functional investigation. *J. Phys. Chem., A*, 111(11):2148–2155, 2007.

[59] Vijay Kumar and Yoshiyuki Kawazoe. Hydrogenated silicon fullerenes: Effects of H on the stability of metal-encapsulated silicon clusters. *Phys. Rev. Lett.*, 90:055502, 2003.

[60] Xiaoming Huang, Hong-Guang Xu, Shengjie Lu, Yan Su, R. B. King, Jijun Zhao, and Weijun Zheng. Discovery of a silicon-based ferrimagnetic wheel structure in $V_xSi_{12}^-$ (x = 1-3) clusters: photoelectron spectroscopy and density functional theory investigation. *Nanoscale*, 6:14617–14621, 2014.

[61] Shuai Zhang, Yu Zhang, Xingqiang Yang, Cheng Lu, Genquan Li, and Zhiwen Lu. Systematic theoretical investigation of structures, stabilities, and electronic properties of rhodium-doped silicon clusters: $Rh_2Si_n^q$ (n = 1-10; q = 0, $\pm$1). *J. Mat. Sci.*, 50(18):6180–6196, 2015.

[62] Zhifeng Liu, Xinqiang Wang, Jiangtao Cai, and Hengjiang Zhu. Room-temperature ordered spin structures in cluster-assembled single $V@Si_{12}$ sheets. *J. Phys. Chem C*, 119(3):1517–1523, 2015.

[63] Dennis Palagin, Tobias Teufl, and Karsten Reuter. Multidoping of Si cages: high spin states beyond the single-dopant septet limit. *J. Phys. Chem. C*, 117(31):16182–16186, 2013.

[64] Nguyen Duy Phi, Nguyen Tien Trung, Ewald Janssens, and Vu Thi Ngan. Electron counting rules for transition metal-doped Si_{12} clusters. *Chem. Phys. Lett.*, 643:103–108, 2016.

[65] A. Fielicke, G. von Helden, and G. Meijer. Far-infrared of isolated transition metal clusters. *Eur. Phys. J. D*, 34(1):83–88, 2005.

[66] D. Oepts, A.F.G. van der Meer, and P.W. van Amersfoort. The free-electron-laser user facility felix. *Infrared Phys. Technol.*, 36(1):297–308, 1995. Proceedings of the Sixth International Conference on Infrared Physics.

[67] Piero Ferrari, Jan Vanbuel, Yejun Li, Ting-Wei Liao, Ewald Janssens, and Peter Lievens. *The Double-Laser Ablation Source Approach*, chapter 4, pages 59–78. John Wiley & Sons, Ltd, Weinheim, 2017.

[68] E. Van Lenthe and E. J. Baerends. Optimized slater-type basis sets for the elements 1-118. *J. Comp. Chem.*, 24(9):1142–1156, 2003.

[69] Yejun Li, Nguyen Minh Tam, Alex P. Woodham, Jonathan T. Lyon, Zhe Li, Peter Lievens, André Fielicke, Minh Tho Nguyen, and Ewald Janssens. Structure dependent magnetic coupling in cobalt-doped silicon clusters. *J. Phys. Chem. C*, 120(34):19454–19460, 2016.

[70] Hung Tan Pham, Devashis Majumdar, Jerzy Leszczynski, and Minh Tho Nguyen. 4d and 5d bimetal doped tubular silicon clusters $Si_{12}M_2$ with M = Nb, Ta, Mo and W: a bimetallic configuration model. *Phys. Chem. Chem. Phys.*, 19:3115–3124, 2017.

[71] Vu Thi Ngan, Ewald Janssens, Pieterjan Claes, Jonathan T. Lyon, André Fielicke, Minh Tho Nguyen, and Peter Lievens. High magnetic moments in manganese-doped silicon clusters. *Chem. Eur. J.*, 18(49):15788–15793, 2012.

[72] Pieterjan Claes, Vu Thi Ngan, Marko Haertelt, Jonathan T. Lyon, André Fielicke, Minh Tho Nguyen, Peter Lievens, and Ewald Janssens. The structures of neutral transition metal doped silicon clusters, Si_nX (n = 6 - 9; X = V, Mn). *J. Chem. Phys.*, 138(19):194301, 2013.

[73] Michel Martin, Bernard Rees, and A Mitschler. Bonding in a binuclear metal carbonyl: experimental charge density in $Mn_2(CO)_{10}$. *Acta Cryst. B*, 38(1):6–15, 1982.

[74] Vu Thi Ngan, Ewald Janssens, Pieterjan Claes, André Fielicke, Minh Tho Nguyen, and Peter Lievens. Nature of the interaction between rare gas atoms and transition metal doped silicon clusters: the role of shielding effects. *Phys. Chem. Chem. Phys.*, 17:17584–17591, 2015.

[75] Takehide Miyazaki, Hidefumi Hiura, and Toshihiko Kanayama. Topology and energetics of metal-encapsulating Si fullerenelike cage clusters. *Phys. Rev. B*, 66:121403, 2002.

[76] Jian Lv, Yanchao Wang, Li Zhu, and Yanming Ma. Particle-swarm structure prediction on clusters. *J. Chem. Phys.*, 137(8):084104, 2012.

[77] Partha P. Bera, Kurt W. Sattelmeyer, Martin Saunders, Henry F. Schaefer, and Paul v. R. Schleyer. Mindless chemistry. *J. Phys. Chem. A*, 110(13):4287–4290, 2006.

[78] Jun Zhang and Michael Dolg. ABCluster: the artificial bee colony algorithm for cluster global optimization. *Phys. Chem. Chem. Phys.*, 17:24173–24181, 2015.

[79] Jun Zhang and Michael Dolg. Global optimization of clusters of rigid molecules using the artificial bee colony algorithm. *Phys. Chem. Chem. Phys.*, 18:3003–3010, 2016.

[80] Ignacio Fdez. Galván, Morgane Vacher, Ali Alavi, Celestino Angeli, Francesco Aquilante, Jochen Autschbach, Jie J. Bao, Sergey I. Bokarev, Nikolay A. Bogdanov, Rebecca K. Carlson, Liviu F. Chibotaru, Joel Creutzberg, Nike Dattani, Mickaël G. Delcey, Sijia S. Dong, Andreas Dreuw, Leon Freitag, Luis Manuel Frutos, Laura Gagliardi, Frédéric Gendron, Angelo Giussani, Leticia González, Gilbert Grell, Meiyuan Guo, Chad E. Hoyer, Marcus Johansson, Sebastian Keller, Stefan Knecht, Goran Kovačević, Erik Källman, Giovanni Li Manni, Marcus Lundberg, Yingjin Ma, Sebastian Mai, João Pedro Malhado, Per Åke Malmqvist, Philipp Marquetand, Stefanie A. Mewes, Jesper Norell, Massimo Olivucci, Markus Oppel, Quan Manh Phung, Kristine Pierloot, Felix Plasser, Markus Reiher, Andrew M. Sand, Igor Schapiro, Prachi Sharma, Christopher J. Stein, Lasse Kragh Sørensen, Donald G. Truhlar, Mihkel Ugandi, Liviu Ungur, Alessio Valentini, Steven Vancoillie, Valera Veryazov, Oskar Weser, Tomasz A. Wesołowski, Per-Olof Widmark, Sebastian Wouters, Alexander Zech, J. Patrick Zobel, and Roland Lindh. OpenMolcas: from source code to insight. *J. Chem. Theory Comput.*, 15(11):5925–5964, 2019.

[81] Francesco Aquilante, Jochen Autschbach, Alberto Baiardi, Stefano Battaglia, Veniamin A. Borin, Liviu F. Chibotaru, Irene Conti, Luca De Vico, Mickaël Delcey, Ignacio Fdez. Galván, Nicolas Ferré, Leon Freitag, Marco Garavelli, Xuejun Gong, Stefan Knecht, Ernst D. Larsson, Roland Lindh, Marcus Lundberg, Per Åke Malmqvist, Artur Nenov, Jesper Norell, Michael Odelius, Massimo Olivucci, Thomas B. Pedersen, Laura Pedraza-González, Quan M. Phung, Kristine Pierloot, Markus Reiher, Igor Schapiro, Javier Segarra-Martí, Francesco Segatta, Luis Seijo, Saumik Sen, Dumitru-Claudiu Sergentu, Christopher J. Stein, Liviu Ungur, Morgane Vacher, Alessio Valentini, and Valera Veryazov. Modern quantum chemistry with [open]Molcas. *J. Chem. Phys.*, 152(21):214117, 2020.

[82] K Pierloot, B Dumez, PO Widmark, and BO Roos. Density matrix averaged atomic

natural orbital (ANO) basis sets for correlated molecular wave functions. *Theor. Chim. Acta*, 90(2-3):87–114, 1995.

[83] Soumen Ghosh, Christopher J. Cramer, Donald G. Truhlar, and Laura Gagliardi. Generalized-active-space pair-density functional theory: an efficient method to study large, strongly correlated, conjugated systems. *Chem. Sci.*, 8:2741–2750, 2017.

[84] Konstantinos D. Vogiatzis, Giovanni Li Manni, Samuel J. Stoneburner, Dongxia Ma, and Laura Gagliardi. Systematic expansion of active spaces beyond the CASSCF limit: a GASSCF/SplitGAS benchmark study. *J. Chem. Theory Comput.*, 11(7):3010–3021, 2015.

[85] Dongxia Ma, Giovanni Li Manni, and Laura Gagliardi. The generalized active space concept in multiconfigurational self-consistent field methods. *J. Chem. Phys.*, 135(4):044128, 2011.